NASA Technical Paper 2560

September 1986

Application of LQG/LTR Technique to Robust Controller Synthesis for a Large Flexible Space Antenna

Suresh M. Joshi,
Ernest S. Armstrong, and
N. Sundararajan

NASA

NASA Technical Paper 2560

1986

Application of LQG/LTR Technique to Robust Controller Synthesis for a Large Flexible Space Antenna

Suresh M. Joshi and
Ernest S. Armstrong
Langley Research Center
Hampton, Virginia

N. Sundararajan
Old Dominion University Research Foundation
Norfolk, Virginia

National Aeronautics
and Space Administration

**Scientific and Technical
Information Branch**

Summary

This paper investigates the application of the linear-quadratic-Gaussian (LQG)/loop transfer recovery (LTR) method to the problem of synthesizing an attitude control system for a large flexible space antenna. The study is based on a finite-element model of the 122-m hoop/column antenna, which consists of three rigid-body rotational modes and the first 10 elastic modes. A robust compensator design for achieving the required performance bandwidth in the presence of modeling uncertainties is obtained by using the LQG/LTR method for loop shaping in the frequency domain. Based on the limitations of achieved performance with the LQG/LTR method, different sensor actuator locations are analyzed in terms of the pole zero locations of the multivariable systems and possible best locations are indicated. The computations are performed by using the LQG design package ORACLS augmented with frequency domain singular value analysis software.

1. Introduction

The robust control synthesis methodology which uses frequency domain matrix norm bounds (i.e., singular values) has received considerable attention in the recent literature (refs. 1 through 5).[1] The basic framework for frequency domain synthesis using the linear-quadratic-Gaussian (LQG)/loop-transfer-recovery (LTR) methodology was developed in references 1 and 2. It has been applied to diverse systems such as power systems (ref. 3) and aircraft engine control (ref. 4). The LQG/LTR design philosophy uses a low frequency "design model" of the plant and a high frequency characterization of the modeling errors. This method, which uses unstructured uncertainty and singular value bounds, appears to be particularly well suited for the control of large flexible spacecraft because of the considerable uncertainty that inherently exists in the mathematical models.

Large space structures (LSS) are typically highly flexible and can be represented by partial differential equations or by very large systems of ordinary differential equations. They have many resonant frequencies, some of which may be very low and possibly closely spaced. The natural damping is usually very small. For these reasons, control of LSS is a challenging task (ref. 5).

Since the system is inherently of high order, a practical controller has to be based on a reduced-order design model. Furthermore, the parameters (i.e., frequencies, mode shapes, and damping ratios) of the system are known imprecisely; this introduces additional modeling errors. Typically, the modeling errors for finite-element models increase substantially with increasing modal frequency. Controller design for large space structures using frequency domain analysis was investigated in reference 6, wherein singular value analysis was used to check the robustness with respect to modeling errors.

One of the planned activities of the NASA Space Transportation System is the placement in Earth orbit of a variety of large space antennas. Potential large space missions will require antennas and structures ranging from 30 m to 20 km in size. Applications include communications (mobile, trunking, etc.), remote sensing (soil moisture, salinity, etc.), deep space network (orbital relays), astronomy (X-ray, observatory, optical array, radio telescope, very long baseline interferometry, etc.), energy, and space platforms. Specific missions have been pinpointed and future requirements identified for large space antennas for communications, Earth sensing, and radio astronomy (ref. 7). Particular emphasis is placed on mesh-deployable antennas in the 50- to 120-m-diameter category. One such antenna is the maypole (hoop/column) antenna, shown schematically in figure 1. The hoop/column antenna basically consists of a central mast attached to a deployable hoop by cables in tension (refs. 7 and 8). The deployable mast consists of a number of telescoping sections, and the hoop consists of 48 rigid segments. The reflective mesh, which is made of knit gold-plated molybdenum wire, is attached to the hoop by graphite fibers. The mesh is shaped by using a network of stringers and ties to form the radio-frequency (RF) reflective surface. In order to achieve

[1] This methodology was also presented in a lecture entitled "Multivariable Control System Design Using the LQG/LTR Methodology" given by Professor Michael Athans of the Massachusetts Institute of Technology at the Langley Research Center in 1984.

required RF performance, the antenna must be controlled to specified precision in attitude and shape. For example, for missions such as land mobile satellite system (LMSS) for providing mobile telephone service to users in the continental United States, it is necessary to achieve a pointing accuracy of 0.03° rms (root mean square) and a surface accuracy of 6 mm rms. It is also necessary to have stringent control (usually a fraction of a degree) on the motion of the feed (located near one end of the mast) relative to the mesh. Because of its large size and relatively light weight, the antenna is highly flexible, having a large number of significant elastic modes. It is therefore necessary to use reduced-order controllers.

Reduced-order control synthesis for this system using the standard LQG theory was investigated in reference 9. The standard LQG procedure yielded satisfactory control, that is, rigid-body bandwidth of up to 0.25 rad/sec, satisfactory time constants for the elastic modes, and acceptable rms pointing errors in the presence of sensor noise. It should be noted that the LQG approach in reference 10 used a large number of actuators and sensors (four three-axis torque actuators and four three-axis attitude and rate sensors). It was found that the first three flexible modes had to be included in the design model (in addition to the three rigid modes) to obtain satisfactory performance. The main problem with the LQG method was that a large number of weighting parameters had to be simultaneously adjusted to obtain a good design. In addition, the stability robustness properties with respect to inaccuracies in the modal parameters could not be properly assessed because it was difficult to effectively characterize the bounds on modeling errors in a time-domain setting. The LQG/LTR method offers an approach for overcoming these problems in the frequency domain.

The purpose of this paper is to investigate the use of LQG/LTR multivariable frequency domain methodology in the design of an attitude control system for the hoop/column antenna. The design approach considered herein is deterministic, and the rms pointing errors in the presence of noise are not analyzed. A sequence of low order compensators is obtained by considering design models which include increasingly higher frequency modes. The final design model chosen is the first one in this sequence which allows the performance/robustness objectives to be met. In this sequence of design models, the first one consists of the rigid-body modes only. Subsequent design models are obtained by the successive addition of flexible modes. The designs use three-axis torque actuators, collocated attitude and rate sensors, and attitude and rate feedback. The organization of this paper is as follows. The mathematical model of the system is first described in section 3. Section 4 describes the control objectives, followed by a brief description of the LQG/LTR technique (refs. 1 and 2) in section 5. The reduced-order (low frequency) design model and the high frequency modeling uncertainty barrier are also discussed in that section. The numerical results are given in section 6. Section 6.1 presents the results of synthesizing the controller based on the LQG/LTR procedure with only attitude feedback being used. Section 6.2 describes the results obtained when both attitude and rate feedback are used for controller design. Some of the problems and limitations observed are also highlighted. Specifically the locations of transmission zeros and their impact on the performance for two different sensor and actuator locations are discussed. The results are summarized in section 7.

2. Symbols

$\mathbf{A}$	system matrix
$\mathbf{A}_F$	system matrix for full-order plant
$\mathbf{B}$	input matrix
$\mathbf{B}_F$	input matrix for full-order plant
$\mathbf{C}$	output matrix
$\mathbf{C}_F$	output matrix for full-order plant
$\mathbf{D}$	damping matrix
$\mathbf{G}$	regulator gain matrix
$\mathbf{G}_c$	compensator transfer function
$\hat{\mathbf{G}}_c$	modified compensator function
$\mathbf{G}_F$	complete plant transfer function
$\mathbf{G}_{KF}$	Kalman filter transfer function for attitude feedback
$\hat{\mathbf{G}}_{KF}$	Kalman filter transfer function for attitude and rate feedback
$\mathbf{G}_L$	modified loop gain
$\mathbf{G}_p$	plant transfer function
$\hat{\mathbf{G}}_p$	modified plant transfer function
$\mathbf{G}_1$	rigid-body transfer function
$\mathbf{G}_2$	elastic-mode transfer function
$\mathbf{H}$	Kalman gain
$\mathbf{I}$	identity matrix
$\mathbf{I}_k$	$k \times k$ identity matrix
$\mathbf{I}_s$	inertia matrix
$\mathbf{L}$	weighting matrix used in Kalman filter design

$\mathbf{L}_p$	multiplicative uncertainty
l_m	upper bound on multiplicative uncertainty
m	order of input vector
n	order of system
n_q	number of elastic modes
n_T	number of torque actuators
$\mathbf{P}$	regulator Riccati matrix
$\mathbf{q}$	modal amplitude vector
q	regulator design parameter
r	reference input
s	Laplace variable
$\mathbf{T}_j$	torque vector for jth actuator
$\mathbf{u}$	input vector
$\mathbf{x}$	state vector
$\hat{\mathbf{x}}$	state estimate vector
$\mathbf{y}_a$	sensed attitude
$\mathbf{y}_r$	sensed rate
$\boldsymbol{\alpha}_s$	rigid-body attitude vector
$\Delta\mathbf{G}$	additive uncertainty
ζ_i	damping ratio for ith elastic mode
θ_s	rigid-body rotation about Y-axis
$\boldsymbol{\Lambda}$	diagonal matrix of squares of natural frequencies
μ	Kalman filter design parameter
$\boldsymbol{\Sigma}$	Kalman filter Riccati matrix
σ	singular value
$\overline{\sigma}$	largest singular value
$\underline{\sigma}$	smallest singular value
$\boldsymbol{\Phi}$	mode slope matrix at actuator locations
ϕ_s	rigid-body rotation about X-axis
$\boldsymbol{\Psi}$	mode slope matrix at sensor locations
ψ_s	rigid-body rotation about Z-axis
ω	frequency
ω_i	natural frequency of ith elastic mode

Dots over symbol indicate derivative with respect to time; superscript T indicates a transposed matrix.

3. Mathematical Model

As a consequence of its large size and light weight, the antenna is a highly flexible system having a large number of significant structural modes. A finite-element model of the antenna (ref. 8) is used in this paper. The mathematical model considered consists of rotational rigid-body dynamics (about the three axes) and the elastic motion. We assume that the control will be accomplished by using n_T three-axis torque actuators. The linearized equations of motion are

$$\mathbf{I}_s\ddot{\boldsymbol{\alpha}}_s = \sum_{j=1}^{n_T} \mathbf{T}_j \tag{1}$$

$$\ddot{\mathbf{q}} + \mathbf{D}\dot{\mathbf{q}} + \boldsymbol{\Lambda}\mathbf{q} = \boldsymbol{\Phi}^T\mathbf{u} \tag{2}$$

where $\mathbf{I}_s$ is the 3×3 inertia matrix, $\mathbf{T}_j$ is the three-axis torque applied by the jth actuator, $\boldsymbol{\alpha}_s = (\phi_s, \theta_s, \psi_s)^T$ denotes the rigid-body attitude, $\mathbf{q}$ is the $n_q \times 1$ modal amplitude vector (for n_q structural modes), $\mathbf{D} = 2$ diag $(\zeta_1\omega_1, \zeta_2\omega_2, \ldots, \zeta_{nq}\omega_{nq})$ is the inherent damping matrix (where ζ_i is the damping ratio for the ith mode), $\boldsymbol{\Phi}$ is the $m \times n_q$ "mode-slope" matrix (where $m = 3n_T$), $\mathbf{u} = (\mathbf{T}_1^T, \mathbf{T}_2^T, \ldots, \mathbf{T}_{nT}^T)^T$ is the $m \times 1$ vector of actuator torques, and $\boldsymbol{\Lambda} = \text{diag}\ (\omega_1^2, \omega_2^2, \ldots, \omega_{nq}^2)$ where ω_i is the frequency of the ith elastic mode. The rigid-body parameters and the first 10 elastic frequencies are given in table I. Each value of ζ_i is assumed to be 0.01 for $i = 1, 2, \ldots, n_q$.

Normally, the sensors used include attitude and rate sensors. The three-axis attitude $\mathbf{y}_a$ at a sensor (e.g., a star tracker) location is given by

$$\mathbf{y}_a = \boldsymbol{\alpha}_s + \boldsymbol{\Psi}\mathbf{q} \tag{3}$$

where $\boldsymbol{\Psi}$ is the $3 \times n_q$ mode-slope matrix at the sensor location. If an attitude rate sensor (e.g., a rate gyro) is used, the sensor output $\mathbf{y}_r$ is given by an equation similar to equation (3), except that $\boldsymbol{\alpha}_s$ and $\mathbf{q}$ are replaced by $\dot{\boldsymbol{\alpha}}_s$ and $\dot{\mathbf{q}}$, respectively. The torque actuators and the attitude and rate sensors are assumed to be located near the top and bottom of the mast as shown in figure 1. The elastic deformation caused by some of the flexible modes is shown in figure 2.

Define $\mathbf{x} = \left(\boldsymbol{\alpha}_s^T, \dot{\boldsymbol{\alpha}}_s^T, \mathbf{q}^T, \dot{\mathbf{q}}^T\right)^T$; then the state space model can be written in the following form:

$$\dot{\mathbf{x}} = \mathbf{A}_F\mathbf{x} + \mathbf{B}_F\mathbf{u} \tag{4}$$

$$\mathbf{y}_a = \mathbf{C}_F\mathbf{x} \tag{5}$$

The sensor and actuator noise are not considered in the design process in this paper; however, it will have to be included when computing the rms

pointing errors. Ignoring the noise, the transfer matrix between the input (three-axis torque) and the output (three-axis attitude) is given by

$$\mathbf{G}_F(s) = \mathbf{G}_1(s) + \mathbf{G}_2(s) \tag{6}$$

where

$$\mathbf{G}_1(s) = \frac{\mathbf{I}_s^{-1}}{s} \tag{7}$$

$$\mathbf{G}_2(s) = \sum_{i=1}^{n_q} \frac{\boldsymbol{\Psi}_i \boldsymbol{\Phi}_i^T}{s^2 + 2\zeta_i\omega_i s + \omega_i^2} \tag{8}$$

where $\boldsymbol{\Psi}_i$ and $\boldsymbol{\Phi}_i$ represent the mode-slope matrices at the sensor and actuator locations corresponding to the ith mode. Numerical data used to define equations (4) through (8) and a discussion of the model characteristics are given in the appendix.

4. Design Objectives

The basic design objectives for the control systems are (1) to obtain sufficiently high bandwidth (i.e., closed-loop frequencies corresponding to the rigid-body modes) and satisfactory closed-loop damping ratios for rigid-body and structural modes; and (2) to obtain satisfactory rms pointing errors, feed motion errors, and surface errors. The first design objective arises from the need to obtain sufficiently fast error decay when a step disturbance (such as sudden thermal distortion caused by entering or leaving the Earth's shadow) occurs. The second design objective arises from the RF performance requirements. These two objectives may not necessarily be compatible. For example, the use of increased feedback gains for obtaining higher bandwidth and damping ratios will in general, result in higher rms errors (because of the amplified effect of sensor noise) beyond a certain point. Therefore, it is necessary to carefully consider the trade-offs between the speed of response and lower rms error. In this study, the main control system specification is to ensure a minimum bandwidth of 0.1 rad/sec for the closed-loop system. The upper limit on the low frequency gain is not specified but it is desired that it should be as high as possible.

5. Design Procedure

The LQG/LTR method (refs. 1 through 3) basically consists of the following steps:

1. Define a "design" model of the nominal plant which is an acceptable low frequency representation. Define the high frequency uncertainty (robustness) barrier and the low frequency performance barrier.

2. Design a full state feedback compensator based on the steady-state Kalman-Bucy filter (KBF). This assumes that the loop is broken at the plant output. Adjust the weighting matrices in the KBF design until its frequency response meets the robustness specifications at high frequencies and bandwidth specification at low frequencies.

3. Design an LQ regulator to asymptotically "recover" the frequency response obtained in step 2.

4. Verify stability, robustness, and performance for the entire closed-loop system.

The first step, which consists of the definition of the plant and the uncertainty (robustness) barrier, is often the most important one. The basic problem in controlling a flexible structure is the presence of a large number of lightly damped structural modes. Practical limitations necessitate the use of reduced-order controllers. Therefore, the uncontrolled modes and the error in the knowledge of the controlled modes together represent uncertainty. Since the number of structural modes is usually large and finite-element modeling accuracy typically decreases with increasing model frequency, the design model should consist of rigid-body plus the first few elastic modes. In order to obtain an acceptable low frequency representation, the design model must include at least the three rigid-body modes. The uncertainty barrier is a measure of the plant uncertainty at high frequencies. The plant uncertainty can be represented as either multiplicative or additive uncertainty (fig. 3). The LQG/LTR approach requires the characterization of the uncertainty in terms of a frequency-dependent upper bound. Frequency domain sufficient conditions are used to test the robustness in the presence of uncertainties within that bound.

For the case of multiplicative uncertainty, $\mathbf{L}_p(j\omega)$ of figure 3(a), with the loop broken at the plant output, the closed-loop system is stable if

$$\overline{\sigma}\left[\mathbf{L}_p(j\omega) - \mathbf{I}\right] \leq \underline{\sigma}\left\{\mathbf{I} + \left[\mathbf{G}_p(j\omega)\,\mathbf{G}_c(j\omega)\right]^{-1}\right\} \tag{9}$$

where $\mathbf{G}_p(j\omega)$ and $\mathbf{G}_c(j\omega)$ are the design model (plant) and compensator transfer matrices, and $\overline{\sigma}$ and $\underline{\sigma}$ denote the largest and the smallest singular values of the argument matrix, respectively. At high frequencies, assuming $\|\mathbf{L}_p(j\omega)\| \gg 1$ and $\|\mathbf{G}_p(j\omega)\,\mathbf{G}_c(j\omega)\| \ll 1$ (ref. 8) (approximately) yields

$$\overline{\sigma}(\mathbf{G}_p\mathbf{G}_c) < 1/\overline{\sigma}(\mathbf{L}_p) \tag{10}$$

For notational convenience, the argument "$j\omega$" has been dropped.

The uncertainty (or robustness) barrier is an upper bound $l_m(\omega)$ on $\overline{\sigma}(\mathbf{L}_p)$. The system is stable

in the presence of such unstructured uncertainties if $\bar{\sigma}[\mathbf{G}_p\mathbf{G}_c] < l_m^{-1}(\omega)$ at high frequencies.

When the additive uncertainty formulation (fig. 3(b)) is used, a sufficient condition for stability robustness is given by (ref. 10)

$$\bar{\sigma}(\Delta\mathbf{G}) < \frac{\underline{\sigma}(\mathbf{I}+\mathbf{G}_p\mathbf{G}_c)}{\bar{\sigma}(\mathbf{G}_c)} \tag{11}$$

At high frequencies, assuming $\|\mathbf{G}_p\mathbf{G}_c\| \ll 1$ (ref. 10) (approximately) yields

$$\bar{\sigma}(\mathbf{G}_c) < \frac{1}{\bar{\sigma}(\Delta\mathbf{G})} \tag{12}$$

That is, the compensator must roll off sufficiently rapidly at high frequencies. The main feature of the LQG/LTR approach is to first design a full state compensator (based on KBF) which has the behavior of the desired loop transfer matrix (i.e., the loop gain $\mathbf{G}_p\mathbf{G}_c$). Therefore (from step 2), any loop shaping should involve the product $\mathbf{G}_p\mathbf{G}_c$ rather than $\mathbf{G}_c$ alone as in equations (11) and (12). Assuming that $\mathbf{G}_p$ is a square matrix,

$$\mathbf{G}_c = \mathbf{G}_p^{-1}(\mathbf{G}_p\mathbf{G}_c) \tag{13}$$

$$\bar{\sigma}(\mathbf{G}_c) \le \bar{\sigma}(\mathbf{G}_p^{-1})\,\bar{\sigma}(\mathbf{G}_p\mathbf{G}_c)$$

or

$$\bar{\sigma}(\mathbf{G}_c) \le \underline{\sigma}^{-1}(\mathbf{G}_p)\,\bar{\sigma}(\mathbf{G}_p\mathbf{G}_c) \tag{14}$$

Using equations (14) and (11), the following sufficient condition for stability robustness is obtained:

$$\frac{\underline{\sigma}(\mathbf{I}+\mathbf{G}_p\mathbf{G}_c)\,\underline{\sigma}(\mathbf{G}_p)}{\bar{\sigma}(\mathbf{G}_p\mathbf{G}_c)} > \bar{\sigma}(\Delta\mathbf{G}) \tag{15}$$

The second step in the design procedure is to design a full state feedback compensator having desirable singular value properties. The performance of the closed-loop system depends on the low frequency gain and the crossover frequency of the loop transfer matrix $\mathbf{G}_p\mathbf{G}_c$, that is, on the behavior of $\underline{\sigma}[\mathbf{G}_p\mathbf{G}_c]$. Larger low frequency gain and crossover frequency indicates better tracking performance. Thus, $\underline{\sigma}[\mathbf{G}_p\mathbf{G}_c]$ should lie above the performance specification as shown in figure 4(a). The other requirement is the stability robustness in the presence of model uncertainties. If the multiplicative uncertainty formulation is used, according to equation (10), the $\bar{\sigma}[\mathbf{G}_p\mathbf{G}_c]$ plot should pass under the robustness barrier $\bar{\sigma}^{-1}(\mathbf{L}_p)$ at high frequencies (fig. 4(a)). On the other hand, if the additive formulation is used, the robustness condition, equation (15), should be satisfied (fig. 4(b)).

The advantage of an LQG-based full state design is that it has excellent classical properties, and its frequency response can be shaped in the desired manner by varying the weighting matrices (ref. 2). As discussed in reference 2, this design can be accomplished by using the linear-quadratic regulator (LQR) Riccati equation if the loop is broken at the plant input, or the KBF Riccati equation if it is broken at the point where the residual signal enters the KBF. Herein we select the latter because the objective is to control the attitude output. This selection is also consistent with references 3 and 4. The KBF equations are

$$\mathbf{A}\boldsymbol{\Sigma} + \boldsymbol{\Sigma}\mathbf{A}^T + \mathbf{L}\mathbf{L}^T - \frac{\boldsymbol{\Sigma}\mathbf{C}^T\mathbf{C}\boldsymbol{\Sigma}}{\mu} = 0 \tag{16}$$

$$\mathbf{H} = \frac{\boldsymbol{\Sigma}\mathbf{C}^T}{\mu} \tag{17}$$

where $\mathbf{L}$ and μ are the design parameters, $\mathbf{L}$ being an $n \times m$ matrix and μ a scalar, $\mathbf{H}$ is the KBF gain matrix, and $\boldsymbol{\Sigma}$ is the corresponding Riccati matrix. The KBF loop transfer matrix is given by

$$\mathbf{G}_{KF}(s) = \mathbf{C}(s\mathbf{I} - \mathbf{A})^{-1}\mathbf{H} \tag{18}$$

Generally, the frequency response $\sigma[\mathbf{G}_{KF}(j\omega)]$ would shift higher as μ decreases, and the crossover frequency can be adjusted by changing $\mathbf{L}$.[2]

Having obtained satisfactory singular value behavior of KBF, the third step is to design an LQR to "recover" the desired frequency response. This is accomplished by solving the algebraic Riccati equation

$$\mathbf{A}^T\mathbf{P} + \mathbf{P}\mathbf{A} - \mathbf{P}\mathbf{B}\mathbf{B}^T\mathbf{P} + \bar{q}\mathbf{C}^T\mathbf{C} = 0 \tag{19}$$

where $\mathbf{P}$ is the Riccati matrix and $\bar{q}$ is a positive scalar. It has been proven in references 1 and 2 that the loop transfer matrix $\mathbf{G}_p\mathbf{G}_c$ for the overall system (consisting of the plant, the KBF, and the LQR) tends to $\mathbf{G}_{KF}(s)$ as $\bar{q} \to \infty$, provided that the open-loop plant has no transmission zeros in the right half-plane. After recovery, $\mathbf{G}_c(s)$ is given by

$$\mathbf{G}_c(s) = \mathbf{G}(s\mathbf{I} - \mathbf{A} + \mathbf{B}\mathbf{G} + \mathbf{H}\mathbf{C})^{-1}\mathbf{H}$$

[2] Ibid.

A block diagram of the compensator is shown in figure 5.

Since the compensation obtained has no guaranteed robustness properties, the last step will consist of testing the eigenvalues of the entire closed-loop system to ensure the stability and robustness. The overall closed-loop system is

$$\begin{bmatrix} \dot{\mathbf{x}} \\ \dot{\hat{\mathbf{x}}} \end{bmatrix} = \begin{bmatrix} \mathbf{A}_F & -\mathbf{B}_F\mathbf{G} \\ \mathbf{H}\mathbf{C}_F & \mathbf{A} - \mathbf{B}\mathbf{G} - \mathbf{H}\mathbf{C} \end{bmatrix} \begin{bmatrix} \mathbf{x} \\ \hat{\mathbf{x}} \end{bmatrix}$$

where the subscript F is used to denote the full-order nominal plant, and $\hat{\mathbf{x}}$ denotes the state estimate for the design model. If instability is discovered, it will be necessary to return to step 2 and redesign the KBF for lower bandwidth and the LQR for robustness recovery. If this does not produce satisfactory results, it would then be necessary to return to step 1 and include more elastic modes in the design model. Application of the foregoing LQG/LTR procedure for the hoop/column antenna is described in the following section.

6. Numerical Results

Before applying the LQG/LTR method for compensator design, the controllability, observability, and invariant zero properties of the plant (with respect to different sensor/actuator locations) were studied. Based on these studies (presented in detail in the appendix), location 1 shown in figure 1 was selected for the sensors and the actuators. The LQG/LTR procedure was subsequently applied, first by using only attitude sensors and then by using attitude and attitude-rate sensors. The computations were performed by using the LQG design package ORACLS (ref. 11) augmented with frequency domain singular value analysis software.

6.1. Controller Design Using Attitude Feedback

In this section, the results of the application of the LQG/LTR procedure are presented when only attitude feedback is employed. The studies are performed by using the design model consisting of (1) only rigid-body model ($n = 6$, $n_q = 0$), (2) rigid-body and the first flexible mode ($n = 8$, $n_q = 1$), and (3) rigid-body and the first three flexible modes ($n = 12$, $n_q = 3$). The measurements available are the three attitude angles at location 1. One three-axis torque actuator is used at the same location. The compensator is designed based on these sensors and actuators. The results of the designs are presented in figures 6 through 23.

The largest and the smallest singular values of the rigid-body transfer matrix ($n = 6$) are plotted in figure 6. The corresponding additive uncertainty $\Delta\mathbf{G}$, which consists of the (20th order) flexible dynamics, is plotted in figure 7. Figure 6 clearly shows the roll-off behavior of the plant, which is of the order of $1/s^2$. Figure 7 indicates the presence of poles near the undamped flexible mode frequencies of 0.75 rad/sec, 1.35 rad/sec, etc. Also, the pole near the first mode frequency near 0.75 rad/sec produces the highest peak. (The importance of this fact is seen later when the stability condition is violated at this point.) It can also be seen that a zero is present near 5 rad/sec.

Based on this rigid design model, the following choice of $\mathbf{L}$ and μ were made after a number of trials:

$$\mathbf{L} = \begin{bmatrix} 0_3 \\ \hline 10^{-2}\mathbf{I}_3 \end{bmatrix} \qquad \mu = 1$$

The objective is to obtain a bandwidth of at least 0.1 rad/sec. The resulting values of the "desired" loop gain matrix $\mathbf{G}$ are shown in figure 8.

The standard LQG/LTR procedure requires the definition of the desired loop transfer characteristics (see step 2 in section 5). That is, $\underline{\sigma}(\mathbf{G}_{KF})$ must satisfy the low frequency performance specifications, and $\overline{\sigma}(\mathbf{G}_{KF})$ must satisfy the high frequency robustness specifications. Thus, in the presence of additive uncertainty $\Delta\mathbf{G}$, the procedure states that the robustness condition

$$\frac{\underline{\sigma}(\mathbf{I} + \mathbf{G}_{KF})\underline{\sigma}(\mathbf{G}_p)}{\overline{\sigma}(\mathbf{G}_{KF})} > \overline{\sigma}(\Delta\mathbf{G})$$

should be satisfied. However, in the computations performed, it was found that this condition makes the desired design ($\mathbf{G}_{KF}$) extremely conservative in the sense that higher loop gains can be used without causing instability. Therefore, recovering this conservative loop gain yields a compensator with poor performance. This fact led to a modification of the LQG/LTR procedure. In particular, this robustness test on $\mathbf{G}_{KF}$ is omitted in the modified procedure. Instead, the recovery is carried out first, and then the (less conservative) stability test (eq. (11)) is applied directly for the compensator $\mathbf{G}_c$.

With the use of the recovery procedure, the compensator is obtained for this case with $\overline{q} = 10^4$. The resulting stability test (eq. (11)) is shown in figure 9. It is seen that the stability margin is lowest at the first mode frequency (0.75 rad/sec). Any increase in the gain (obtained by $\overline{q} > 10^4$) resulted in the violation of the stability condition at that point. The resulting singular values of the compensator $\mathbf{G}_c$ are given in figure 10, which shows that the compensator is of the "lead-lag" type. The overall loop

bandwidth is obtained from the singular values of the loop transfer function $\mathbf{G}_p\mathbf{G}_c$ shown in figure 11. It is seen that the bandwidth (i.e., the frequency at which $\underline{\sigma}(\mathbf{G}_p\mathbf{G}_c) = 1$) is far short of the required 0.1 rad/sec. The plots roll off as $1/s^2$ (40 dB/decade) and indicate the recovery process. In order to increase the bandwidth, the regulator gain has to be increased by increasing $\bar{q}$. However, this results in the violation of the stability condition (eq. (11)). Thus it became evident that, with the rigid-body design model, it is not possible to meet the performance specifications.

To overcome these problems, the inclusion of the first flexible mode (0.75 rad/sec) in the design model was considered. The inclusion of the first flexible mode, which is predominantly a torsion mode, results in a design model of order 8. The singular value plots for $\mathbf{G}_p$ and $\Delta\mathbf{G}$ are given in figures 12 and 13. Figure 12 indicates the presence of a pole of $\mathbf{G}_p$ near 0.75 rad/sec and a zero near 0.082 rad/sec. The singular values of $\Delta\mathbf{G}$ in figure 13 are an order of magnitude lower than those in figure 7 (wherein $\Delta\mathbf{G}$ consisted of *all* the flexible modes). The first peak of $\bar{\sigma}(\Delta\mathbf{G})$ occurs at 1.35 rad/sec, which is the frequency of the second mode. This is the critical point in the stability test (eq. (11)). After a number of trials, the following choice of $\mathbf{L}$ and μ was made:

$$\mathbf{L} = \left[\begin{array}{c|c} 0_3 & \\ \hline 10^{-2}\mathbf{I}_3 & \\ \hline 10^{-2}\mathbf{I}_2 & 0 \end{array}\right] \qquad \mu = 1$$

The singular values of $\mathbf{G}_{KF}$ are plotted in figure 14. The recovery is obtained for $\bar{q} = 10^5$ and the stability test is shown in figure 15.

Figure 15 indicates the critical point to be about 0.28 rad/sec. There is a good margin at the peaks of $\Delta\mathbf{G}$ due to upward sloping of the upper curve. The resulting compensator is shown in figure 16. The compensator has a pole at about 0.25 rad/sec and a zero at 0.8 rad/sec. The resulting loop transfer function ($\mathbf{G}_p\mathbf{G}_c$) plots are shown in figure 17. The plots indicate that the required 0.1 rad/sec bandwidth is not obtained (although it is much higher than the rigid-model case). Any increase in the gain (for $\bar{q} > 10^5$) was found to result in the violation of the stability condition (eq. (11)). Figure 17 indicates the presence of the open-loop invariant zero near 0.082 rad/sec, which was also confirmed by independent computations. This zero is almost on the imaginary axis (i.e., the transfer matrix is close to being nonminimum phase). Therefore (as would be expected), the recovery procedure is not very effective for making $\mathbf{G}_p\mathbf{G}_c$ approximate $\mathbf{G}_{KF}$.

In order to improve the performance further, the next step was to include the first three flexible modes in the design model. It is logical to do this because they represent the first modes about each axis, that is, the first torsion mode and the first bending modes in the X-Z and Y-Z planes. Thus the order of the design model was 12. The singular value plots for $\mathbf{G}_p$ and $\Delta\mathbf{G}$ are shown in figures 18 and 19, respectively. Figure 18 indicates that $\mathbf{G}_p$ has zeros near 0.082 and 0.22 rad/sec and poles near 0.75, 1.35, and 1.7 rad/sec. It is seen from the $\Delta\mathbf{G}$ plot (fig. 19) that $\bar{\sigma}$ is considerably lower than that in figures 7 and 13. After numerous trials, the following choice of the $\mathbf{L}$ matrix and the scalar μ were made:

$$\mathbf{L} = \left[\begin{array}{c|c} 0_3 & \\ \hline 10^{-1}\mathbf{I}_3 & \\ \hline 10^{-4}\mathbf{I}_2 & 0 \\ \hline 10^{-4}\mathbf{I}_2 & 0 \\ \hline 10^{-4}\mathbf{I}_2 & 0 \end{array}\right] \qquad \mu = 1$$

The resulting $\mathbf{G}_{KF}$ with the desired characteristics is shown in figure 20. The recovery was accomplished with $\bar{q} = 10^{10}$. The stability test is shown in figure 21. It can be seen that condition (11) is satisfied with a wide margin. Also, at the peaks for $\Delta\mathbf{G}$ (at 8 rad/sec), the upper curve slopes upward, indicating good tolerance of high frequency uncertainty. The limit for increasing the gain (indicated by the lowest point in the upper curve in figure 21) occurs at about 0.3 rad/sec. The resulting compensator $\mathbf{G}_c$ is shown in figure 22. The gain of $\mathbf{G}_c$ is much higher than that obtained in the previous cases. Generally, the LQG/LTR technique attempts to choose $\mathbf{G}_c$ in such a way that $\mathbf{G}_p$ is approximately inverted and the product $\mathbf{G}_p\mathbf{G}_c$ is replaced by $\mathbf{G}_{KF}$. The three-mode design plant shown in figure 18 has elastic mode eigenvalues at $-0.0075 \pm j0.75$, $-0.0135 \pm j1.35$, and $-0.017 \pm j1.7$. Figure 22 shows that $\mathbf{G}_c$ has zeros with frequencies near these locations. The design model also has transmission zeros at

$$(-0.9 \times 10^{-4}) \pm j0.082$$
$$(-0.37 \times 10^{-3}) \pm j0.22$$
$$(-0.29 \times 10^{-3}) \pm j0.22$$

The zeros of the design model are too close to the $j\omega$ axis and tend to numerically behave as nonminimum phase. Some alleviation is obtained by the compensator pole near 0.4 rad/sec. The plots for the loop transfer matrix $\mathbf{G}_p\mathbf{G}_c$ are given in figure 23. It is seen that a bandwidth of 0.1 rad/sec is obtained except for the presence of the invariant zero near 0.082 rad/sec which causes some deterioration of performance. This zero is invariant under feedback and depends on the sensor/actuator locations. At higher frequencies, $\mathbf{G}_p\mathbf{G}_c$ rolls off at 60 dB/decade. Also, $\overline{\sigma}$ and $\underline{\sigma}$ are closely spaced; this indicates good system behavior. The compensator gains (i.e., the regulator and filter gain matrices) for this case are shown in table II, and the complete closed-loop eigenvalues are shown in table III.

Thus it is seen that the inclusion of the first three modes in the design model yields a robust compensator which also meets the bandwidth specifications.

6.2. Controller Design Using Attitude and Rate Feedback

In this section, the numerical results for the design using the feedback of both attitude and rate are discussed. Similar to the attitude feedback case, one three-axis torque actuator is used at location 1. One three-axis attitude sensor and one three-axis attitude rate sensor are assumed to be located at the same location (i.e., location 1). Thus the plant $\mathbf{G}_p(s)$ is now 6×3, with the three attitude angles and the three attitude rates being the outputs and three torques being the inputs. The compensator $\mathbf{G}_c(s)$ is then 3×6. The resulting loop is shown in figure 24(a). The realization of $\mathbf{G}_c$ consists of a KBF using the six measurements, followed by the $3 \times n$ LQ regulator gain matrix $\mathbf{G}$, where n is the order of the design model. As in the attitude feedback design, three cases are considered, with the design model consisting of

Case a: Only rigid-body modes ($n = 6$)

Case b: Rigid-body and the first flexible mode ($n = 8$)

Case c: Rigid-body and the first three flexible modes ($n = 12$)

As in the design with attitude feedback, the second and third modes (being bending modes about X- and Y-axes) were not considered separately, and hence a three-mode model was considered after the one-mode model.

For the design with attitude and rate feedback, the transfer matrix for the design model is

$$\mathbf{G}_p(s) = \begin{bmatrix} \widehat{\mathbf{G}}(s) \\ s\widehat{\mathbf{G}}(s) \end{bmatrix}_{6\times 3}$$

where $\widehat{\mathbf{G}}(s)$ is the transfer function matrix with attitude as the output. Thus $\mathbf{G}_p(s)$ is always of rank 3, and $\underline{\sigma}(\mathbf{G}_p\mathbf{G}_c) = 0$. Therefore the loop gain can never satisfy the bandwidth specifications. To overcome this difficulty, we consider only the attitude measurements for performance evaluation. In other words, the compensator $\mathbf{G}_c$ uses both the attitude and the rate as its inputs (and has the dimension 3×6), but we consider only the 3×1 attitude in the performance evaluation. Figure 24(b) shows the loop with a slight modification to account for this. The loop gain for the system is

$$\mathbf{G}_L(s) = [\mathbf{I}_3 0_3]\,[\mathbf{G}_p\mathbf{G}_c]\,[\mathbf{I}_3 s\mathbf{I}_3]^T$$

and one needs to check $\underline{\sigma}(\mathbf{G}_L)$ as the measure of performance (i.e., bandwidth). Similarly, in the KBF design for the desired loop gain, one needs to check $\underline{\sigma}$ of

$$\widehat{\mathbf{G}}_{KF} = [\mathbf{I}_3 0_3]\,\mathbf{G}_{KF}\,[\mathbf{I}_3 s\mathbf{I}_3]^T$$

As in the previous case, the robustness test (eq. (11)) is carried out by using (the 6×6) $\mathbf{G}_p\mathbf{G}_c$ (and not $\mathbf{G}_{KF}$) although $\underline{\sigma}(\mathbf{G}_L)$ is used as the measure of performance.

The design procedure involves first solving the KBF equations with suitable choices of $\mathbf{L}$ and μ to obtain the desired performance characteristics $\underline{\sigma}(\mathbf{G}_{KF})$. The next step is to recover this desirable loop gain by increasing $\overline{q}$ the LQ regulator design. However, the loop transfer recovery can be obtained only if the number of inputs is greater than or equal to the number of outputs, which is not the case here. Based on the experience with attitude feedback designs, $\overline{q}$ cannot be usually increased sufficiently to obtain recovery in the desired frequency range (because the stability condition is violated). Therefore, although asymptotic recovery is not possible, a decent bandwidth should still be obtainable by increasing $\overline{q}$.

Figure 25 shows the frequency response of $\mathbf{G}_p$ for case a, i.e., rigid-body design model. The σ-plots of $\Delta\mathbf{G}$ are shown in figure 26. After a number of trials, the following $\mathbf{L}$ and μ were used:

$$\mathbf{L} = \left[\begin{array}{c|c} 0_3 & 0_3 \\ \hline 0_3 & 10^{-2}\mathbf{I}_3 \end{array}\right]_{6\times 6} \qquad \mu = 1$$

The resulting σ-plots of $\hat{\mathbf{G}}_{KF}$ are shown in figure 27. After the KBF design, the recovery procedure is carried out by increasing $\overline{q}$. The largest $\overline{q}$ without causing instability (as indicated by the stability test (eq. (11)), which is shown in fig. 28) was $\overline{q} = 10^4$. Figures 29 and 30, respectively, show the σ-plots of $\mathbf{G}_L$ and $\hat{\mathbf{G}}_c \triangleq \mathbf{G}_c\,[\mathbf{I}_3 s\mathbf{I}_3]^T$. It is seen from figure (29) that the bandwidth requirement of 0.1 rad/sec is practically impossible to meet using a rigid model.

For case b, the design model consisted of the rigid-body and the first flexible modes. Figures 31 and 32 show the σ-plots for $\mathbf{G}_p$ and $\Delta\mathbf{G}$, and figure 33 shows the plots for $\hat{\mathbf{G}}_{KF}$ which was obtained with

$$\mathbf{L} = \left[\begin{array}{c|c} 0_3 & 0_3 \\ \hline 0_3 & 10^{-1}\mathbf{I}_3 \\ \hline 10^{-1}\mathbf{I}_2 & 0_{2\times 4} \end{array}\right]_{8\times 6} \qquad \mu = 1$$

The largest $\overline{q}$ in the LQ regulator design (which does not cause instability) was $\overline{q} = 10^5$, and the corresponding stability test (eq. (11)) is shown in figure 34. The σ-plots of $\mathbf{G}_L$ and $\hat{\mathbf{G}}_c$ are shown in figures 35 and 36, respectively. It is clear that the bandwidth specification cannot be met with this model.

In order to improve the performance, the first three flexible modes were next included in the model (in addition to the rigid modes). Figures 37 and 38, respectively, show the σ-plots of $\mathbf{G}_p$ and $\Delta\mathbf{G}$. The $\hat{\mathbf{G}}_{KF}$ plot shown in figure 39 was obtained for the following choice of $\mathbf{L}$ and μ:

$$\mathbf{L} = \left[\begin{array}{c|c} 0_3 & 0_3 \\ \hline 0_3 & 10^{-1}\mathbf{I}_3 \\ \hline 10^{-1}\mathbf{I}_2 & 0_{2\times 4} \\ \hline 10^{-1}\mathbf{I}_2 & 0_{2\times 4} \\ \hline 10^{-1}\mathbf{I}_2 & 0_{2\times 4} \end{array}\right]_{12\times 6} \qquad \mu = 1$$

The largest permissible $\overline{q}$ (without causing instability) was 10^8, and the resulting stability test is shown in figure 40. The σ-plots of $\mathbf{G}_L$ and $\hat{\mathbf{G}}_c$ are shown in figures 41 and 42. As shown in figure 41, the bandwidth requirement is not satisfactorily met. In addition, the presence of a transmission zero near 0.082 rad/sec introduces a notch in the $\sigma(\mathbf{G}_L)$ plots similar to the attitude feedback case. The compensator gains and the closed-loop eigenvalues of the complete system are given in tables IV and V, respectively.

Based on these results, it appears that designing with attitude feedback only allows for higher performance bandwidth while maintaining stability robustness. The reason can be seen from a comparison of the stability robustness condition (eq. (11)) in both the attitude and attitude and rate cases. In the attitude case, $\Delta\mathbf{G}_{3\times 3}$ rolls off as $1/s^2$. For attitude and rate, it rolls off as $1/s$. Since, in both situations, $\mathbf{G}_c$ behaves as $1/s$ and $\underline{\sigma}(\mathbf{I}+\mathbf{G}_p\mathbf{G}_c) \to \mathbf{I}$ for large values of s, condition (11) is ultimately satisfied. However, comparing figures 21 and 40 shows that the attitude and rate case experiences greater difficulty in the frequency region containing the peak of $\overline{\sigma}(\Delta\mathbf{G})$. It can be shown that

$$\overline{\sigma}(\Delta\mathbf{G}_{6\times 3}(j\omega)) = (1+\omega^2)^{1/2}\,\overline{\sigma}(\Delta\mathbf{G}_{3\times 3}(j\omega))$$

The $(1+\omega^2)^{1/2}$ magnifies $\overline{\sigma}(\mathbf{G}(j\omega))$ and causes a lower value of $\overline{q}$ in the recovery process and a more conservative performance bandwidth. This difficulty could possibly be overcome by a different choice of $\mathbf{L}$ and μ.

7. Concluding Remarks

The LQG/LTR (linear-quadratic-Gaussian/loop transfer recovery) multivariable frequency domain technique was employed in the design of an attitude control system for large flexible space antenna. The LQG/LTR method was noted to be especially attractive for overcoming spillover effects common to large space structures control problem modeled by using finite-element data. The design objective of avoiding excitation of higher order modes while satisfying performance criteria was met by including these modes in the robustness uncertainty barrier.

Design was based on a reduced-order model chosen as the rigid-body dynamics plus the fewest number of low frequency vibrational modes necessary to meet a desired closed-loop bandwidth. Inclusion of the first three vibrational modes (corresponding to the three axes) was found to be necessary to meet a bandwidth of 0.1 rad/sec. For higher bandwidths, design models with greater than three modes would be needed. A satisfactory control design was obtained by using only a single collocated pair of three-axis attitude sensor and torque actuator for this

problem. An investigation employing attitude-rate sensors in addition to the attitude sensors showed no improvement over this arrangement.

Performance degradation was observed due to the presence of invariant zeros within the design bandwidth. These zeros were unavoidable given the prescribed sensor/actuator locations and emphasized the fact that consideration should be given to control aspects right from the early design phases of large space structures.

A modification of the standard LQG/LTR procedure was introduced in which the robustness test was performed with the the full LQG compensator instead of the intermediate Kalman filter design. This approach was found to produce higher gain compensators and helped overcome the basic conservativeness shortcoming of the LQG/LTR approach.

NASA Langley Research Center
Hampton, VA 23665-5225
April 15, 1986

Appendix

System Characteristics of Hoop/Column Antenna Mathematical Models

In this appendix, the state-variable realizations employed in the LQG/LTR design studies are analyzed to determine their innate controllability, observability, and invariant zero properties. Computational results are presented for a single three-axis torque actuator and a collocated attitude sensor. A combined attitude and rate sensor case yielded the same results.

The hoop/column antenna model given by equations (4) and (5) are

$$\dot{\mathbf{x}} = \mathbf{A}_F\mathbf{x} + \mathbf{B}_F\mathbf{u} \tag{A1}$$

$$\mathbf{y}_a = \mathbf{C}_F\mathbf{x} \tag{A2}$$

In equation (A1), with $n = 6 + 2n_q$,

$$\mathbf{A}_F = \begin{bmatrix} \mathbf{A}_R & 0 \\ 0 & \mathbf{A}_E \end{bmatrix}_{n\times n} \tag{A3}$$

$$\mathbf{A}_R = \begin{bmatrix} 0 & \mathbf{I}_3 \\ 0 & 0 \end{bmatrix}_{6\times 6} \tag{A4}$$

$$[\mathbf{A}_E]_{2n_q\times 2n_q} = \text{diag}\left(\mathbf{A}_E^1, \mathbf{A}_E^2, \ldots, \mathbf{A}_E^{n_q}\right) \tag{A5}$$

and

$$\mathbf{A}_E^i = \begin{bmatrix} 0 & 1 \\ -\omega_i^2 & -2\varsigma_i\omega_i \end{bmatrix}_{2\times 2} \qquad (i = 1, 2, \ldots, n_q) \tag{A6}$$

Equation (A4) describes the plant rigid-body motion, and equation (A5) describes the elastic motion contribution when n_q vibrational modes are included in the design model. Frequencies $\omega_i (i = 1, 2, \ldots, 10)$ are given in table I for a 122-m-diameter hoop/column structure. The damping ratios ς_i are taken as $\varsigma_i = 0.01 (i = 1, 2, \ldots, 10)$. Eigenvalues of $\mathbf{A}_E^i (i = 1, 2, \ldots, 10)$ are as given in table AI. Employing a single three-axis torque actuator gives

$$\mathbf{B}_F = \begin{bmatrix} 0_3 \\ \mathbf{I}_s^{-1} \\ \hline \mathbf{V}_B \end{bmatrix} \begin{matrix} \Big\} (6\times 3) \\ \\ \Big\} (2n_q \times 3) \end{matrix} \tag{A7}$$

where, in units of $(\text{ft-lb-sec}^2)^{-1}$,

$$\mathbf{I}_s^{-1} = \text{diag}\,(2.37\times 10^{-7}, 2.37\times 10^{-7}, 3.09\times 10^{-7}) \tag{A8}$$

The matrix $\mathbf{V}_B$ depends on actuator location.

TABLE AI. EIGENVALUES OF ELASTIC MODES

Mode	Eigenvalue
1	$-0.0075 \pm j0.75$
2	$-0.0135 \pm j1.35$
3	$-0.0170 \pm j1.70$
4	$-0.0318 \pm j3.18$
5	$-0.0453 \pm j4.53$
6	$-0.0559 \pm j5.59$
7	$-0.0578 \pm j5.78$
8	$-0.0684 \pm j6.84$
9	$-0.074 \pm j7.4$
10	$-0.0878 \pm j8.78$

For actuator location 1 (fig. 1):

$$\mathbf{V}_B = \begin{bmatrix} 0 & 0 & 0 \\ 6.3 \times 10^{-5} & 0 & -5.04 \times 10^{-3} \\ 0 & 0 & 0 \\ 0 & -2.91 \times 10^{-3} & 0 \\ 0 & 0 & 0 \\ 3.71 \times 10^{-3} & 0 & 5.45 \times 10^{-4} \\ 0 & 0 & 0 \\ -7.49 \times 10^{-7} & 0 & -8.45 \times 10^{-6} \\ 0 & 0 & 0 \\ -6.21 \times 10^{-4} & 0 & -5.6 \times 10^{-5} \\ 0 & 0 & 0 \\ 5.55 \times 10^{-6} & 0 & -3.19 \times 10^{-4} \\ 0 & 0 & 0 \\ 0 & -5.00 \times 10^{-4} & 0 \\ 0 & 0 & 0 \\ 1.1 \times 10^{-3} & 0 & -2.23 \times 10^{-4} \\ 0 & 0 & 0 \\ 0 & -3.04 \times 10^{-3} & 0 \\ 0 & 0 & 0 \\ 2.43 \times 10^{-3} & 0 & -1.05 \times 10^{-4} \end{bmatrix} \begin{matrix} \}\text{mode 1} \\ \\ \}\text{mode 2} \\ \\ \}\text{mode 3} \\ \\ \\ \\ \\ \\ \\ \\ \\ \\ \\ \\ \\ \\ \}\text{mode 10} \end{matrix} \tag{A9}$$

For actuator location 2 (fig. 1):

$$\mathbf{V}_B = \begin{bmatrix} 0 & 0 & 0 \\ -1.81 \times 10^{-5} & 0 & -1.62 \times 10^{-5} \\ 0 & 0 & 0 \\ 0 & 2.52 \times 10^{-4} & 0 \\ 0 & 0 & 0 \\ -3.76 \times 10^{-4} & 0 & 1.22 \times 10^{-5} \\ 0 & 0 & 0 \\ 1.70 \times 10^{-7} & 0 & -1.97 \times 10^{-4} \\ 0 & 0 & 0 \\ -1.08 \times 10^{-2} & 0 & -4.09 \times 10^{-6} \\ 0 & 0 & 0 \\ 6.69 \times 10^{-6} & 0 & -1.26 \times 10^{-2} \\ 0 & 0 & 0 \\ 0 & -6.47 \times 10^{-3} & 0 \\ 0 & 0 & 0 \\ 4.41 \times 10^{-3} & 0 & -1.23 \times 10^{-5} \\ 0 & 0 & 0 \\ 0 & -7.58 \times 10^{-3} & 0 \\ 0 & 0 & 0 \\ 4.90 \times 10^{-3} & 0 & -2.16 \times 10^{-6} \end{bmatrix} \begin{matrix} \}\text{mode 1} \\ \\ \}\text{mode 2} \\ \\ \}\text{mode 3} \\ \\ \\ \\ \\ \\ \\ \\ \\ \\ \\ \\ \\ \\ \}\text{mode 10} \end{matrix} \tag{A10}$$

In both equations (A9) and (A10), mode slope magnitudes less than 10^{-9} have been set to zero.

For collocated attitude sensors and torque actuators,

$$\mathbf{C}_F = [(\mathbf{I}_3, 0), \mathbf{V}_C]_{3\times n} \tag{A11}$$

with

$$\mathbf{V}_C = [\mathbf{U}\mathbf{V}_B]^T_{3\times 2nq} \tag{A12}$$

$$\mathbf{U}_{2nq\times 2nq} = \text{diag}\,(\mathbf{U}_1, \mathbf{U}_2, \ldots, \mathbf{U}_{nq}) \tag{A13}$$

$$\mathbf{U}_i = \begin{bmatrix} 0 & 1 \\ 1 & 0 \end{bmatrix}_{2\times 2} \tag{A14}$$

The matrix $\mathbf{V}_B$ in equation (A12) is chosen from equation (A9) or (A10), depending on actuator location. For collocated rate sensors,

$$\mathbf{C}_F = \left[(0, \mathbf{I}_3), \mathbf{V}_B^T\right]_{3\times n} \tag{A15}$$

A measure of the relative controllability of the rigid-body and elastic modes can be obtained through

examination of the reciprocal condition numbers of the polynomial matrix (ref. 12)

$$\mathbf{C}(s) = [(s\mathbf{I}_n - \mathbf{A}_F), \mathbf{B}_F] \qquad \text{(A16)}$$

over the set of eigenvalues of $\mathbf{A}_F$. Reciprocal condition numbers are defined as the ratio of smallest to largest singular values for $\mathbf{C}(s)$. Comparison of these numbers evaluated at $s = 0.0$ for the rigid-body mode and one of each of the eigenvalues of $\mathbf{A}_E^i$, $(i = 1, 2, \ldots, n_q)$ gives an indication of the relative ease or difficulty in affecting a particular mode through the control input. A similar approach applied to the polynomial matrix

$$O(s) = \begin{bmatrix} s\mathbf{I}_n - \mathbf{A}_F \\ \mathbf{C}_F \end{bmatrix} \qquad \text{(A17)}$$

can be used to measure relative observability properties. Table AII presents controllability and observability reciprocal condition numbers for collocated sensor and actuator locations 1 and 2 in figure 1.

Table AII indicates that of all the modes considered, the rigid-body modes are least controllable from both locations as could be expected from the large numerical magnitude of the inertia matrix $\mathbf{I}_s$. Mode 1 is easier to control from location 1 than 2. Modes greater than 4 are less likely to experience spillover (ref. 5) effects from location 1. The rigid-body modes are most observable. Mode 1 is least observable from location 2 and actually behaves numerically as an unobservable mode in Kalman filter computations. Generally, table AII shows that the first three modes have better controllability and observability properties from location 1.

The presence of invariant zeros (ref. 13) in the system models can be tested by seeking those values of s such that

$$\text{Rank} \begin{bmatrix} s\mathbf{I}_n - \mathbf{A}_F & \mathbf{B}_F \\ \mathbf{C}_F & 0 \end{bmatrix} < n + 3 \qquad (A18)$$

for given values of $1 \leq n_q \leq 10$. No zeros exist for $n_q = 0$ since in this case

$$\det \left[\mathbf{C}_F (s\mathbf{I}_6 - \mathbf{A}_F)^{-1} \mathbf{B}_F\right] = \det \left(\mathbf{I}_s^{-1}\right) \neq 0 \qquad \text{(A19)}$$

For $n_q > 0$, the finite invariant zeros can be obtained from data given in table AIII.

TABLE AII. RECIPROCAL CONDITION NUMBERS FOR COLLOCATED SENSOR/ACTUATOR LOCATIONS 1 AND 2

Reciprocal Condition number	Mode										
	Rigid body	1	2	3	4	5	6	7	8	9	10
$\mathbf{C}(s)$. (1)	2.4×10^{-7}	4.0×10^{-3}	1.7×10^{-3}	1.9×10^{-3}	2.5×10^{-6}	1.3×10^{-4}	5.6×10^{-5}	8.5×10^{-5}	1.6×10^{-4}	4.1×10^{-4}	2.8×10^{-4}
$\mathbf{C}(s)$. (2) . . .	2.4×10^{-7}	1.9×10^{-5}	1.5×10^{-4}	1.9×10^{-4}	5.9×10^{-5}	2.3×10^{-3}	2.2×10^{-3}	1.1×10^{-3}	6.4×10^{-4}	1.1×10^{-3}	5.5×10^{-4}
$O(s)$. (1)	0.56	1.6×10^{-3}	1.3×10^{-3}	1.5×10^{-3}	2.4×10^{-6}	1.3×10^{-4}	5.5×10^{-5}	8.4×10^{-5}	1.6×10^{-4}	4.0×10^{-4}	2.7×10^{-4}
$O(s)$. (2) . . .	0.56	7.9×10^{-6}	1.1×10^{-4}	1.6×10^{-4}	5.6×10^{-5}	2.3×10^{-3}	2.2×10^{-3}	1.1×10^{-3}	6.3×10^{-4}	1.0×10^{-3}	5.5×10^{-4}

TABLE AIII. DATA FOR INVARIANT ZEROS

n_q	Sensor/actuator location 1	Sensor/actuator location 2
1	$-0.9 \times 10^{-4} \pm j0.082$	$-0.75 \times 10^{-2} \pm j0.75$
2	$-0.37 \times 10^{-3} \pm j0.22$	$-0.013 \pm j1.3$
3	$-0.29 \times 10^{-3} \pm j0.22$	$-0.017 \pm j1.7$
4	$-0.032 \pm j3.2$	$-0.032 \pm j3.2$
5	$-0.045 \pm j4.5$	$-0.79 \times 10^{-4} \pm j0.19$
6	$-0.056 \pm j5.6$	$-0.11 \times 10^{-3} \pm j0.24$
7	$-0.057 \pm j5.7$	$-0.17 \times 10^{-3} \pm j0.32$
8	$-0.064 \pm j6.6$	$-0.065 \pm j6.5$
9	$-0.042 \pm j5.1$	$-0.065 \pm j6.5$
10	$-0.074 \pm j7.7$	$-0.082 \pm j8.3$

Given a particular n_q selection, the corresponding set of system zeros is the collection of entries from row 1 to row n_q in table III. For example, with $n_q = 3$ and location 1, the set of system zeros are

$$\left(-0.9 \times 10^{-4}\right) \pm j.082$$
$$\left(-0.37 \times 10^{-3}\right) \pm j0.22$$
$$\left(-0.29 \times 10^{-3}\right) \pm j0.22$$

For both locations, all zeros are (marginally) minimum phase. Many zeros lie close to the open-loop eigenvalues of $\mathbf{A}_E$ (eq. (A5)) giving, as in table AII, an indication that these modes will exhibit weak controllability/observability properties. Even though the zeros from location 2 for $n_q \leq 4$ have higher frequencies (therefore allowing a higher controller bandwidth before interfering with performance), location 1 is chosen for the LQG/LTR design studies due to better controllability/observability properties.

References

1. Doyle, John C.; and Stein, Gunter: Multivariable Feedback Design: Concepts for a Classical/Modern Synthesis. *IEEE Trans. Autom. Control,* vol. AC-26, no. 1, Feb. 1981, pp. 4–16.
2. Stein, Gunter: LQG-Based Multivariable Design: Frequency Domain Interpretation. *Multi-Variable Analysis and Design Techniques,* AGARD-LS-117, Sept. 1981, pp. 5–1—5–9.
3. Chan, Sherman M.; and Athans, Michael: Applications of Robustness Theory to Power System Models. *IEEE Trans. Autom. Control,* vol. AC-29, no. 1, Jan. 1984, pp. 2–8.
4. Kappos, Efthimios: *Robust Multivariable Control for the F100 Engine.* LIDS-TH-1328 (Grant NGL-22-009-124), Massachusetts Inst. of Technol., Sept. 1983. (Available as NASA CR-174304.)
5. Balas, Mark J.: Trends in Large Space Structure Control Theory: Fondest Hopes, Wildest Dreams. *IEEE Trans. Autom. Control,* vol. AC-27, no. 3, June 1982, pp. 522–535.
6. Kosut, Robert L.; Salzwedel, Horst; and Emami-Naeini, Abbas: Robust Control of Flexible Spacecraft. *J. Guid., Control, & Dyn.,* vol. 6, no. 2, Mar.–Apr. 1983, pp. 104–111.
7. Russell, R. A.; Campbell, T. G.; and Freeland, R. E.: *A Technology Development Program for Large Space Antennas.* NASA TM-81902, 1980. (Also available as Paper No. IAF-80-A-33.)
8. Sullivan, Marvin R.: *LSST (Hoop/Column) Maypole Antenna Development Program.* NASA CR-3558, 1982.
9. Joshi, Suresh M.: Control Systems Synthesis for a Large Flexible Space Antenna. *Acta Astronaut.,* vol. 10, no. 5–6, May–June 1983, pp. 365–380.
10. Cruz, Jose B., Jr.; Freudenberg, James S.; and Looze, Douglas P.: A Relationship Between Sensitivity and Stability of Multivariable Feedback Systems. *IEEE Trans. Autom. Control,* vol. AC-26, no. 1, Feb. 1981, pp. 66–74.
11. Armstrong, Ernest S.: *ORACLS—A Design System for Linear Multivariable Control.* Marcel Dekker, Inc., c.1980.
12. Kailath, Thomas: *Linear Systems.* Prentice-Hall, Inc., c.1980.
13. Emami-Naeini, A.; and Van Dooren, P.: Computation of Zeros of Linear Multivariable Systems. *Automatica,* vol. 18, no. 4, July 1982, pp. 415–430.

TABLE I. ANTENNA PARAMETERS

Weight, lb	10015.64
Inertia about axes through center of mass:	
I_{xx}, lb-ft-sec^2	4.222×10^6
I_{yy}, lb-ft-sec^2	4.239×10^6
I_{zz}, lb-ft-sec^2	3.233×10^6
Structural mode frequencies, rad/sec	0.75, 1.35, 1.7, 3.18, 4.53, 5.59, 5.78, 6.84, 7.4, 8.78

$I_{xy} = I_{yz} = I_{xz} = 0$

TABLE II. COMPENSATOR GAINS FOR ATTITUDE FEEDBACK CASE

Filter gain matrix $\mathbf{H}_{12\times3}$

4.47×10^{-1}	-9.32×10^{-9}	4.36×10^{-8}
-2.12×10^{-8}	4.47×10^{-1}	7.72×10^{-8}
-2.44×10^{-8}	1.48×10^{-7}	4.47×10^{-1}
1.00×10^{-1}	1.33×10^{-9}	7.60×10^{-9}
-1.33×10^{-9}	1.00×10^{-1}	-7.96×10^{-9}
-7.60×10^{-9}	7.97×10^{-9}	1.00×10^{-1}
-1.39×10^{-5}	1.42×10^{-5}	-3.60×10^{-9}
-7.92×10^{-6}	-1.41×10^{-5}	-1.94×10^{-9}
-5.12×10^{-6}	1.43×10^{-6}	-3.34×10^{-11}
-2.59×10^{-6}	-5.16×10^{-6}	1.19×10^{-10}
-3.29×10^{-6}	5.69×10^{-7}	8.92×10^{-11}
-1.65×10^{-6}	-3.31×10^{-6}	1.26×10^{-10}

Control gain matrix $\mathbf{G}_{3\times12}$

10^5	-2.73×10^{-7}	-7.61×10^2
-9.85×10^{-7}	10^5	-6.2×10^{-7}
7.61×10^2	4.5×10^{-7}	10^5
7.52×10^5	2.26×10^{-5}	-8.6×10^3
1.23×10^{-5}	7.61×10^5	-7.44×10^{-6}
-3.32×10^2	3.64×10^{-6}	3.35×10^5
-2.63	-1.91×10^{-10}	-4.12×10^2
9.55	2.49×10^{-10}	-3.83×10^2
2.57×10^{-8}	-9.31×10^1	3.67×10^{-9}
2.88×10^{-8}	-1.95×10^2	1.00×10^{-9}
1.14×10^2	-6.81×10^{-9}	3.60×10^1
1.98×10^2	1.413×10^{-9}	2.32×10^1

TABLE III. CLOSED-LOOP EIGENVALUES FOR ATTITUDE FEEDBACK

Real part	Imaginary part
-8.54×10^{-3}	8.05×10^{-2}
-8.54×10^{-3}	-8.05×10^{-2}
-7.56×10^{-2}	1.25×10^{-1}
-7.56×10^{-2}	-1.25×10^{-1}
-7.60×10^{-2}	1.25×10^{-1}
-7.60×10^{-2}	-1.25×10^{-1}
-2.24×10^{-1}	2.24×10^{-1}
-2.24×10^{-1}	-2.24×10^{-1}
-2.33×10^{-1}	2.15×10^{-1}
-2.33×10^{-1}	-2.15×10^{-1}
-2.38×10^{-1}	2.11×10^{-1}
-2.38×10^{-1}	-2.11×10^{-1}
-7.47×10^{-3}	7.47×10^{-1}
-7.47×10^{-3}	-7.47×10^{-1}
-1.35×10^{-2}	1.35×10^{0}
-1.35×10^{-2}	-1.35×10^{0}
-3.08×10^{-1}	1.37×10^{0}
-3.08×10^{-1}	-1.37×10^{0}
-1.02×10^{0}	1.27×10^{0}
-1.02×10^{0}	-1.27×10^{0}
-1.70×10^{-2}	1.70×10^{0}
-1.70×10^{-2}	-1.70×10^{0}
-4.03×10^{-1}	1.74×10^{0}
-4.03×10^{-1}	-1.74×10^{0}
-3.18×10^{-2}	3.18×10^{0}
-3.18×10^{-2}	-3.18×10^{0}
-4.42×10^{-2}	4.53×10^{0}
-4.42×10^{-2}	-4.53×10^{0}
-5.58×10^{-2}	5.59×10^{0}
-5.58×10^{-2}	-5.59×10^{0}
-5.73×10^{-2}	5.78×10^{0}
-5.73×10^{-2}	-5.78×10^{0}
-6.69×10^{-2}	6.84×10^{0}
-6.69×10^{-2}	-6.84×10^{0}
-6.39×10^{-2}	7.40×10^{0}
-6.39×10^{-2}	-7.40×10^{0}
-8.33×10^{-2}	8.78×10^{0}
-8.33×10^{-2}	-8.78×10^{0}

TABLE IV. COMPENSATOR GAINS FOR ATTITUDE AND RATE FEEDBACK CASE

Filter gain matrix $\mathbf{H}_{12\times6}$

4.17×10^{-1}	-2.87×10^{-12}	1.51×10^{-12}	9.09×10^{-2}	1.99×10^{-12}	-8.20×10^{-13}
1.31×10^{-11}	4.17×10^{-1}	6.79×10^{-12}	3.92×10^{-12}	9.09×10^{-2}	9.36×10^{-13}
1.67×10^{-11}	-9.32×10^{-12}	4.17×10^{-1}	1.78×10^{-12}	2.05×10^{-12}	9.09×10^{-2}
9.09×10^{-2}	-2.16×10^{-13}	1.84×10^{-13}	4.17×10^{-2}	7.07×10^{-13}	-2.84×10^{-13}
3.11×10^{-12}	9.09×10^{-2}	2.06×10^{-12}	1.25×10^{-12}	4.17×10^{-2}	4.52×10^{-13}
2.32×10^{-12}	-7.95×10^{-13}	9.09×10^{-2}	2.63×10^{-14}	6.09×10^{-13}	4.17×10^{-2}
2.51×10^{-11}	2.47×10^{-11}	-3.32×10^{-9}	-7.10×10^{-11}	6.89×10^{-11}	5.39×10^{-10}
3.85×10^{-11}	-2.51×10^{-11}	-1.83×10^{-9}	3.37×10^{-11}	3.12×10^{-12}	-2.91×10^{-9}
-1.67×10^{-11}	-7.10×10^{-10}	-3.15×10^{-11}	-1.36×10^{-10}	6.88×10^{-11}	-8.74×10^{-11}
8.07×10^{-11}	-3.32×10^{-10}	1.12×10^{-10}	7.91×10^{-12}	-1.58×10^{-9}	-6.84×10^{-12}
6.40×10^{-10}	-1.85×10^{-11}	8.03×10^{-11}	-5.92×10^{-11}	-7.70×10^{-11}	-4.46×10^{-11}
2.83×10^{-10}	9.03×10^{-11}	1.19×10^{-10}	2.18×10^{-9}	-1.64×10^{-11}	3.16×10^{-10}

Control gain matrix $\mathbf{G}_{12\times3}^{T}$

10.00×10^{3}	2.40×10^{-8}	-1.01×10^{1}
5.05×10^{-9}	1.00×10^{4}	-1.16×10^{-8}
1.01×10^{1}	1.12×10^{-8}	10.00×10^{3}
2.84×10^{5}	1.39×10^{-6}	-4.57×10^{2}
1.35×10^{-6}	2.85×10^{5}	7.11×10^{-8}
4.00×10^{1}	3.82×10^{-7}	2.11×10^{5}
-7.10×10^{0}	-7.49×10^{-1}	-1.52×10^{0}
9.64×10^{-1}	2.40×10^{-11}	-7.87×10^{1}
1.22×10^{-9}	-2.45×10^{0}	2.53×10^{-11}
4.38×10^{-9}	-2.81×10^{1}	-2.98×10^{-10}
3.13×10^{0}	7.35×10^{-10}	7.08×10^{-1}
3.50×10^{1}	-2.53×10^{-11}	5.19×10^{0}

TABLE V. CLOSED-LOOP EIGENVALUES FOR ATTITUDE AND RATE FEEDBACK

-3.35×10^{-2}	3.52×10^{-2}
-3.35×10^{-2}	-3.52×10^{-2}
-3.36×10^{-2}	3.52×10^{-2}
-3.36×10^{-2}	-3.52×10^{-2}
-2.87×10^{-2}	4.47×10^{-2}
-2.87×10^{-2}	-4.47×10^{-2}
-2.32×10^{-1}	2.14×10^{-1}
-2.32×10^{-1}	-2.14×10^{-1}
-2.30×10^{-1}	2.17×10^{-1}
-2.30×10^{-1}	-2.17×10^{-1}
-2.29×10^{-1}	2.18×10^{-1}
-2.29×10^{-1}	-2.18×10^{-1}
-7.47×10^{-3}	7.47×10^{-1}
-7.47×10^{-3}	-7.47×10^{-1}
-2.09×10^{-1}	7.53×10^{-1}
-2.09×10^{-1}	-7.53×10^{-1}
-1.35×10^{-2}	1.35×10^{0}
-1.35×10^{-2}	-1.35×10^{0}
-5.42×10^{-2}	1.35×10^{0}
-5.42×10^{-2}	-1.35×10^{0}
-1.70×10^{-2}	1.70×10^{0}
-1.70×10^{-2}	-1.70×10^{0}
-8.33×10^{-2}	1.70×10^{0}
-8.33×10^{-2}	-1.70×10^{0}
-3.18×10^{-2}	3.18×10^{0}
-3.18×10^{-2}	-3.18×10^{0}
-4.51×10^{-2}	4.53×10^{0}
-4.51×10^{-2}	-4.53×10^{0}
-5.59×10^{-2}	5.59×10^{0}
-5.59×10^{-2}	-5.59×10^{0}
-5.77×10^{-2}	5.78×10^{0}
-5.77×10^{-2}	-5.78×10^{0}
-6.81×10^{-2}	6.84×10^{0}
-6.81×10^{-2}	-6.84×10^{0}
-7.19×10^{-2}	7.41×10^{0}
-7.19×10^{-2}	-7.41×10^{0}
-8.78×10^{-2}	8.78×10^{0}
-8.78×10^{-2}	-8.78×10^{0}

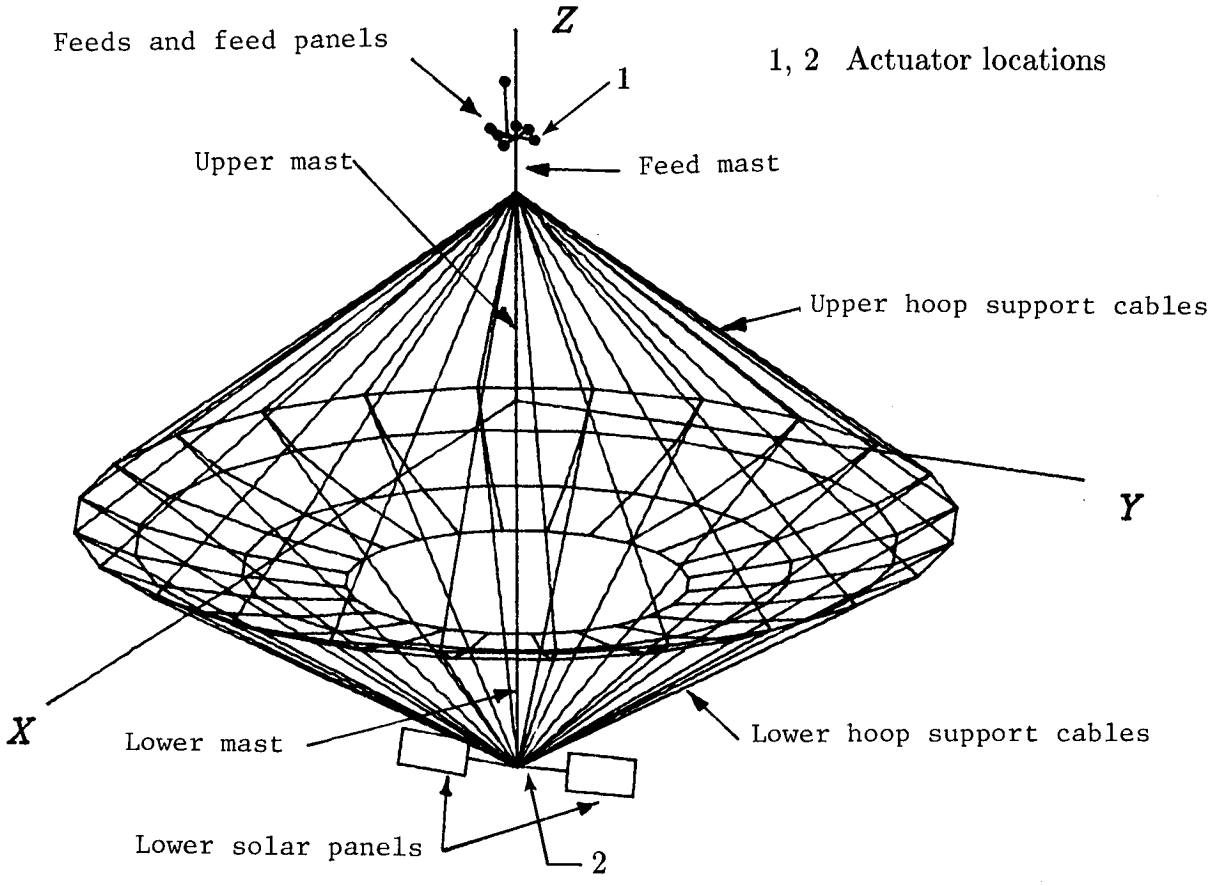

Figure 1. Hoop/column antenna concept.

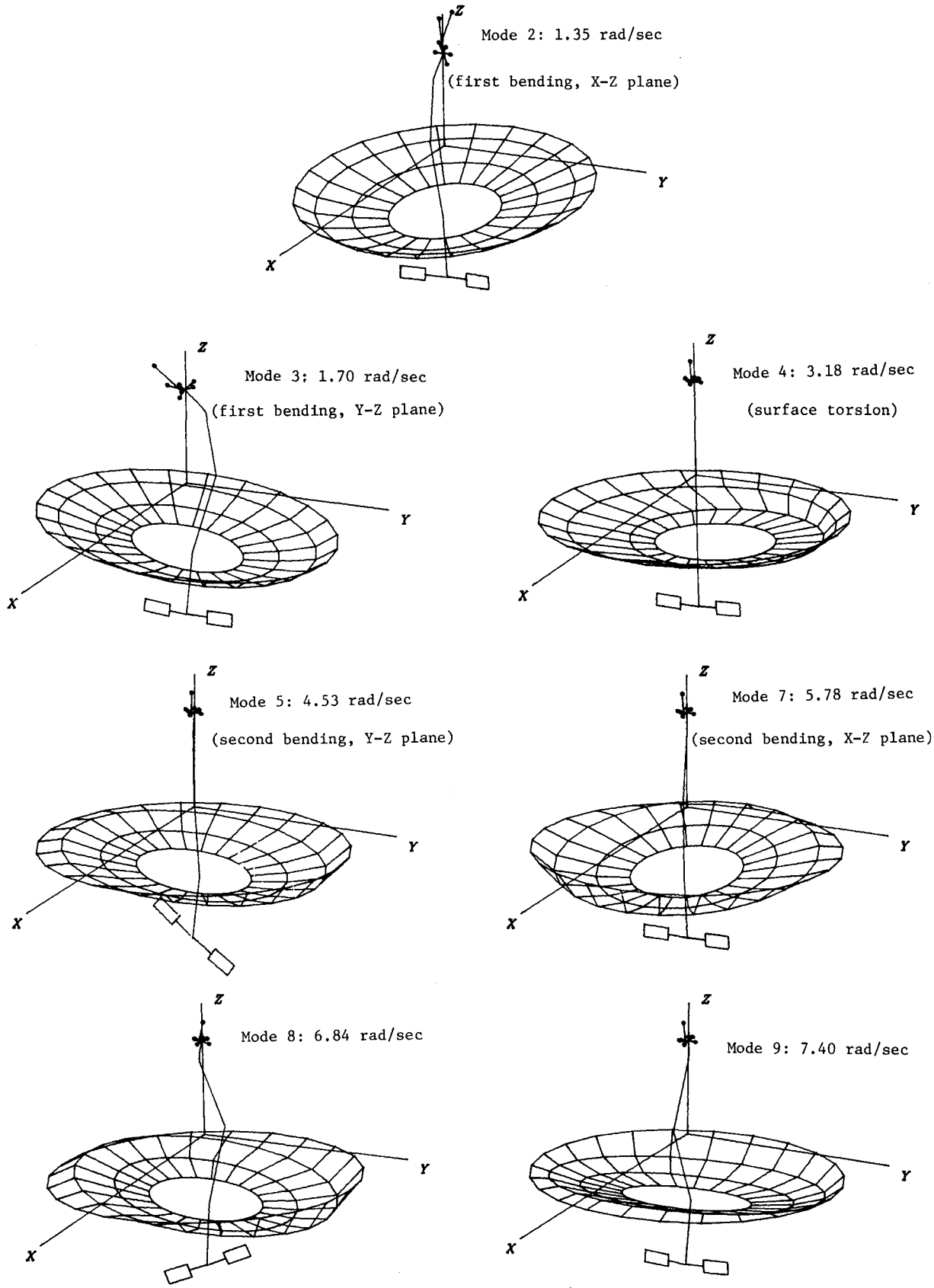

Figure 2. Plots of typical antenna mode shapes.

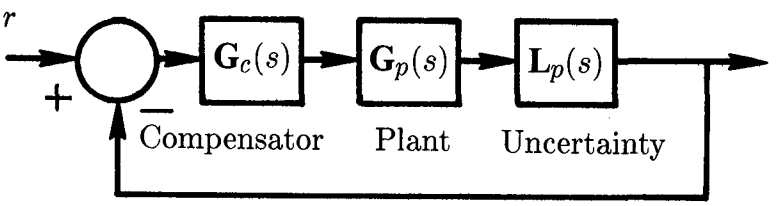

(a) Multiplicative uncertainty.

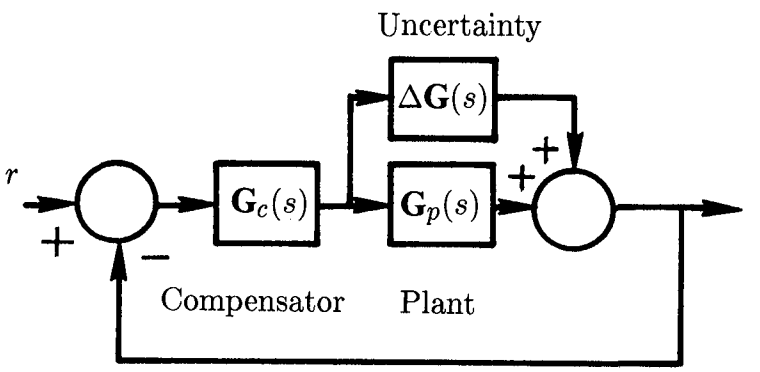

(b) Additive uncertainty.

Figure 3. Definition of uncertainty.

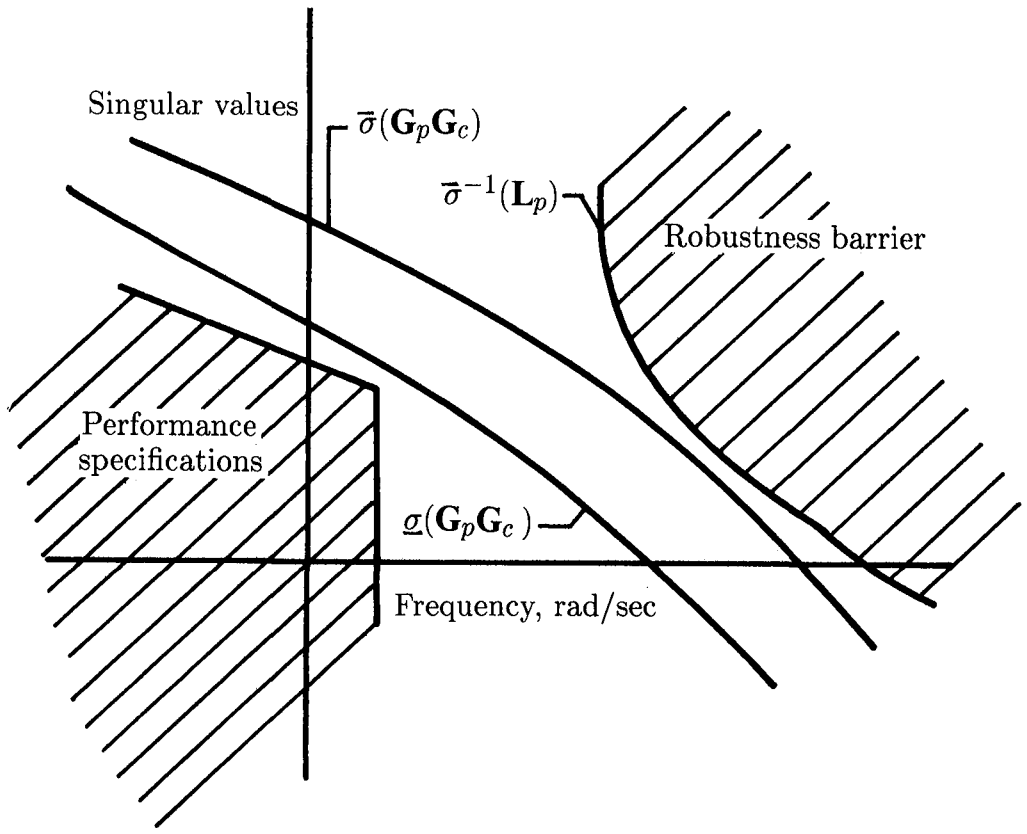

(a) Performance and robustness barriers for multiplicative uncertainty.

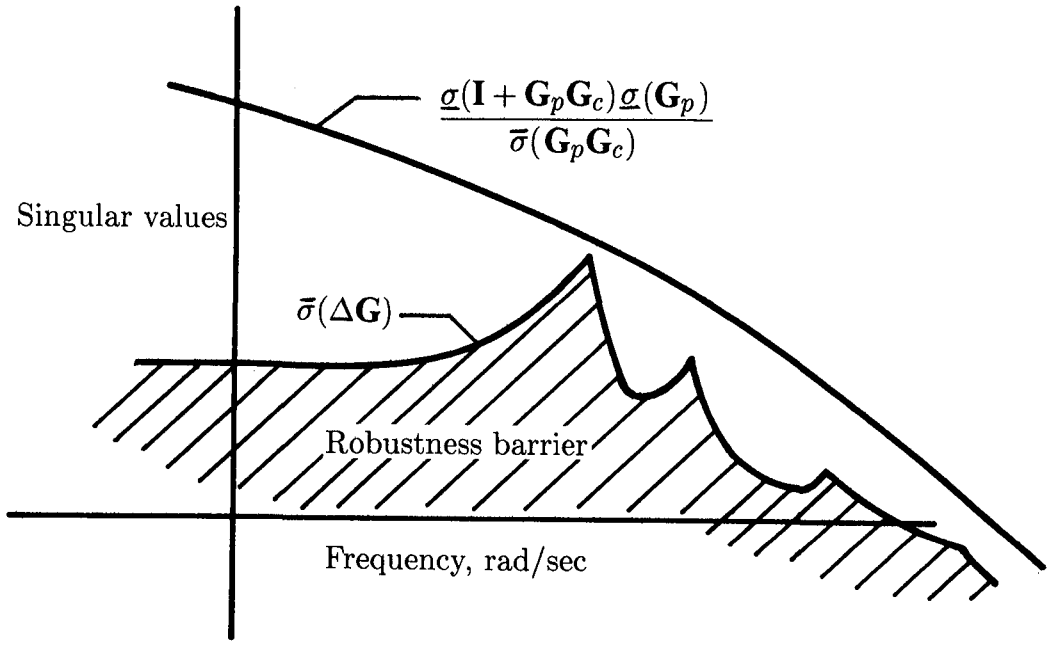

(b) Robustness barrier for additive uncertainty.

Figure 4. Performance and robustness barriers.

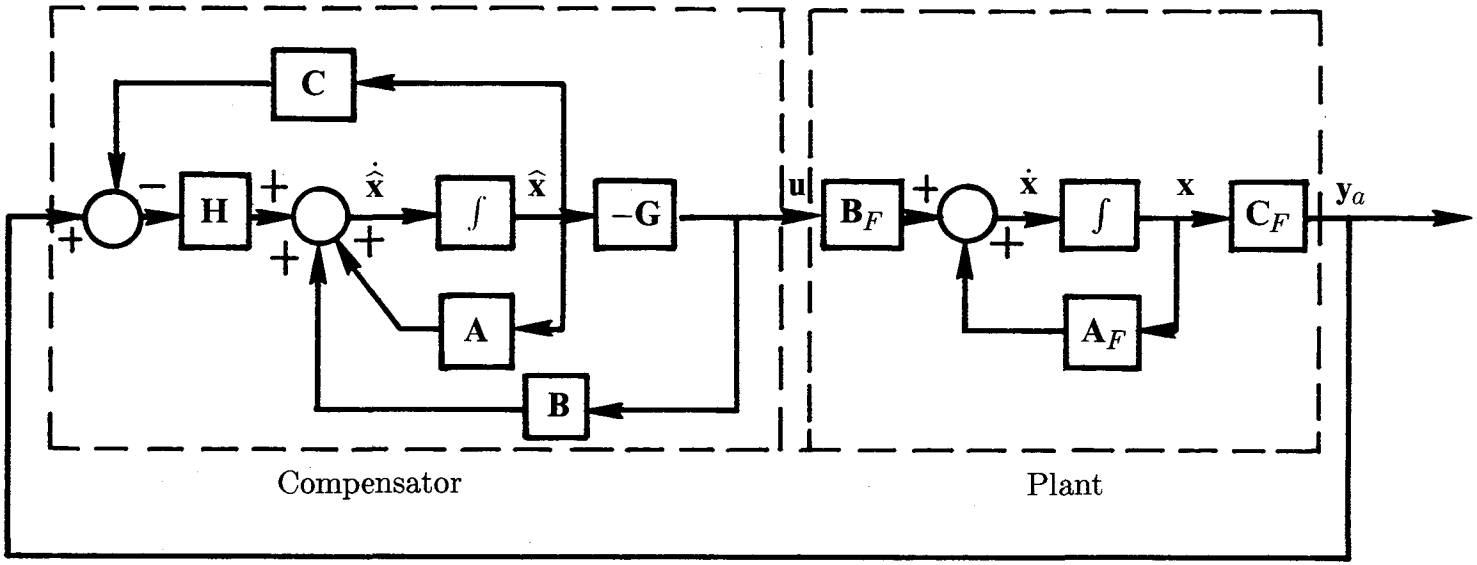

Figure 5. Block diagram of compensator/plant loop.

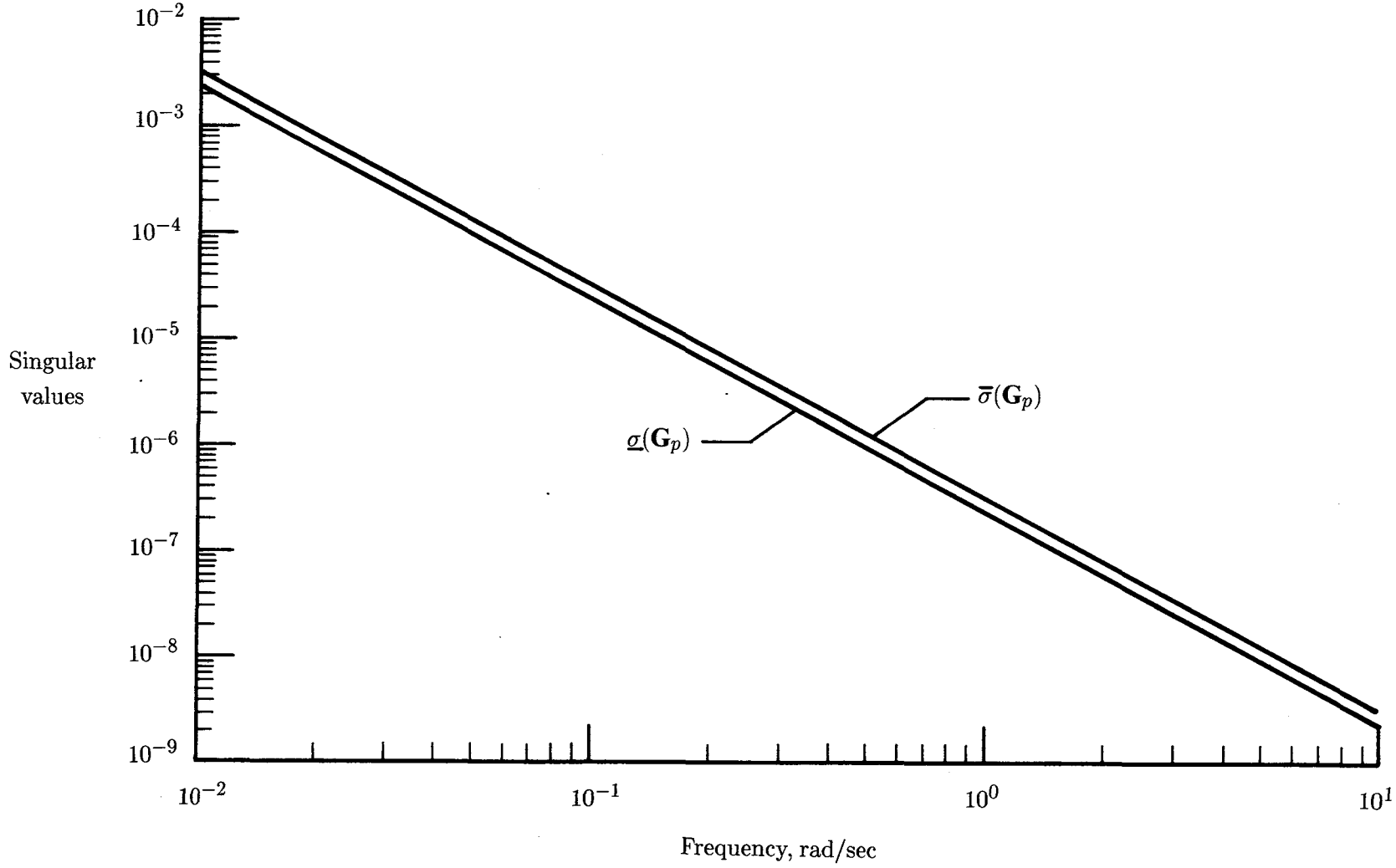

Figure 6. Singular values of $\mathbf{G}_p$ for rigid-body design model (attitude feedback).

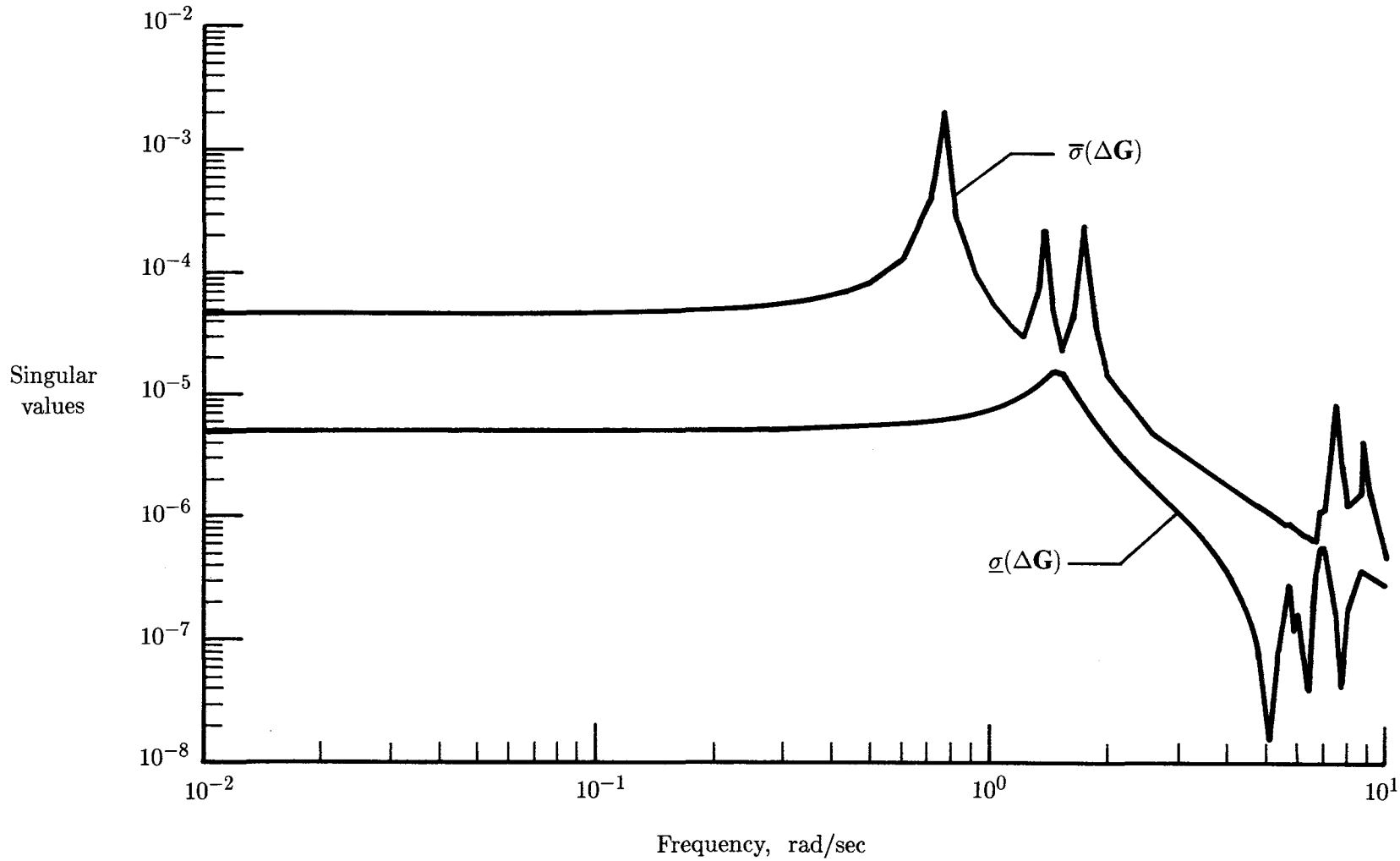

Figure 7. Singular values of $\Delta \mathbf{G}$ for rigid-body design model (attitude feedback).

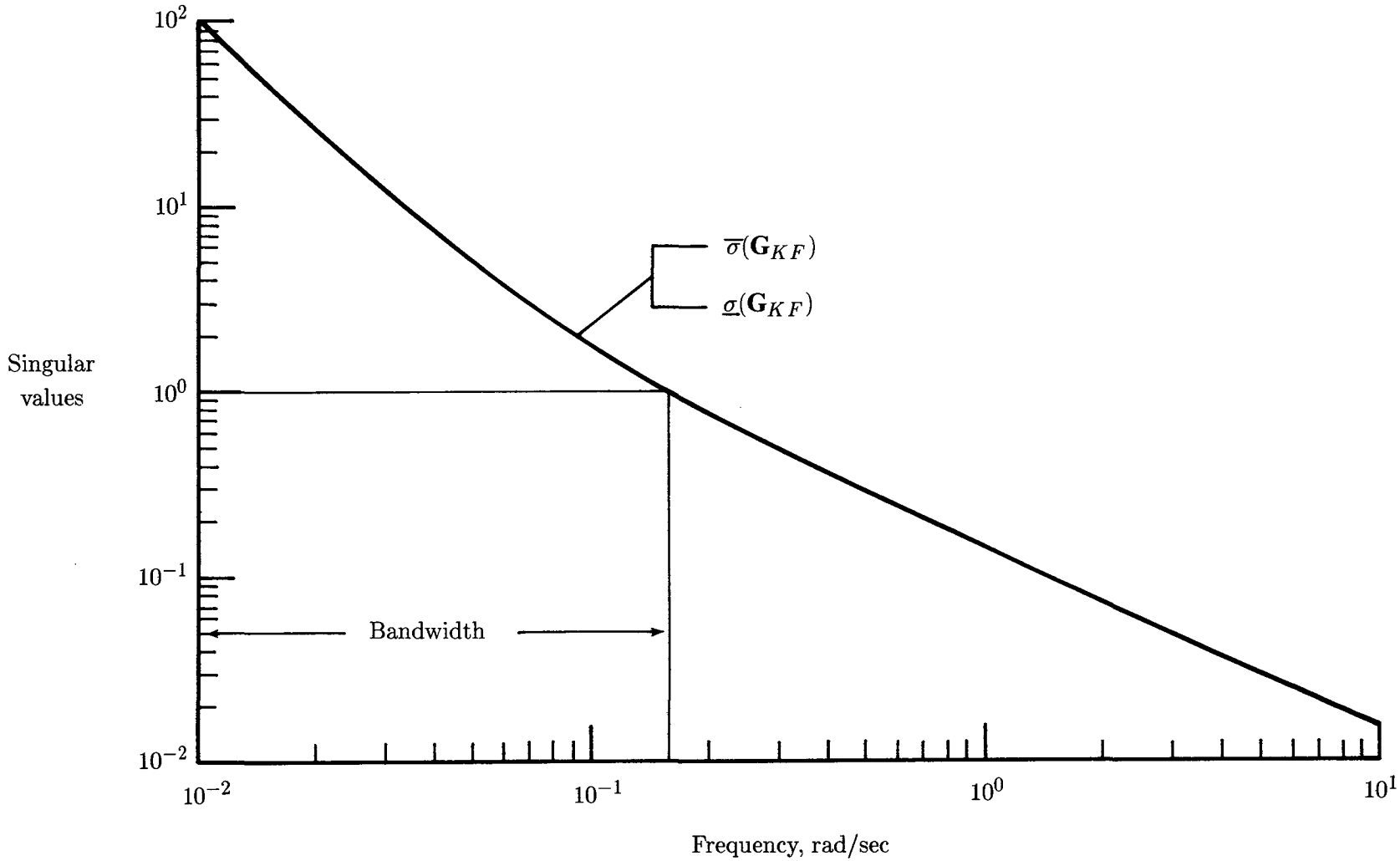

Figure 8. Singular values of $\mathbf{G}_{KF}$ for rigid-body design model (attitude feedback).

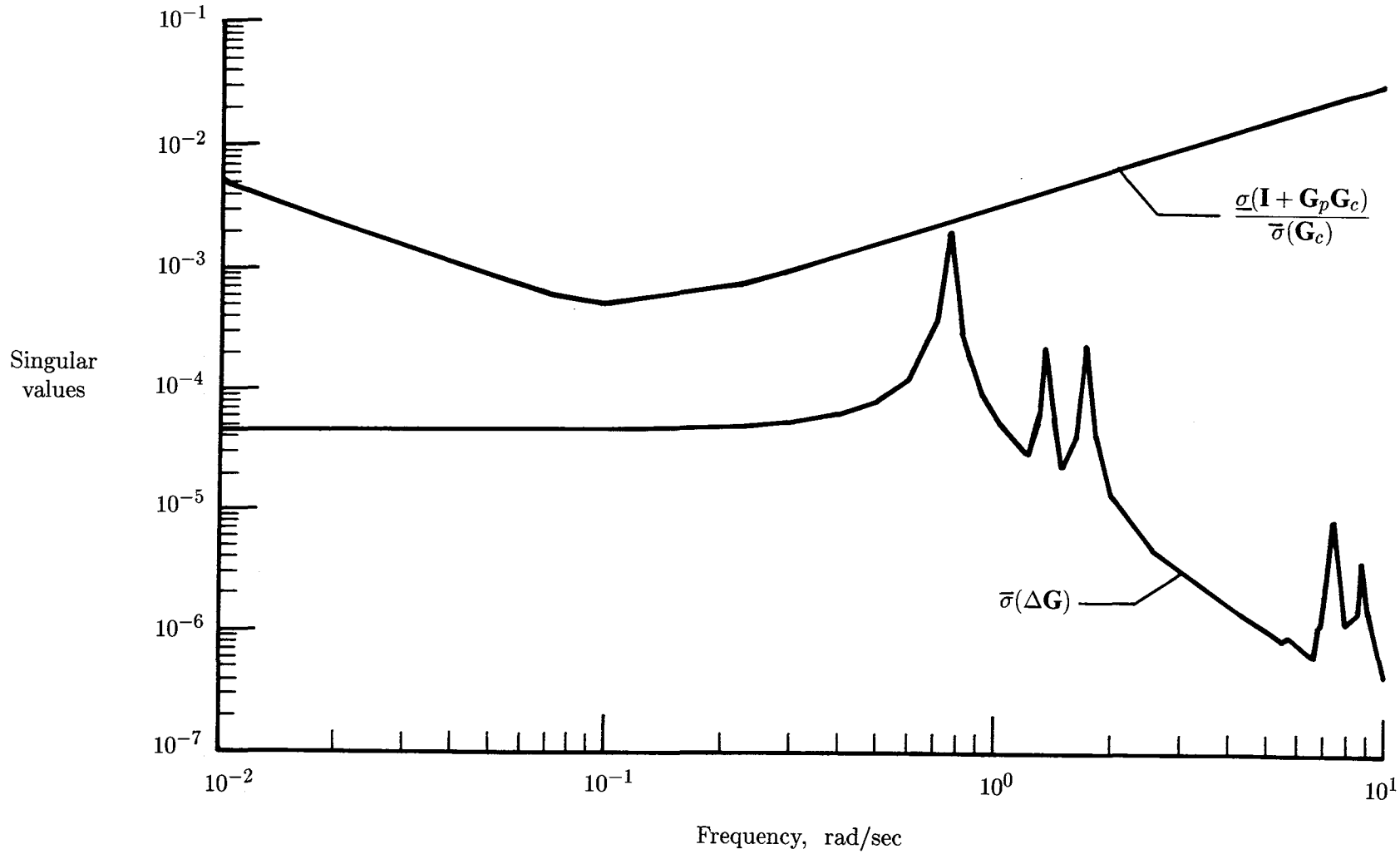

Figure 9. Stability robustness test (eq. (11)) for rigid-body design model (attitude feedback).

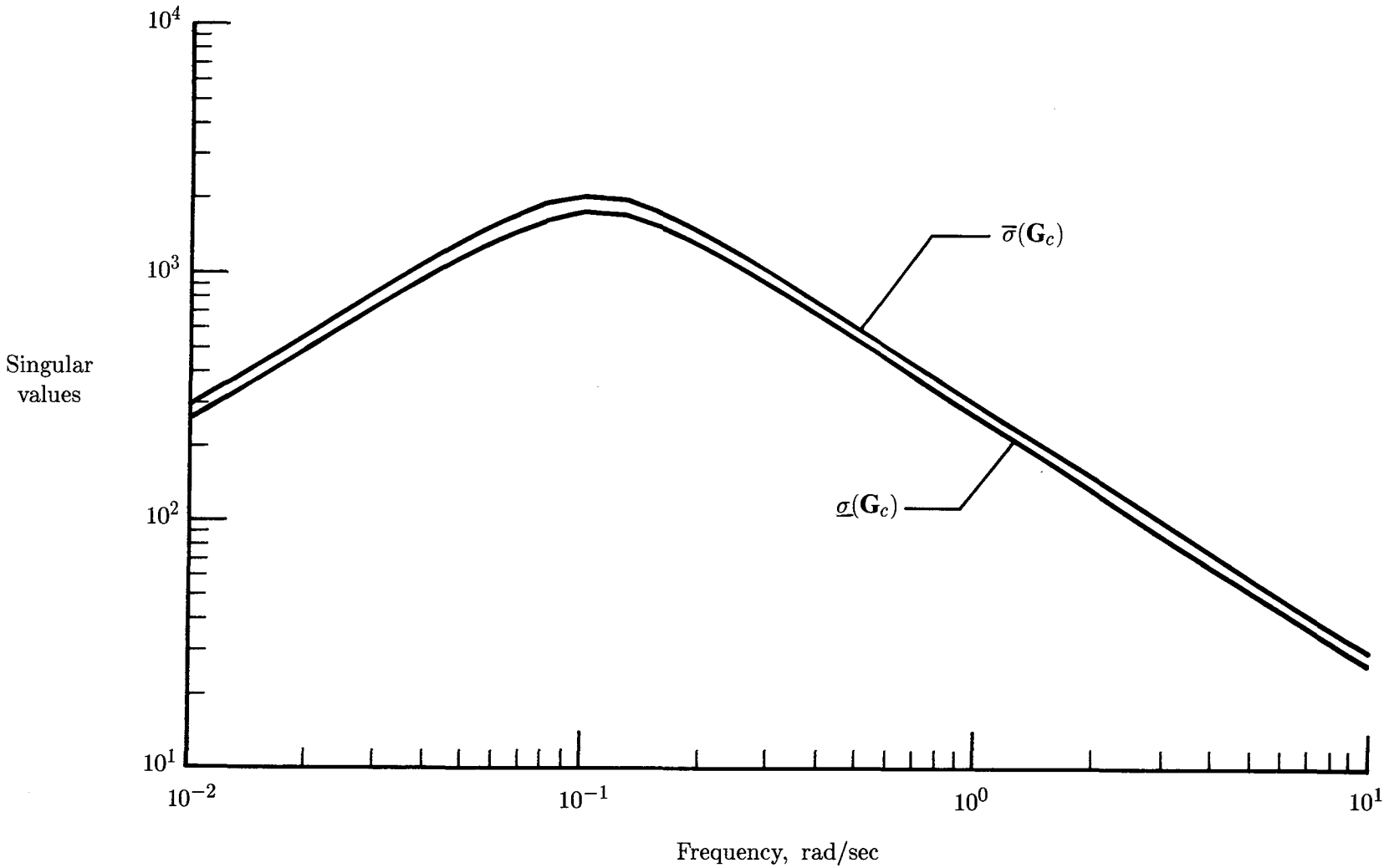

Figure 10. Singular values of compensator $\mathbf{G}_c$ for rigid-body design model (attitude feedback).

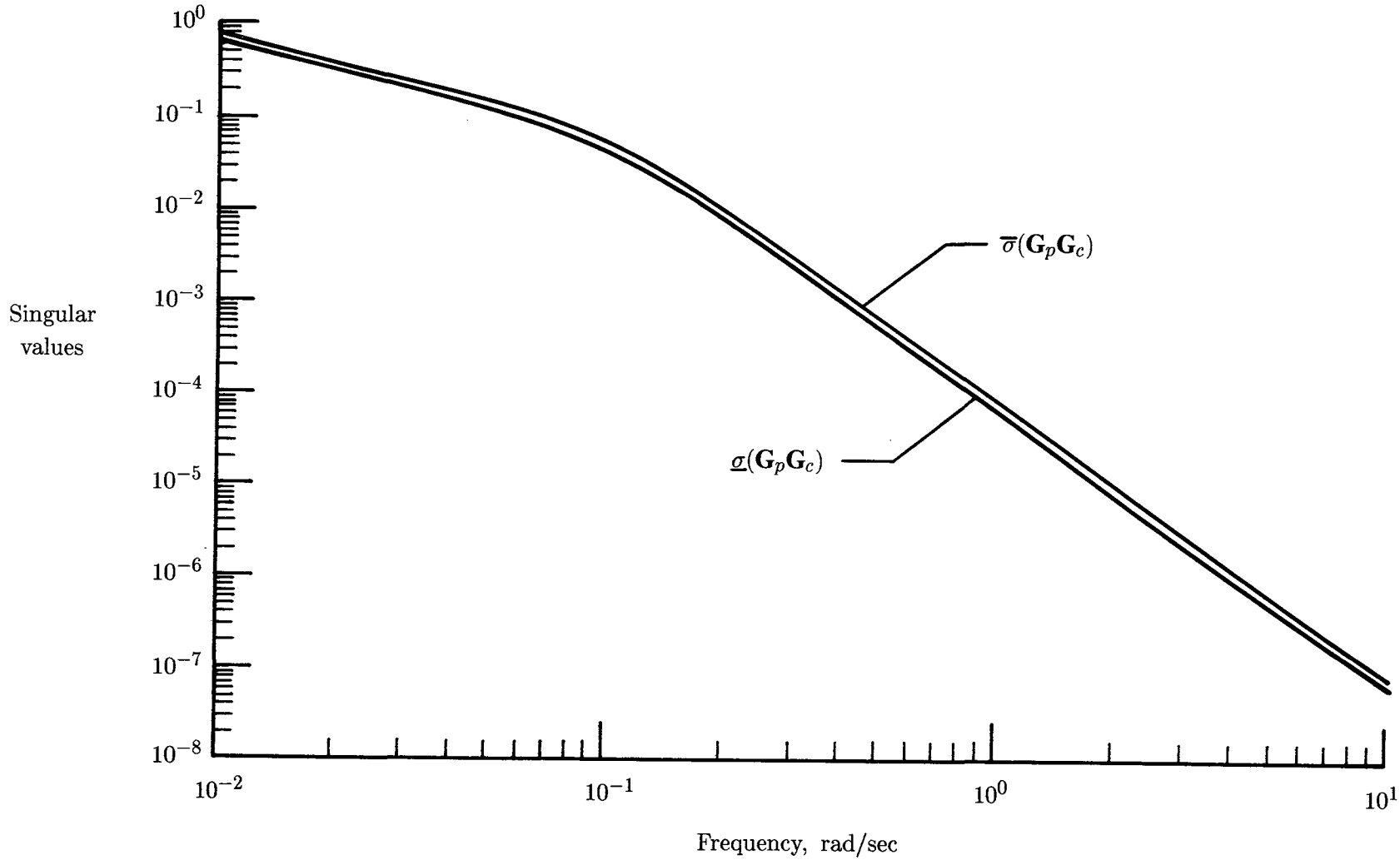

Figure 11. Singular values of loop transfer matrix $\mathbf{G}_p\mathbf{G}_c$ for rigid-body design model (attitude feedback).

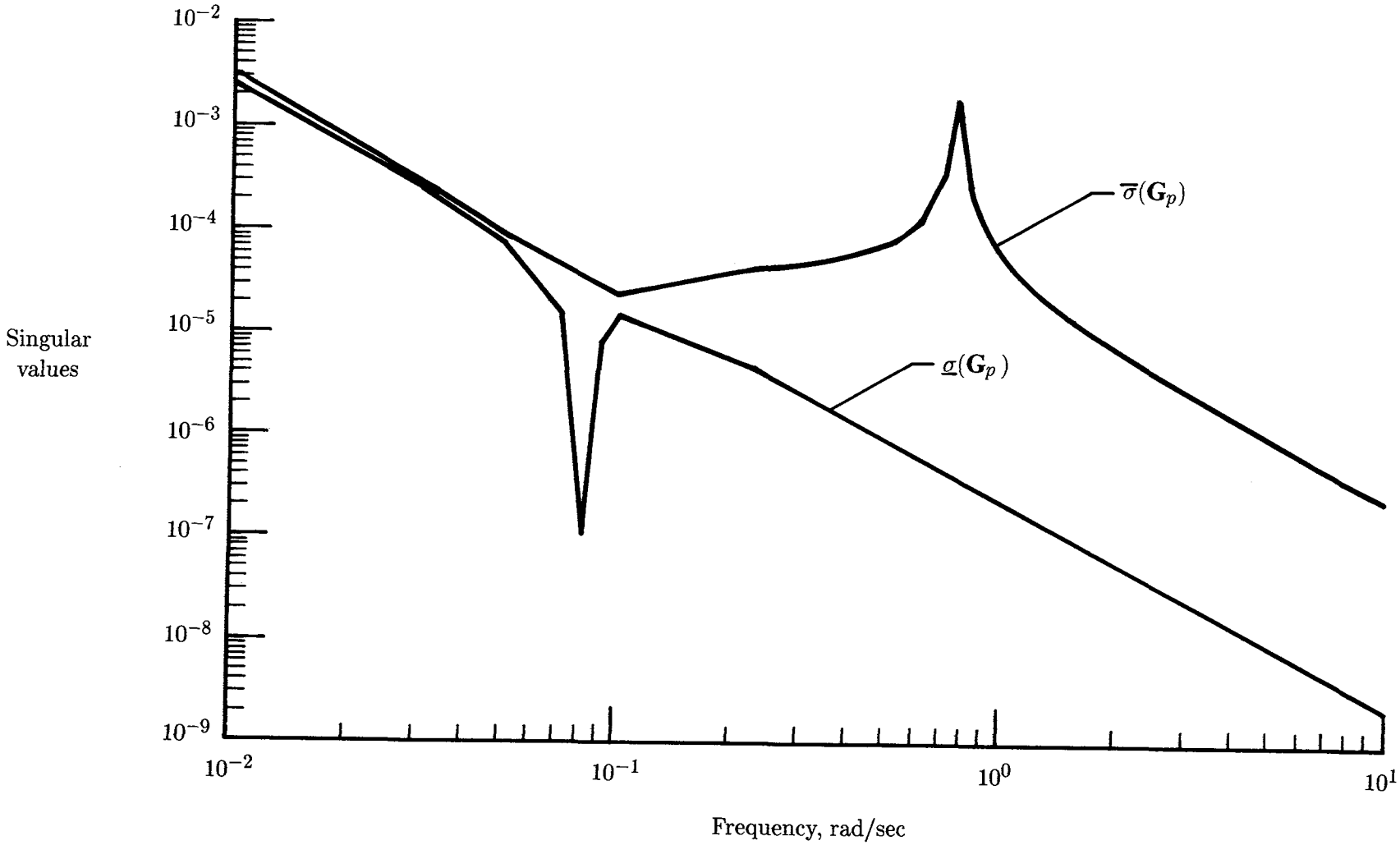

Figure 12. Singular values of $\mathbf{G}_p$ for one-mode design model (attitude feedback).

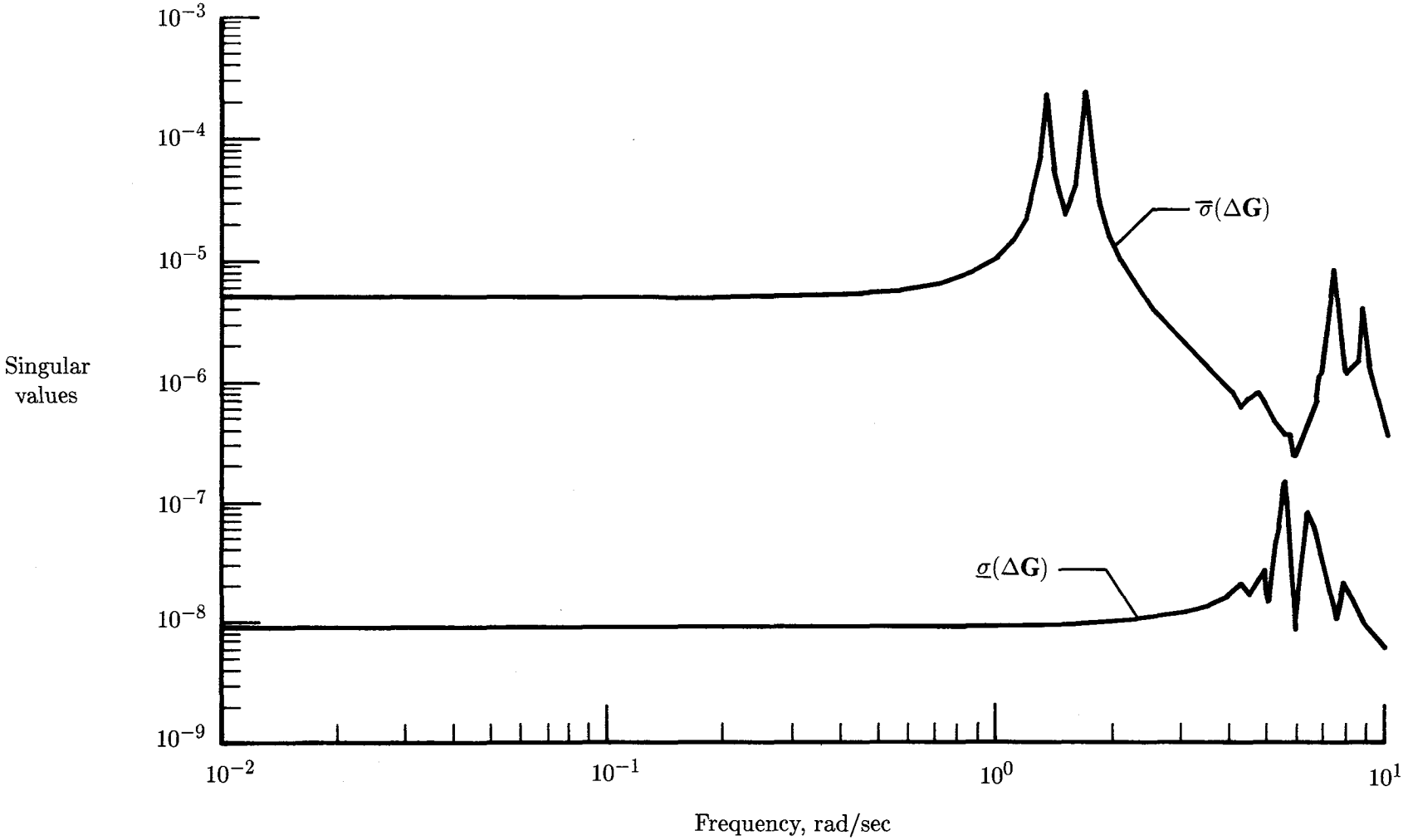

Figure 13. Singular values of $\Delta \mathbf{G}$ for one-mode design model (attitude feedback).

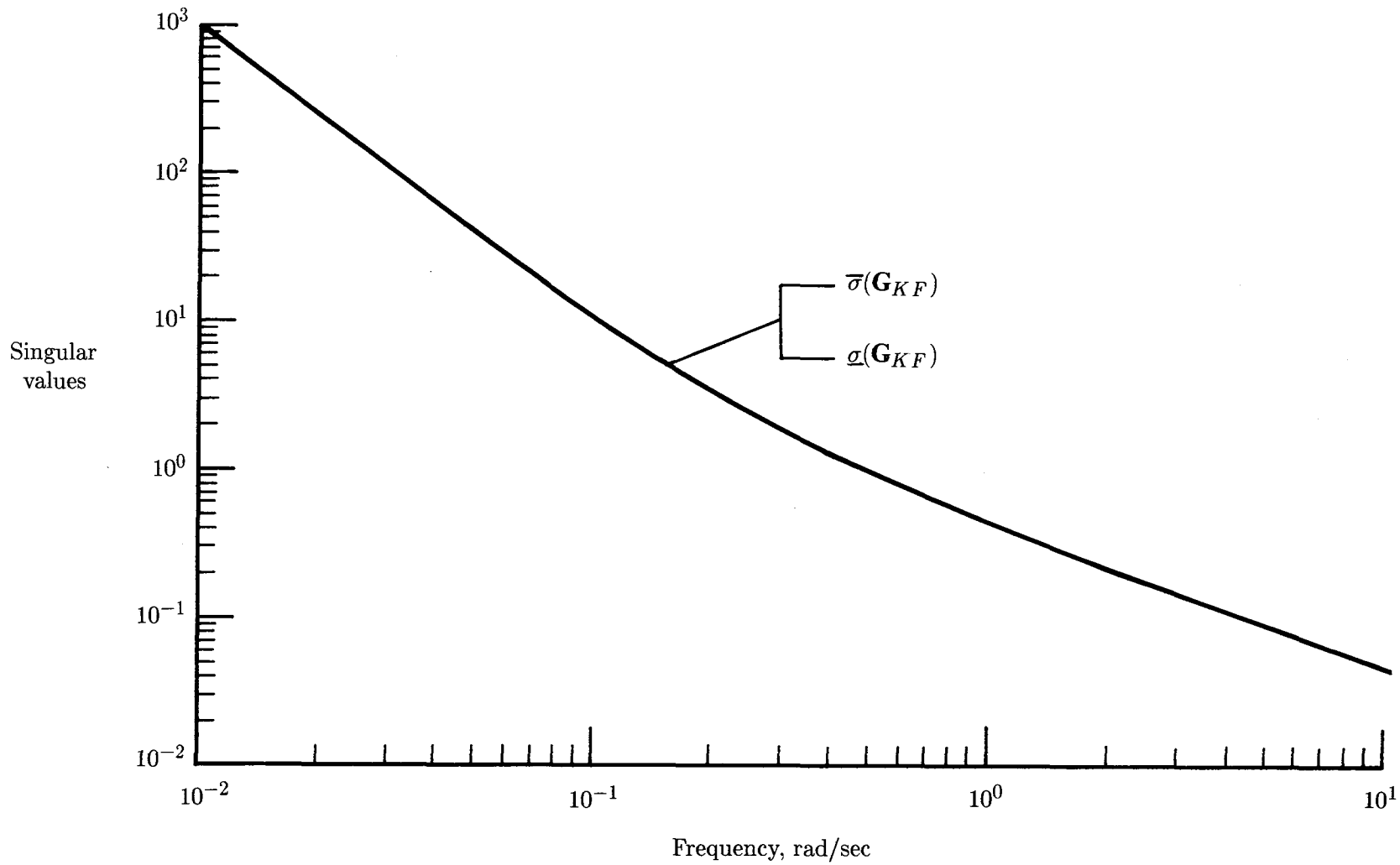

Figure 14. Singular values of $\mathbf{G}_{KF}$ for one-mode design model (attitude feedback).

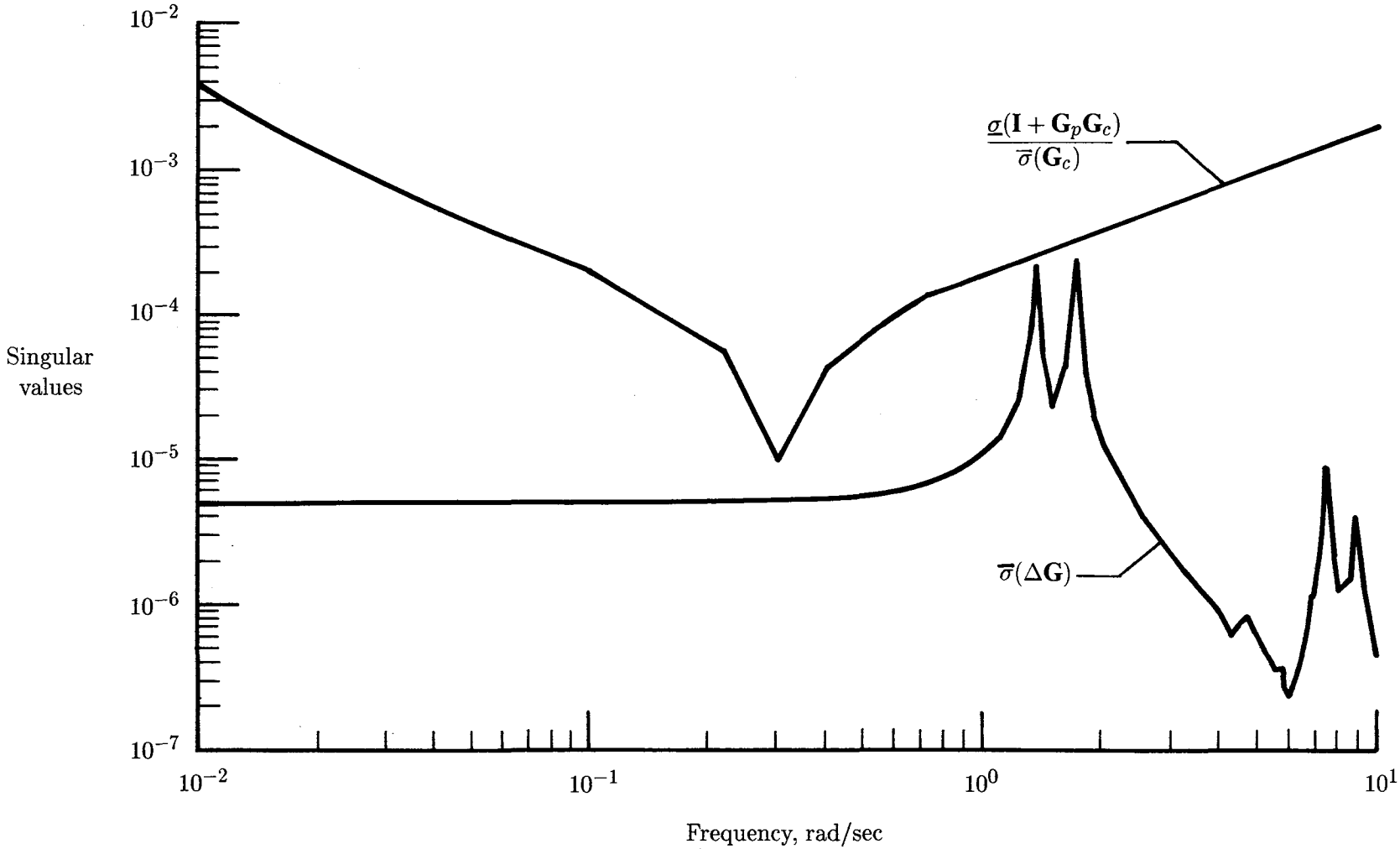

Figure 15. Stability robustness test for one-mode design model (attitude feedback).

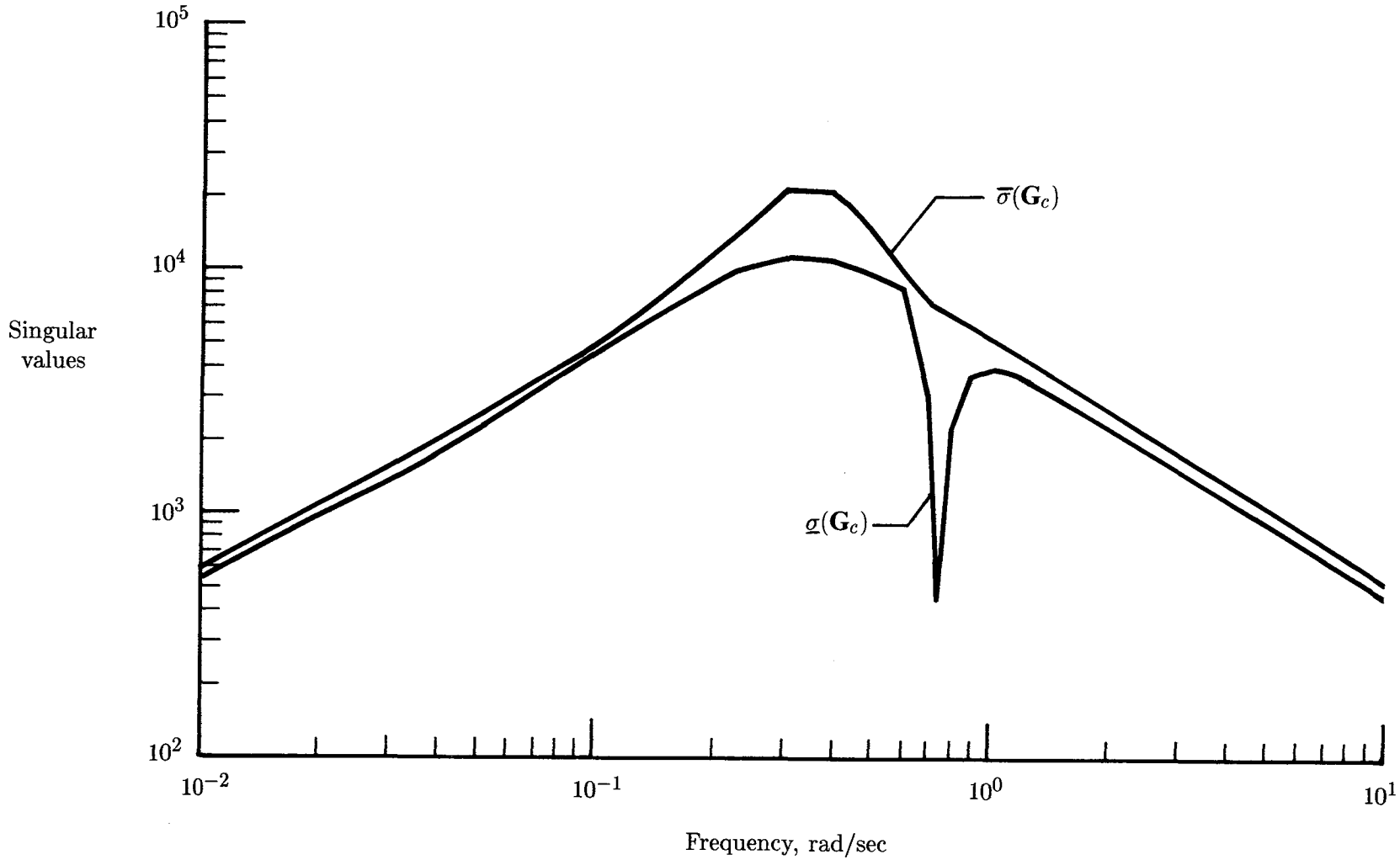

Figure 16. Singular values of compensator $\mathbf{G}_c$ for one-mode design model (attitude feedback).

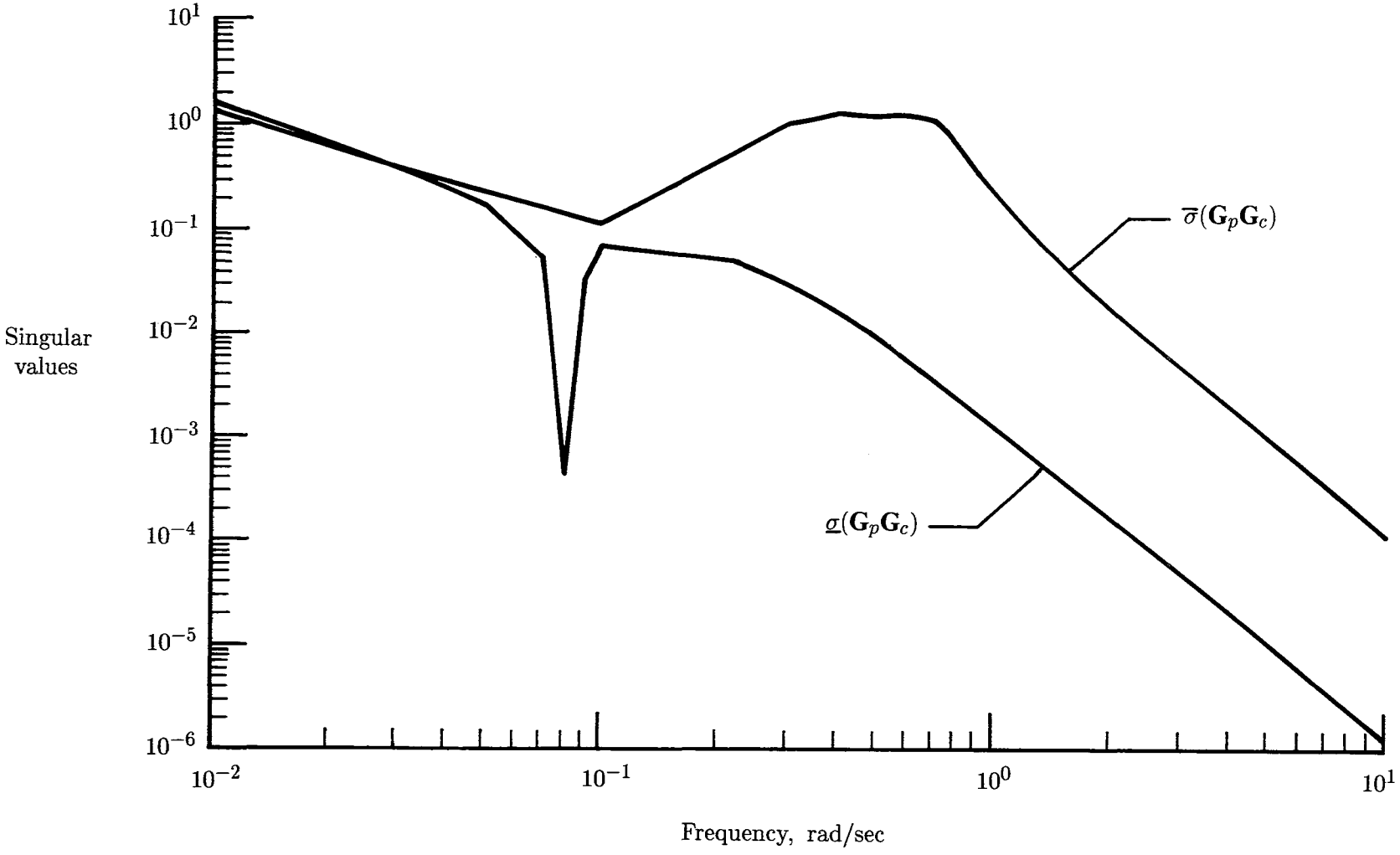

Figure 17. Singular values of $\mathbf{G}_p\mathbf{G}_c$ for one-mode design model (attitude feedback).

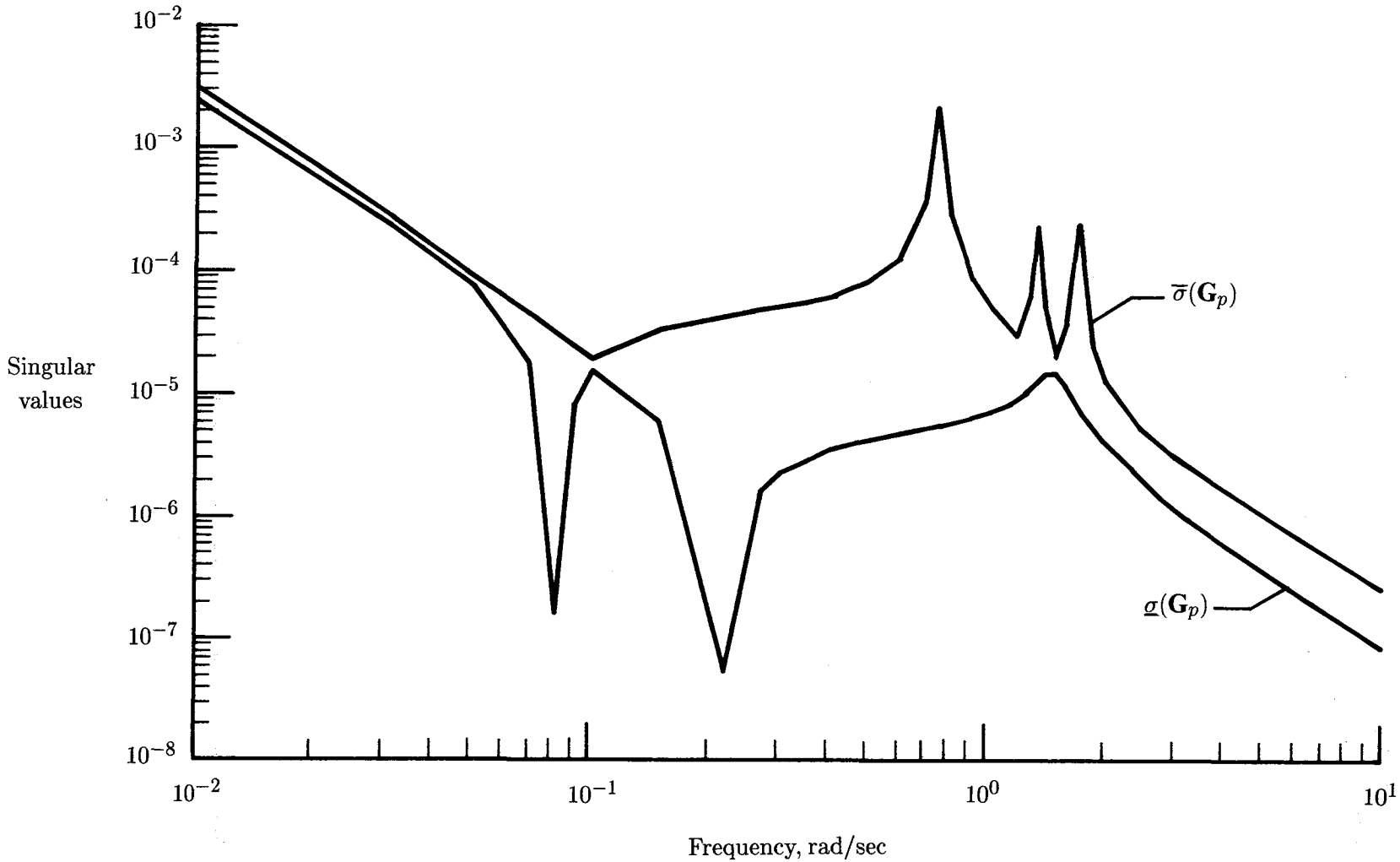

Figure 18. Singular values of $\mathbf{G}_p$ for three-mode model (attitude feedback).

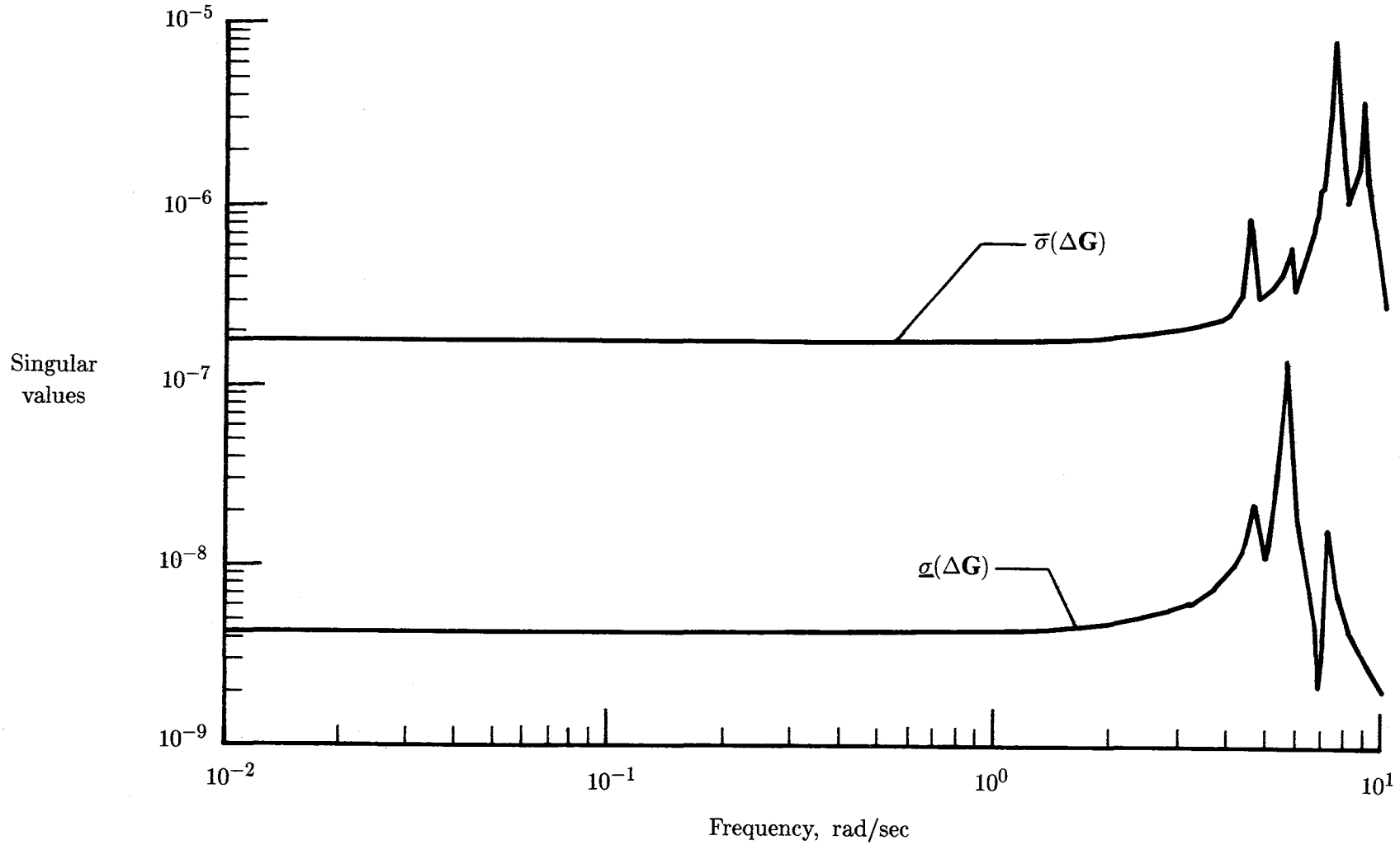

Figure 19. Singular values of $\Delta \mathbf{G}$ for three-mode design model (attitude feedback).

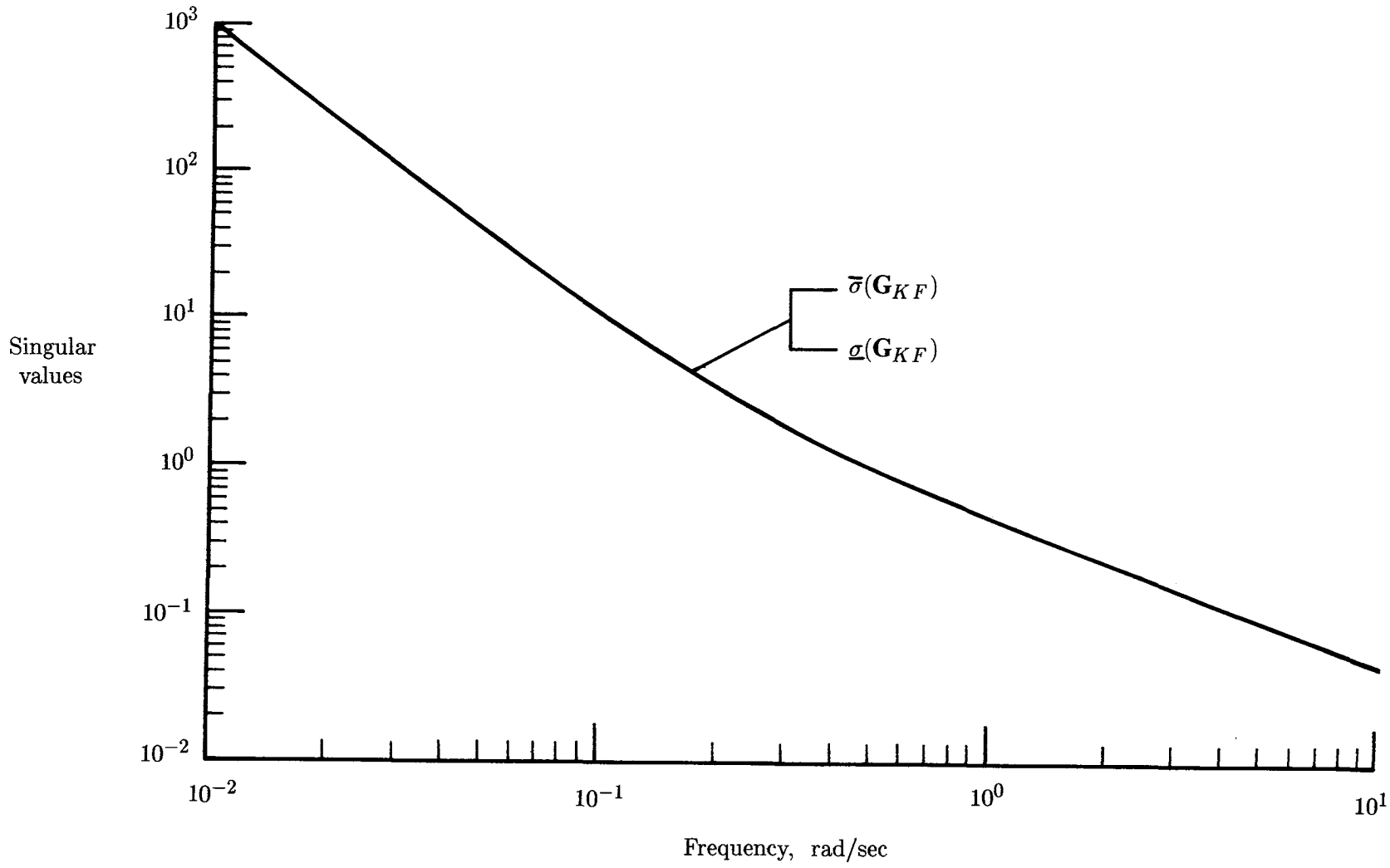

Figure 20. Singular values of $\mathbf{G}_{KF}$ for three-mode design model (attitude feedback).

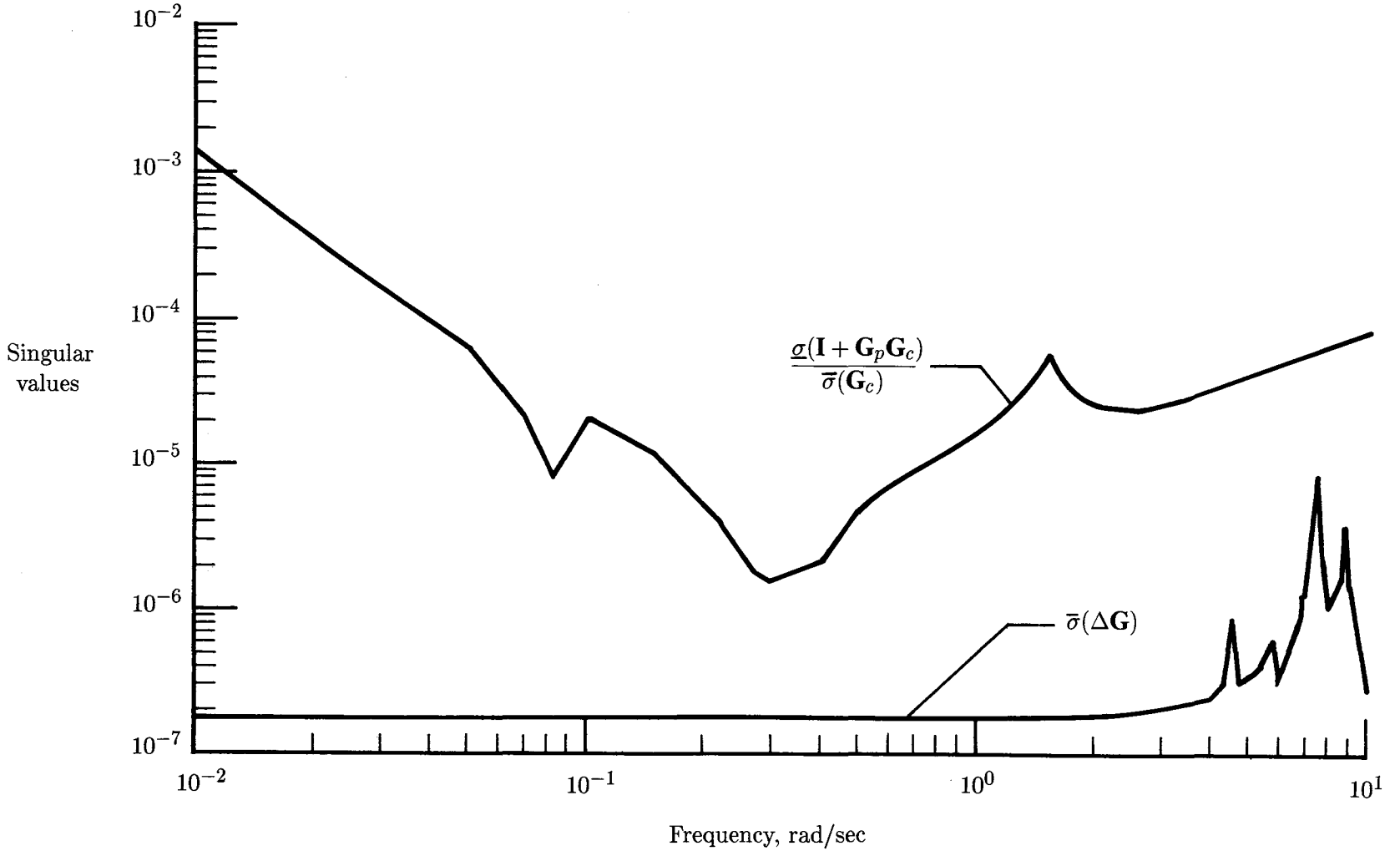

Figure 21. Stability robustness test (eq. (11)) for three-mode model (attitude feedback).

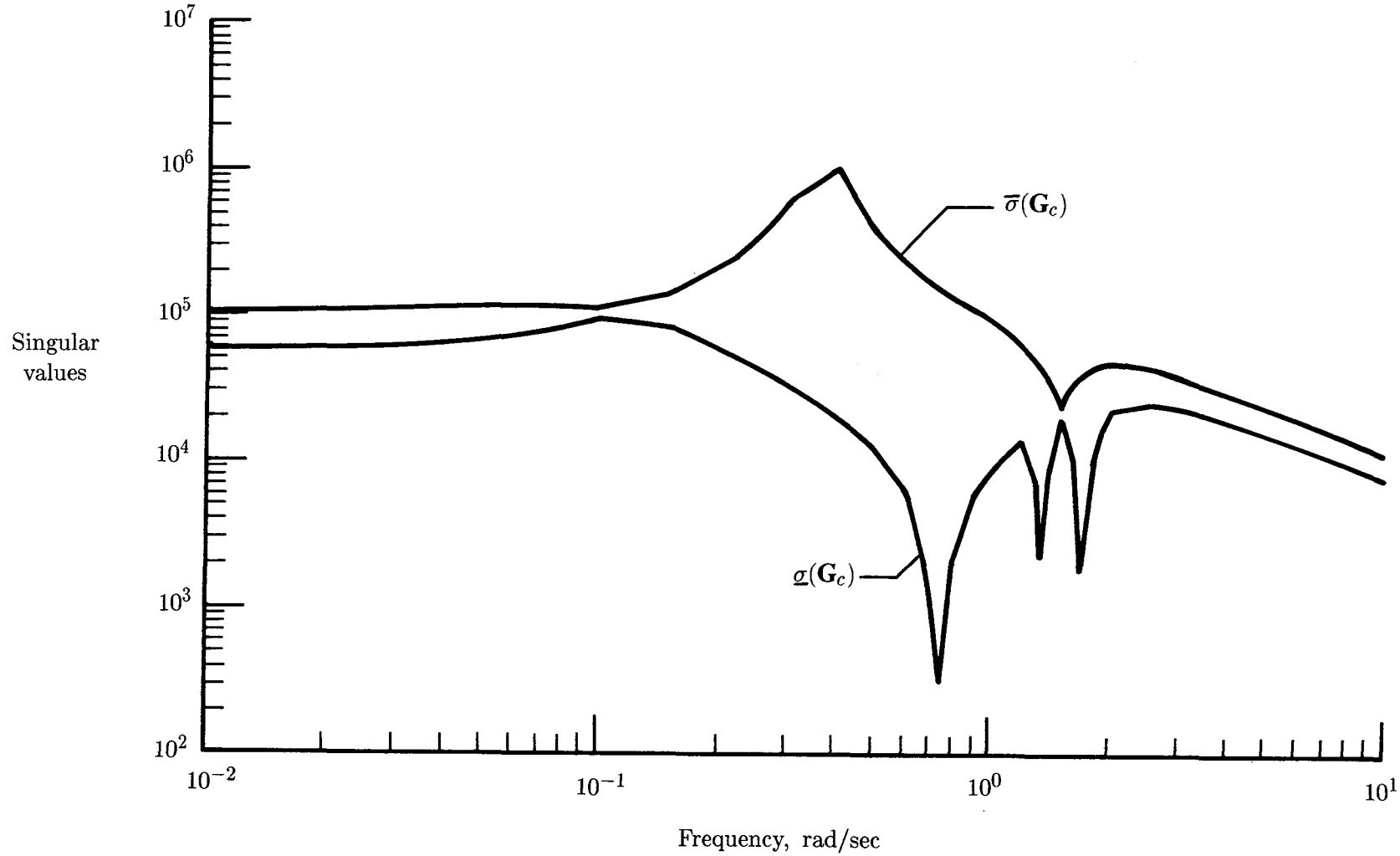

Figure 22. Singular values of compensator $\mathbf{G}_c$ for three-mode design model (attitude feedback).

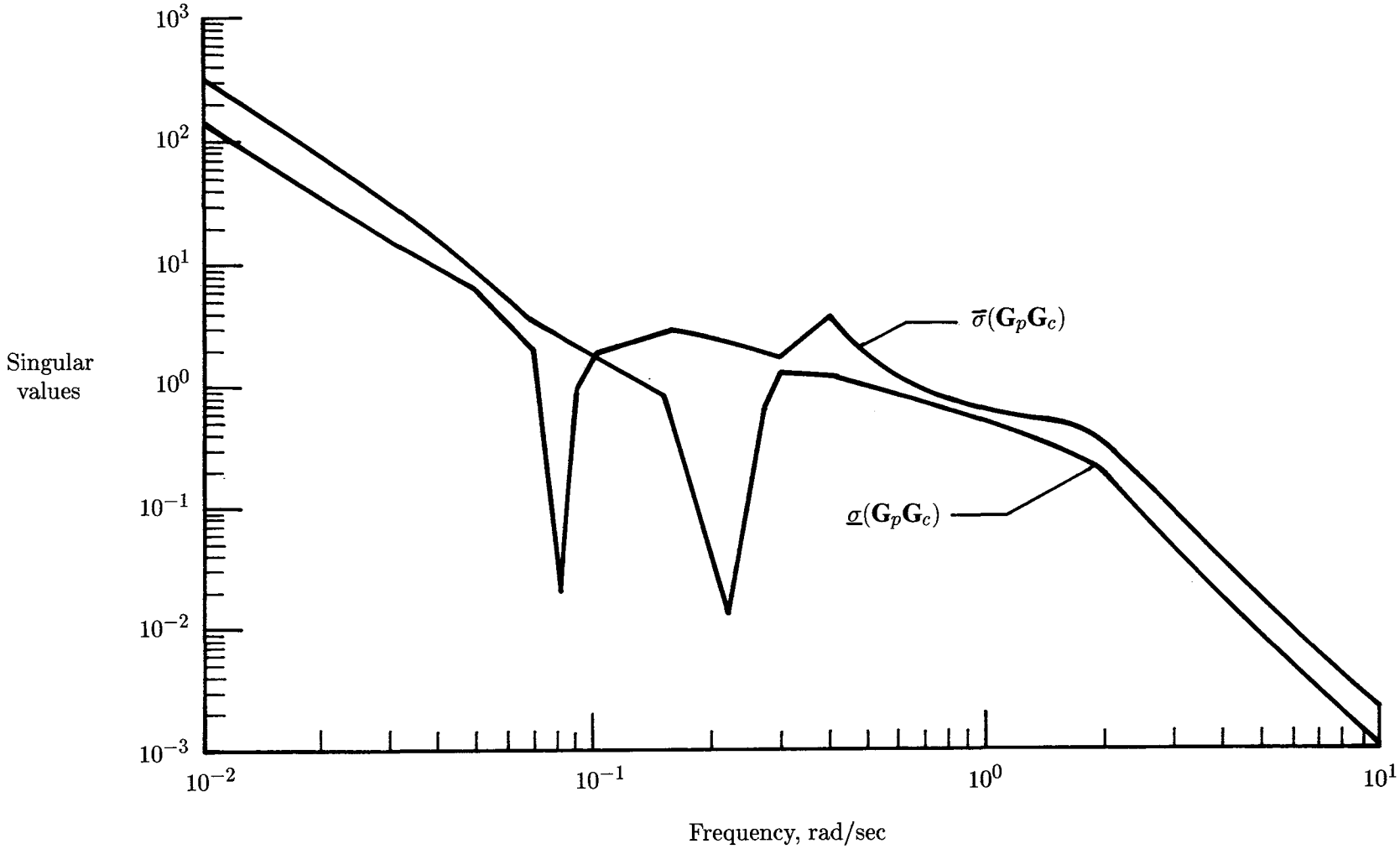

Figure 23. Singular values of $\mathbf{G}_p\mathbf{G}_c$ for three-mode design model (attitude feedback).

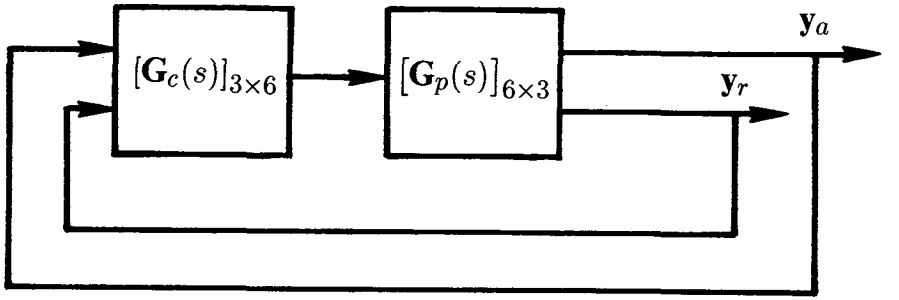

(a) Attitude and rate feedback loop.

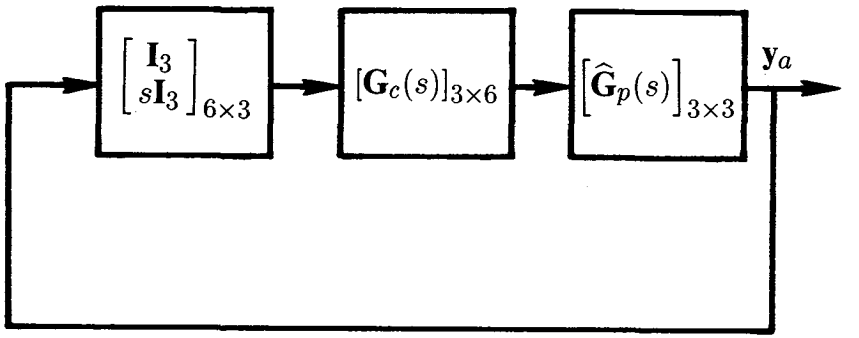

(b) Modified attitude and rate feedback loop.

Figure 24. Modified block diagram for attitude and rate feedback.

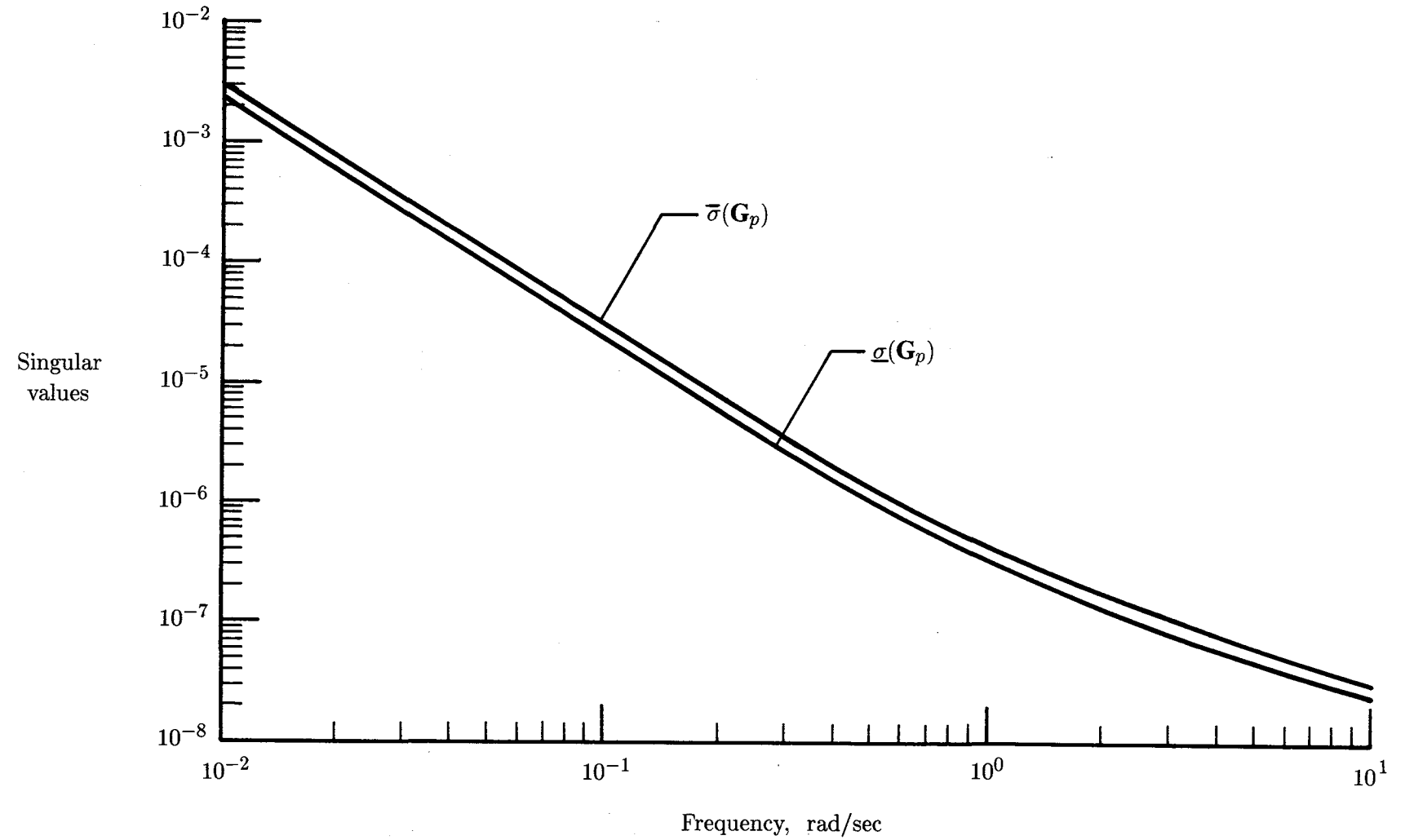

Figure 25. Singular values of $\mathbf{G}_p$ for rigid-body design model (attitude and rate feedback).

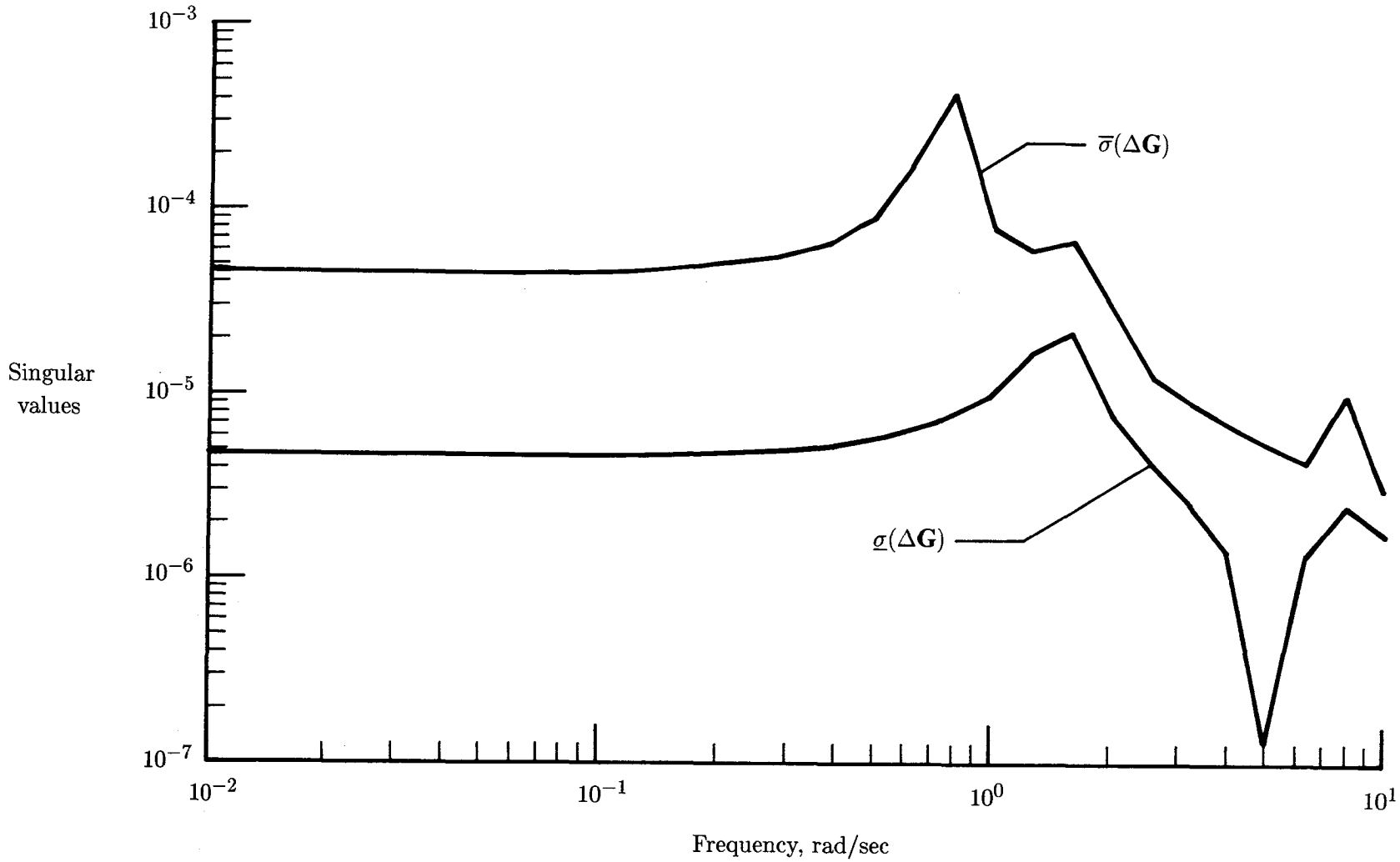

Figure 26. Singular values of $\Delta \mathbf{G}$ for rigid-body design model (attitude and rate feedback).

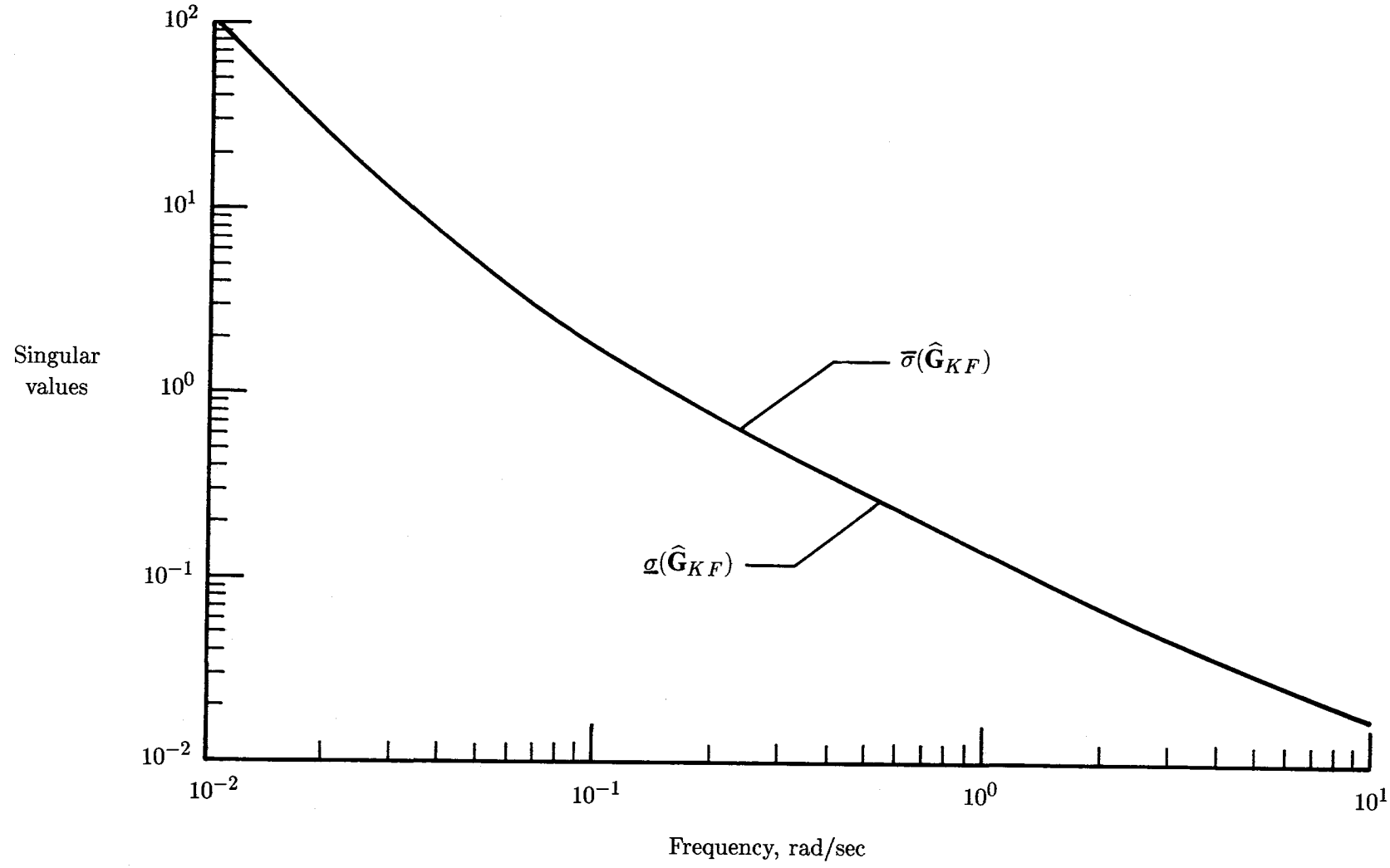

Figure 27. Singular values of $\widehat{\mathbf{G}}_{KF}$ for rigid-body design model (attitude and rate feedback).

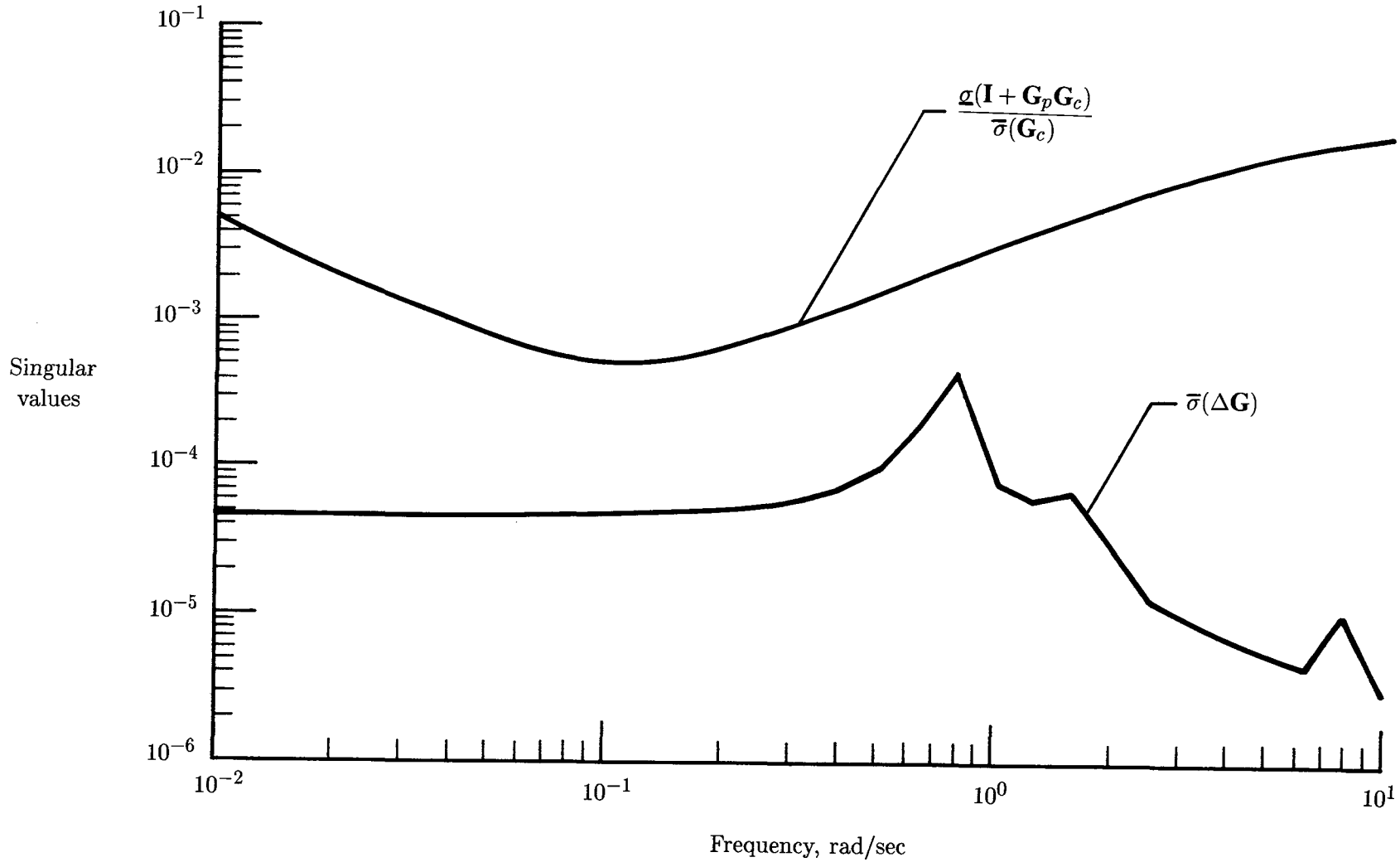

Figure 28. Stability robustness test (eq. (11)) for rigid-body design model (attitude and rate feedback).

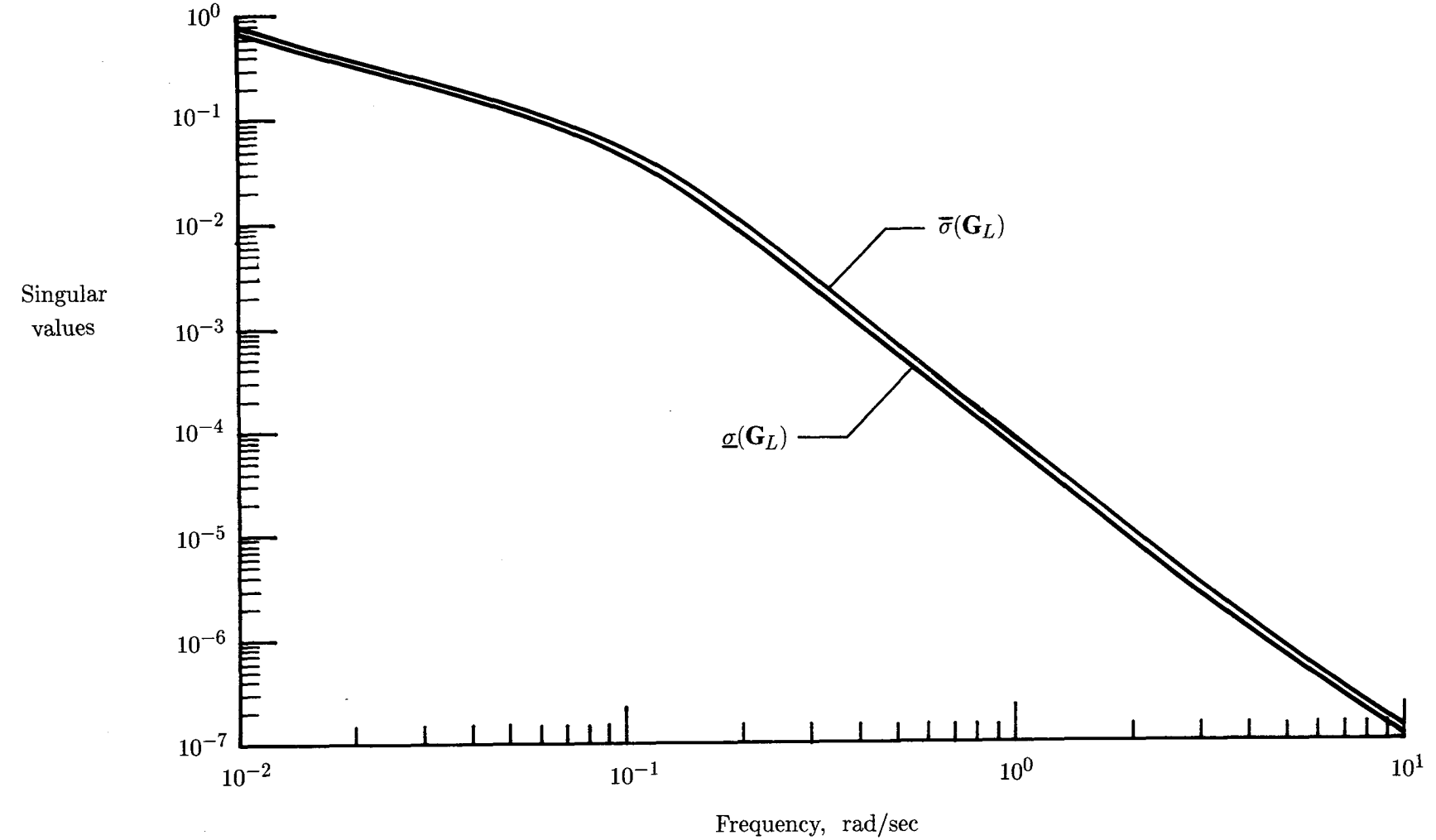

Figure 29. Singular values of loop transfer matrix $\mathbf{G}_L$ for rigid-body design model (attitude and rate feedback).

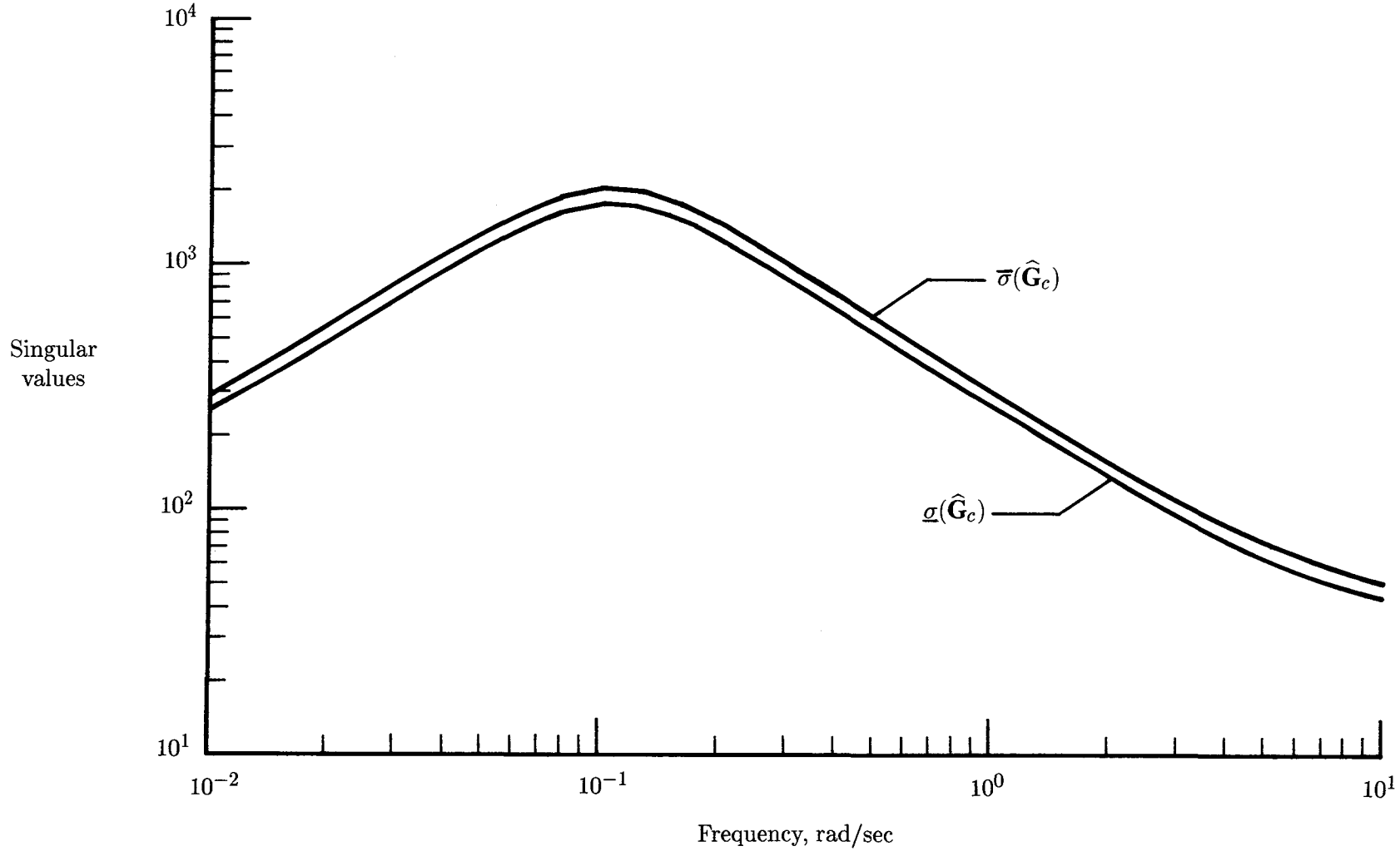

Figure 30. Singular values of compensator $\widehat{\mathbf{G}}_c$ for rigid-body design model (attitude and rate feedback).

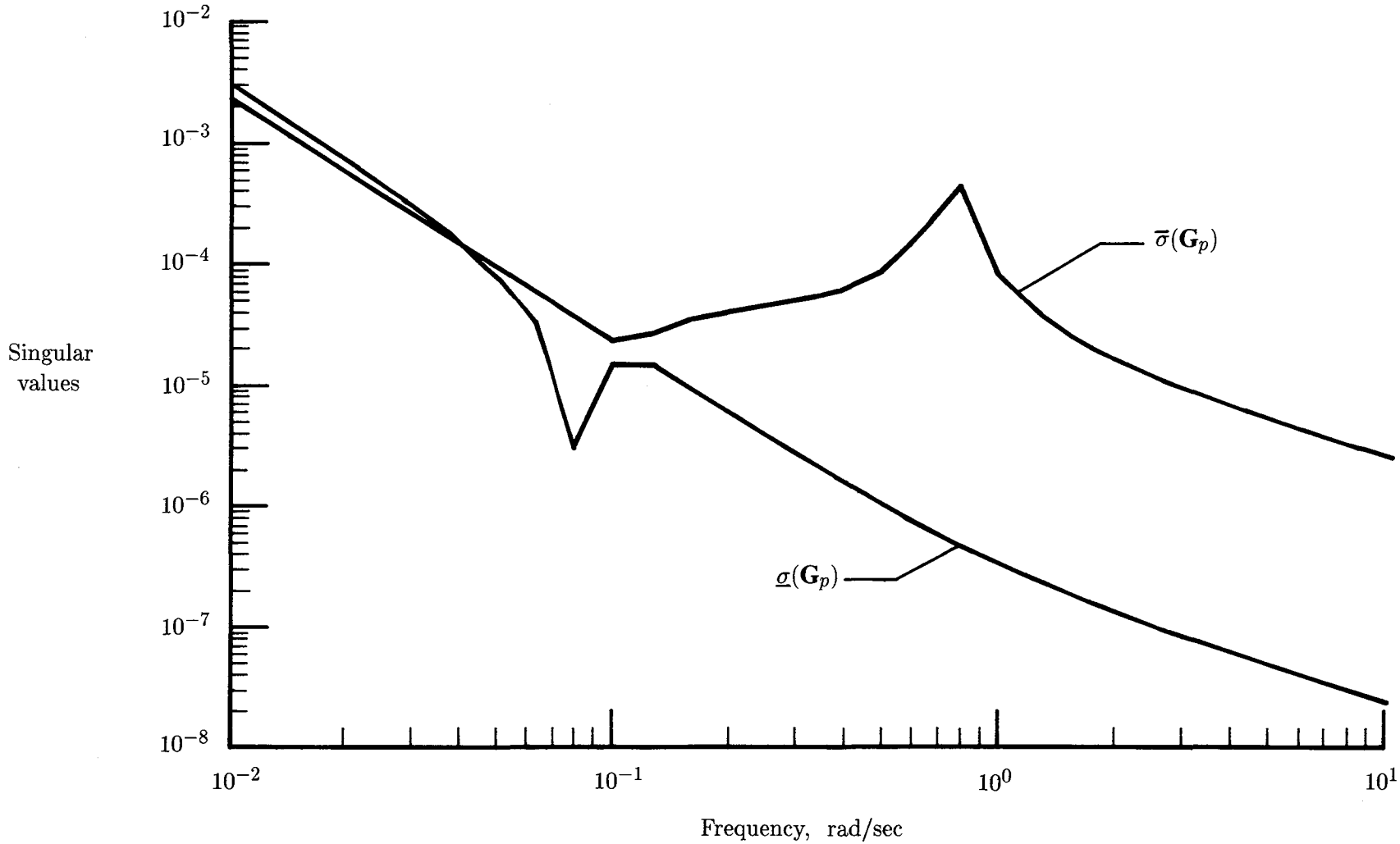

Figure 31. Singular values of $\mathbf{G}_p$ for one-mode design model (attitude and rate feedback).

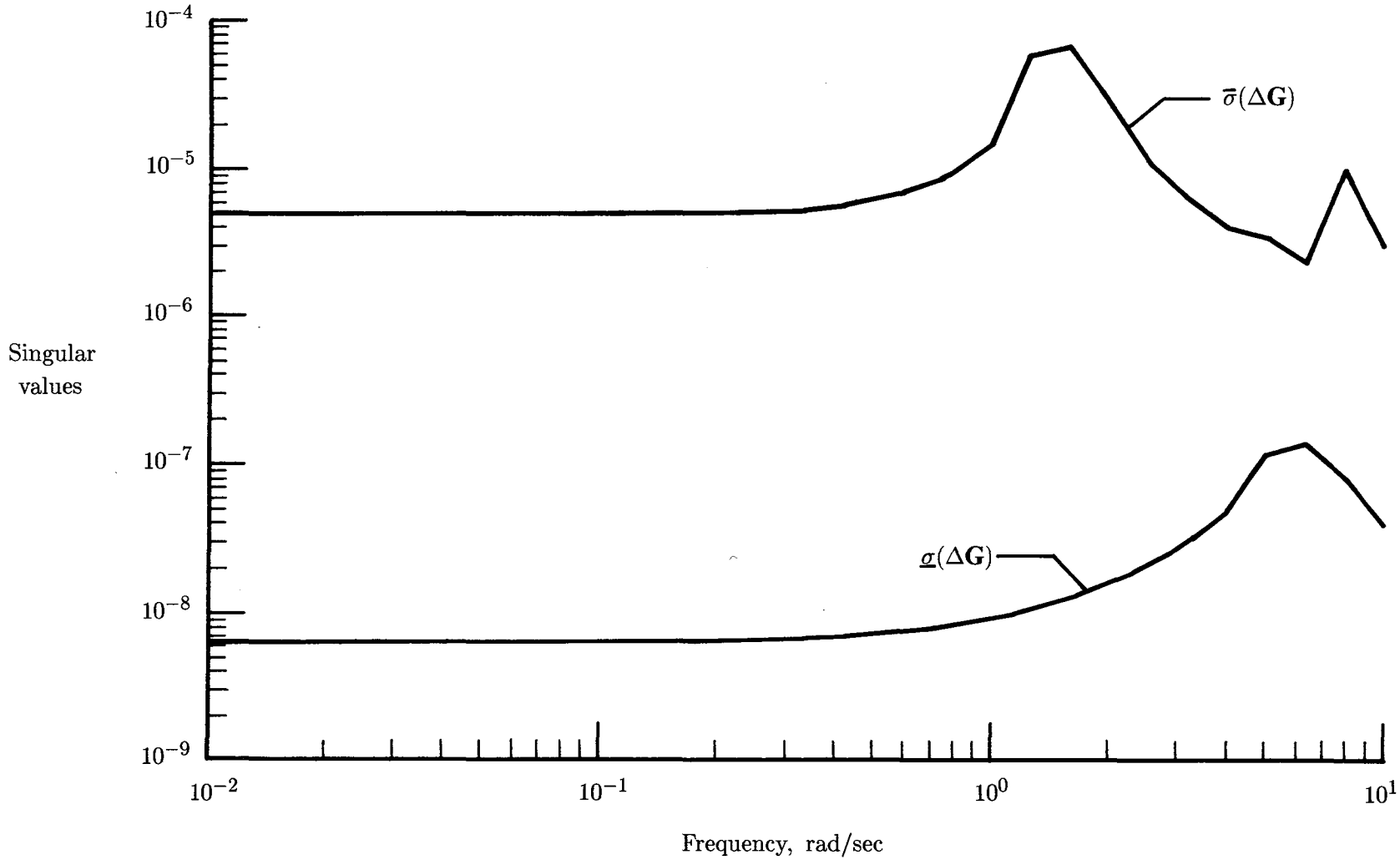

Figure 32. Singular values of $\Delta \mathbf{G}$ for one-mode design model (attitude and rate feedback).

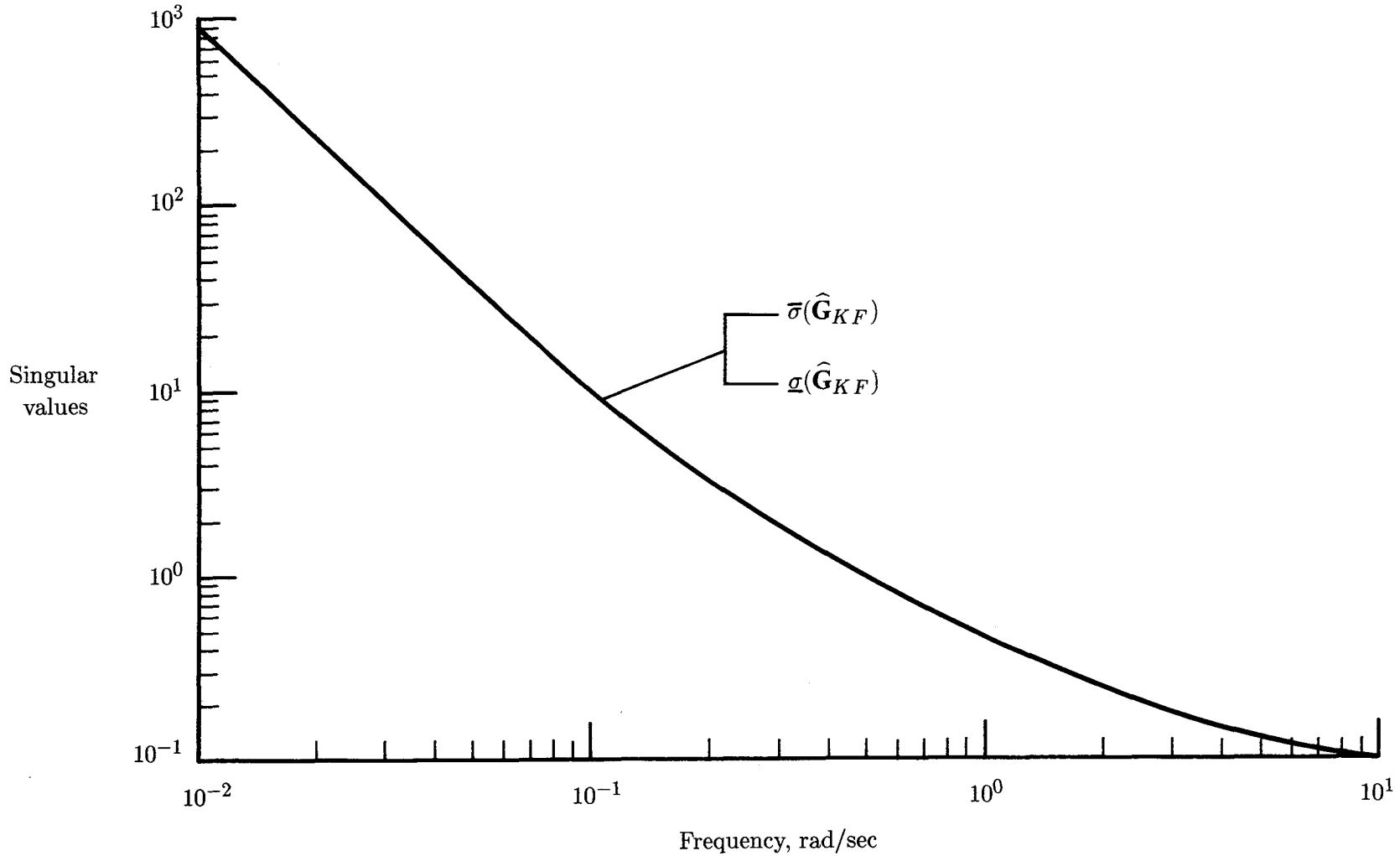

Figure 33. Singular values of $\widehat{\mathbf{G}}_{KF}$ for one-mode design model (attitude and rate feedback).

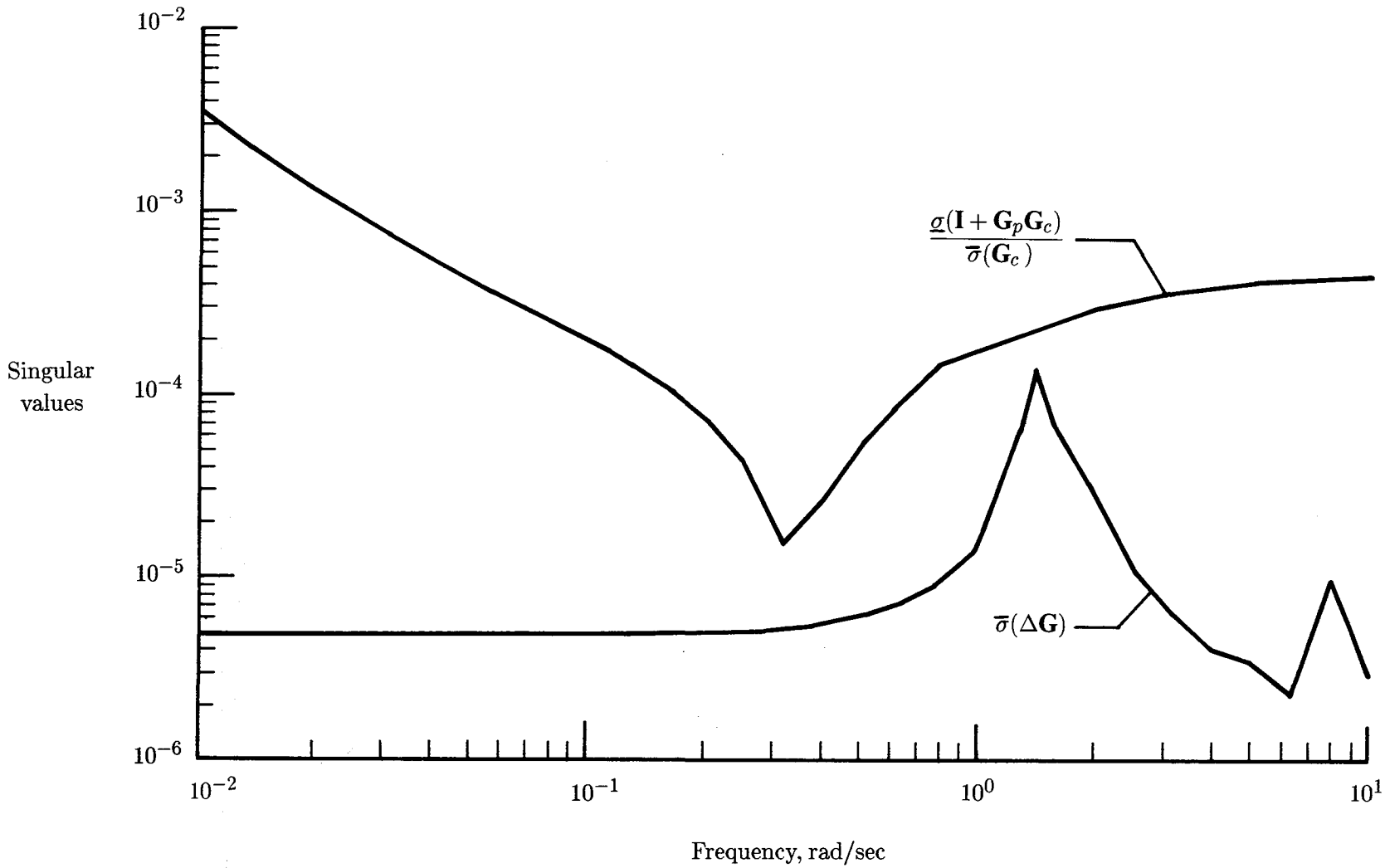

Figure 34. Stability robustness test (eq. (11)) for one-mode design model (attitude and rate feedback).

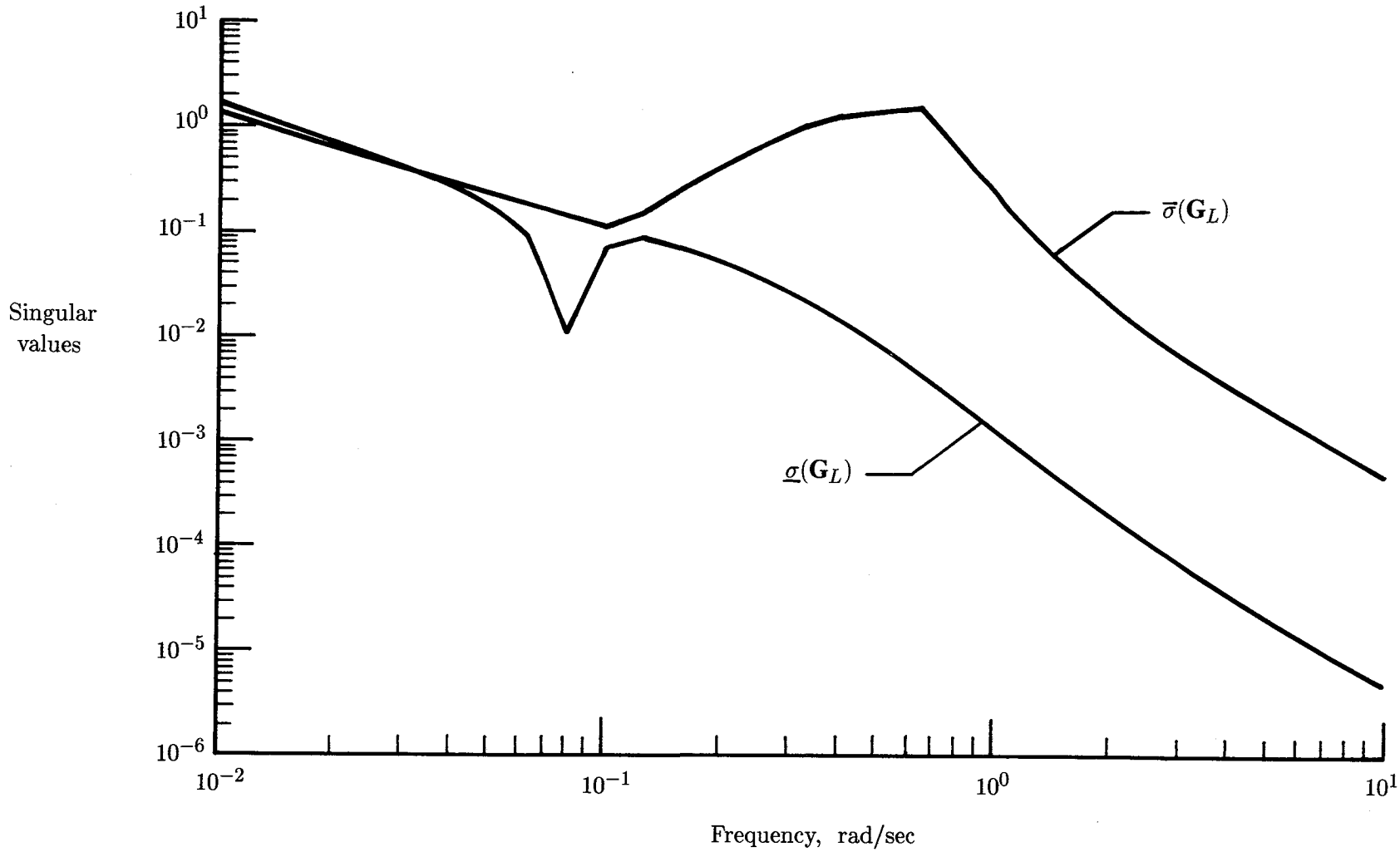

Figure 35. Singular values of loop transfer matrix $\mathbf{G}_L$ for one-mode design model (attitude and rate feedback).

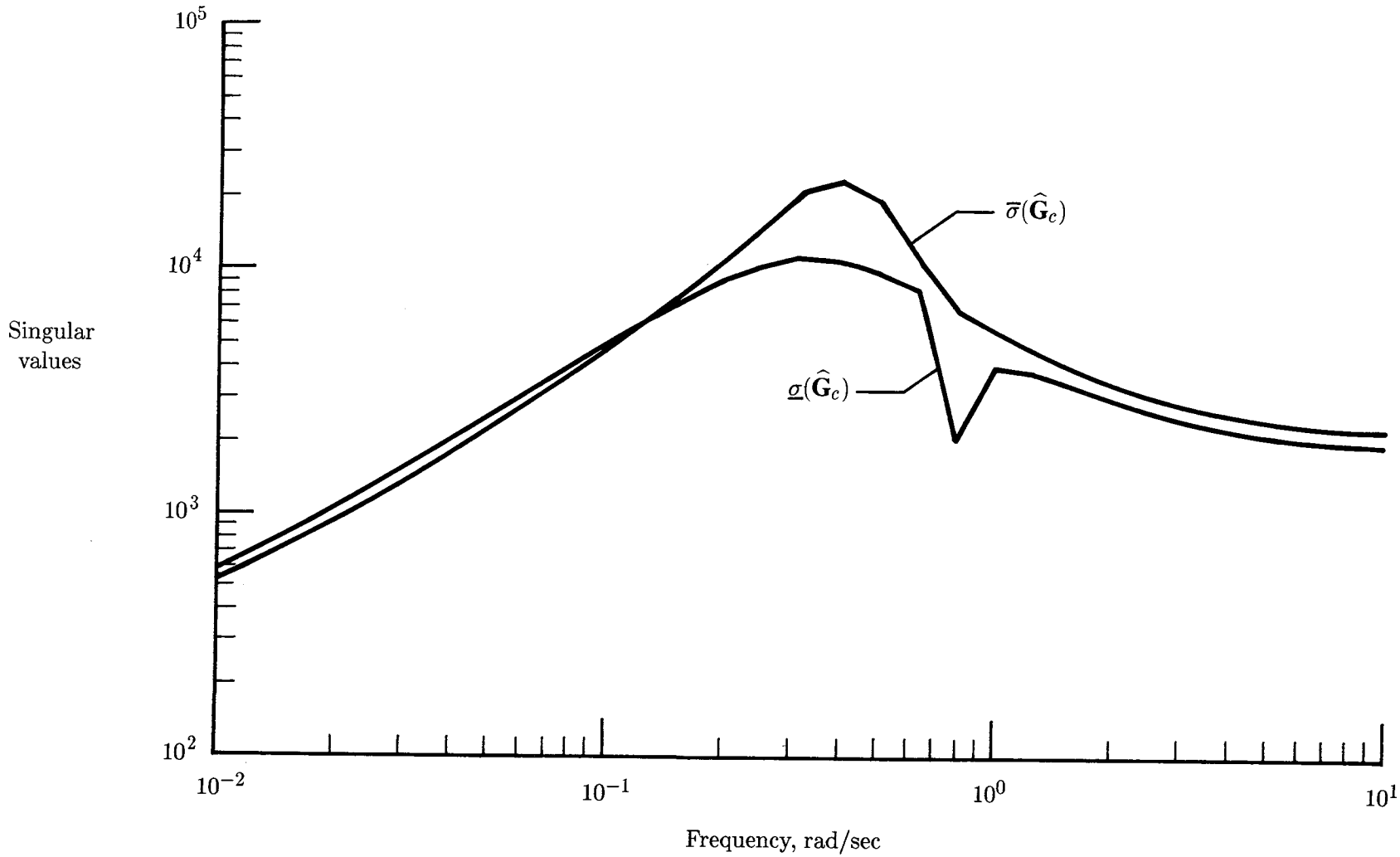

Figure 36. Singular values of compensator $\widehat{\mathbf{G}}_c$ for one-mode design model (attitude and rate feedback).

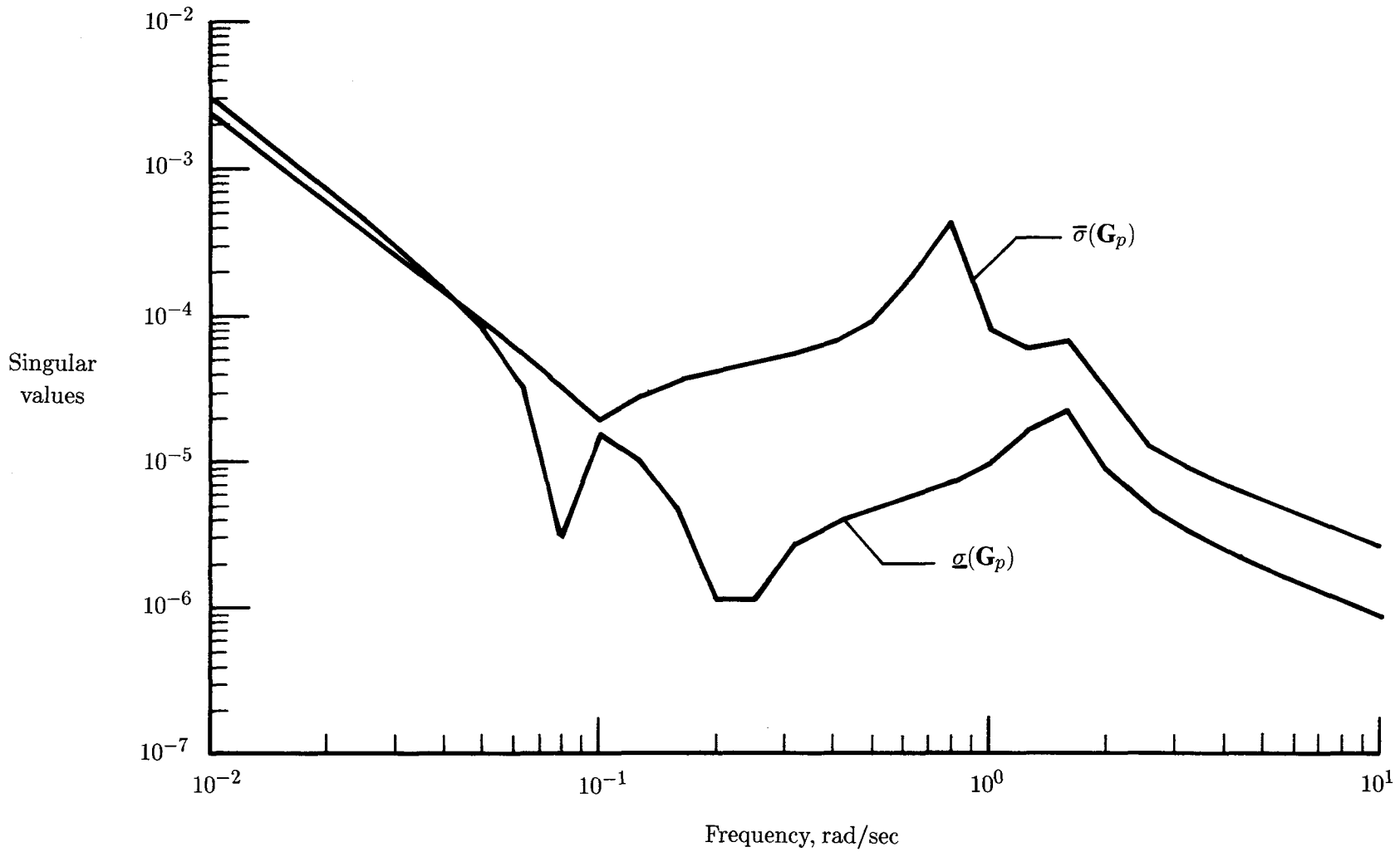

Figure 37. Singular values of $\mathbf{G}_p$ for three-mode design model (attitude and rate feedback).

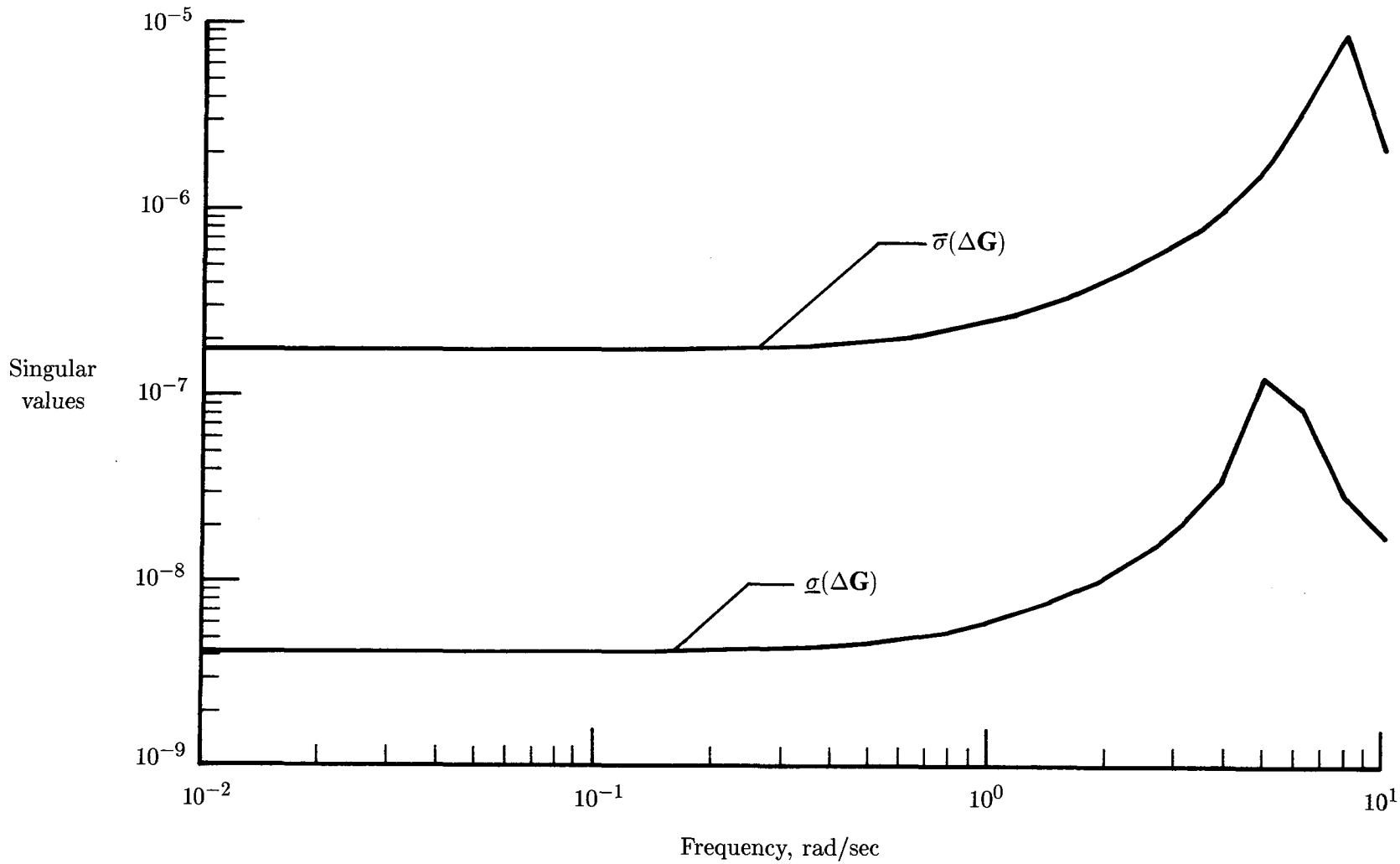

Figure 38. Singular values of $\Delta \mathbf{G}$ for three-mode design model (attitude and rate feedback).

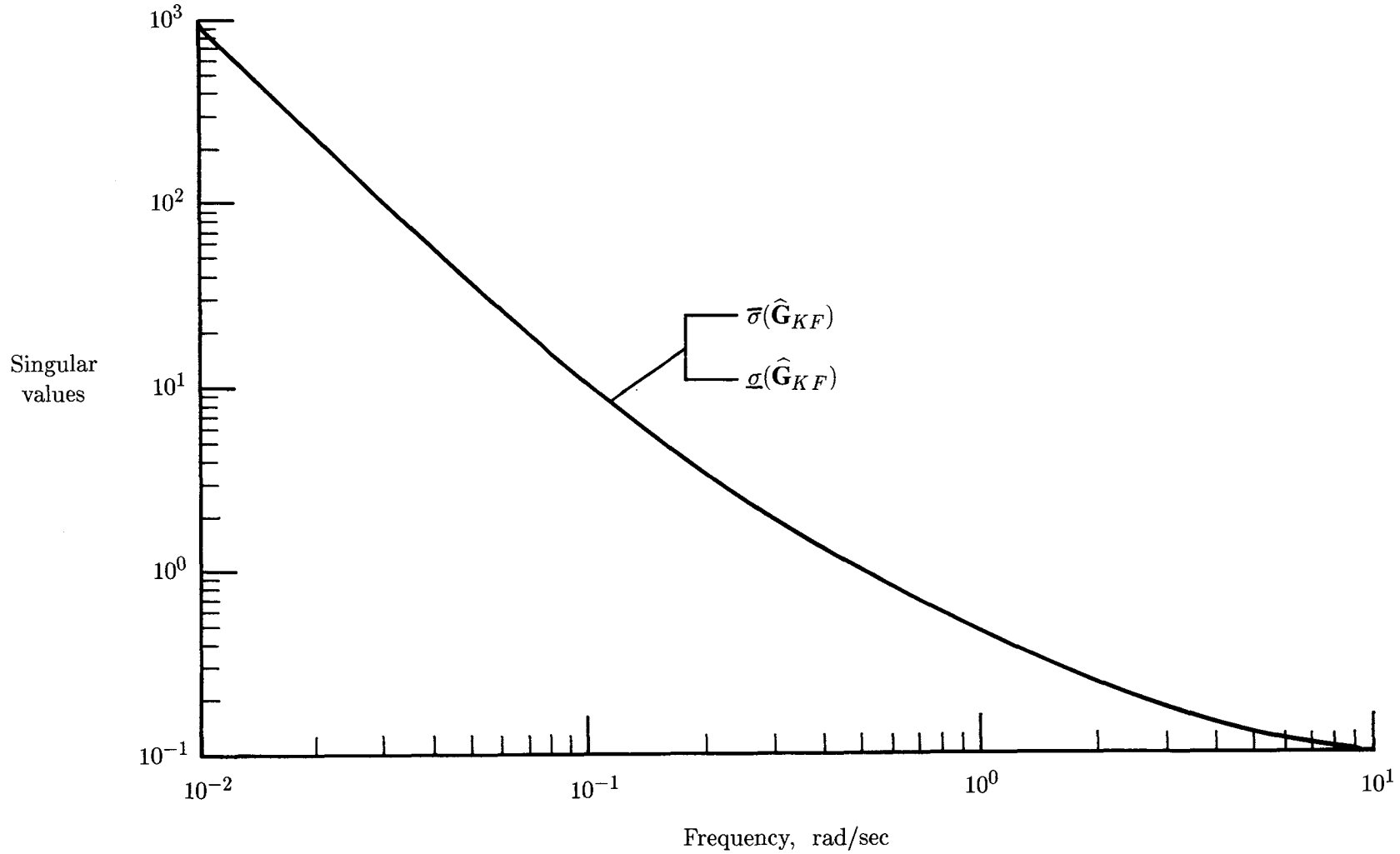

Figure 39. Singular values of $\widehat{\mathbf{G}}_{KF}$ for three-mode design model (attitude and rate feedback).

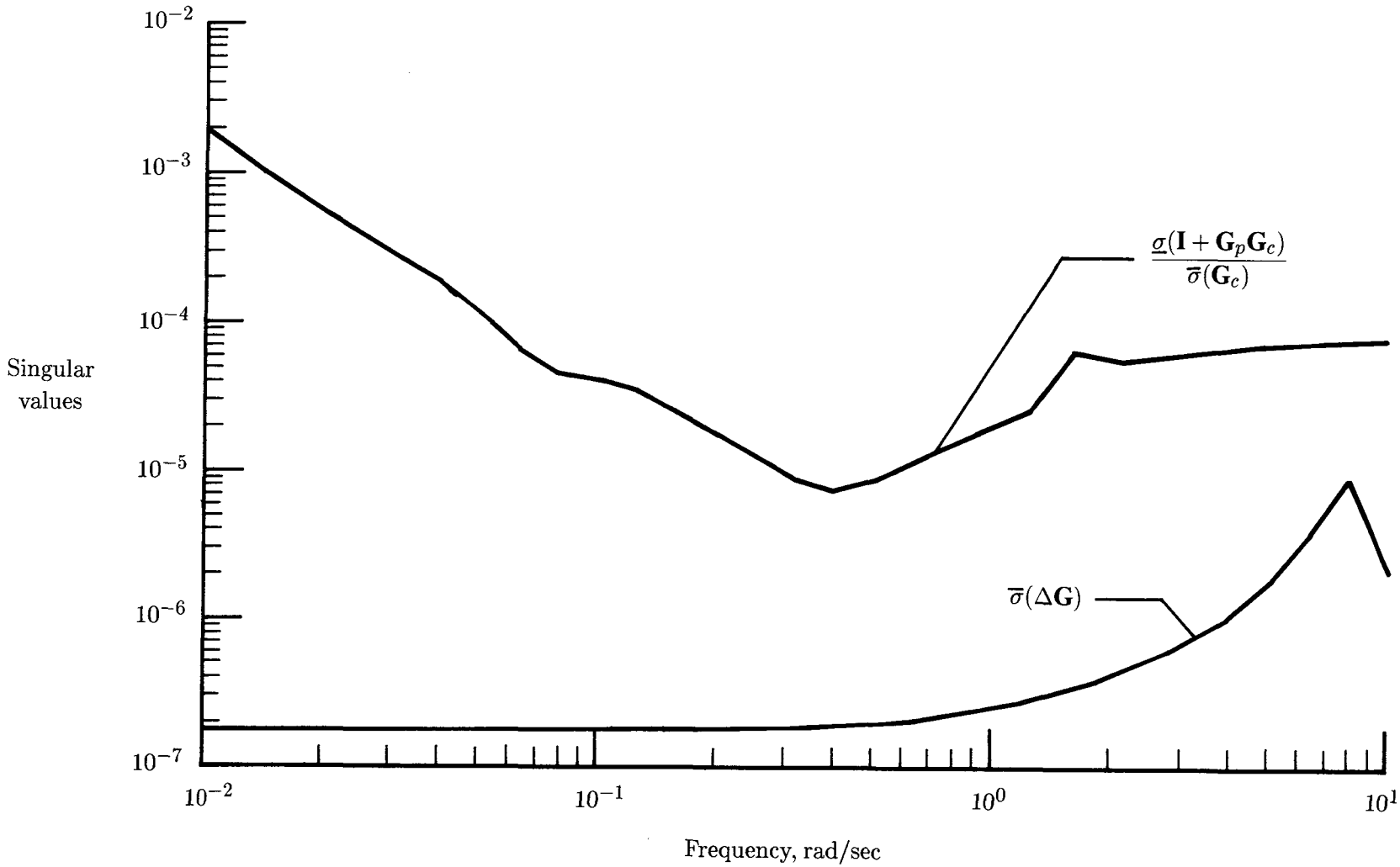

Figure 40. Stability robustness test (eq. (11)) for three-mode design model (attitude and rate feedback).

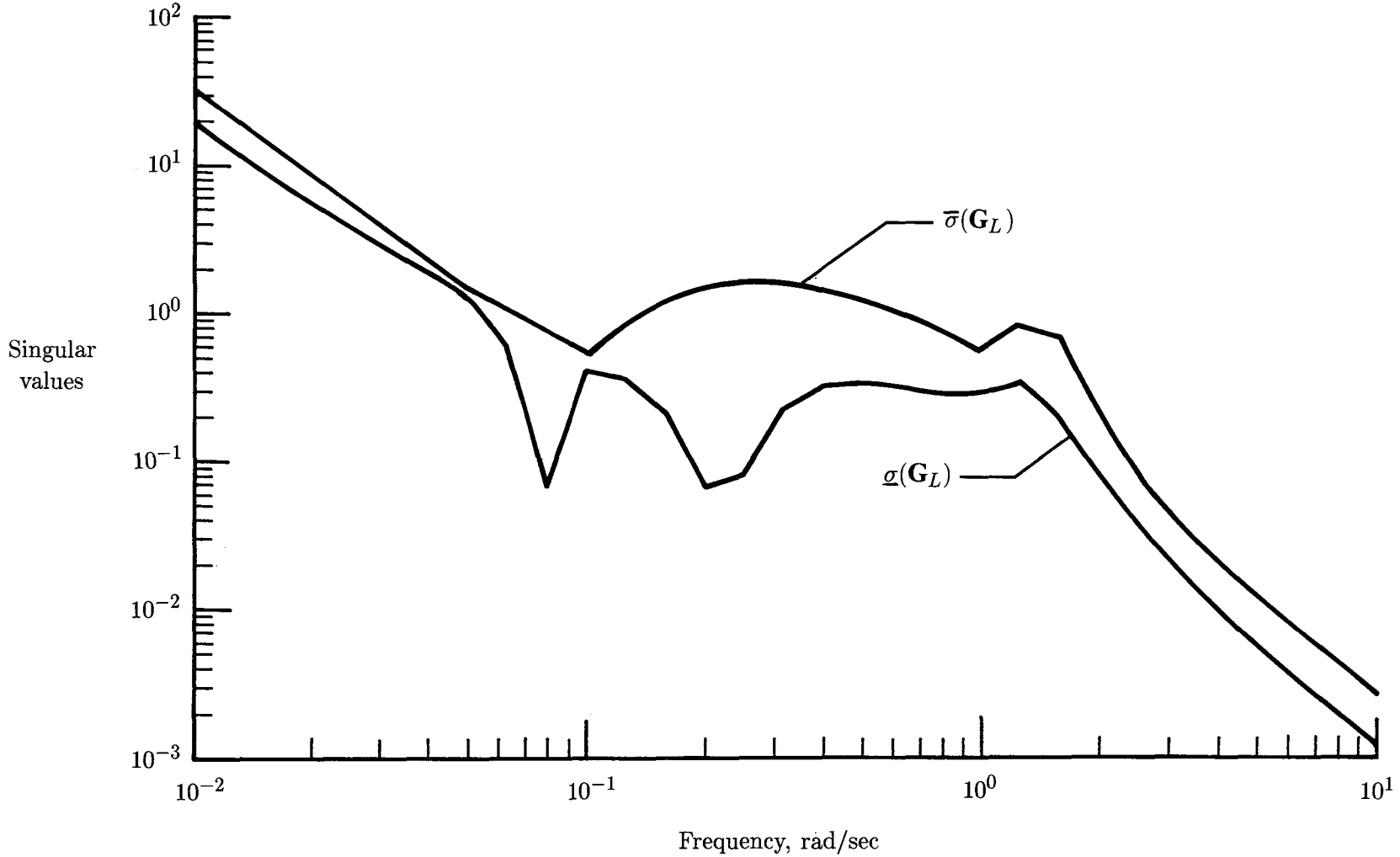

Figure 41. Singular values of loop transfer matrix $\mathbf{G}_L$ for three-mode design model (attitude and rate feedback).

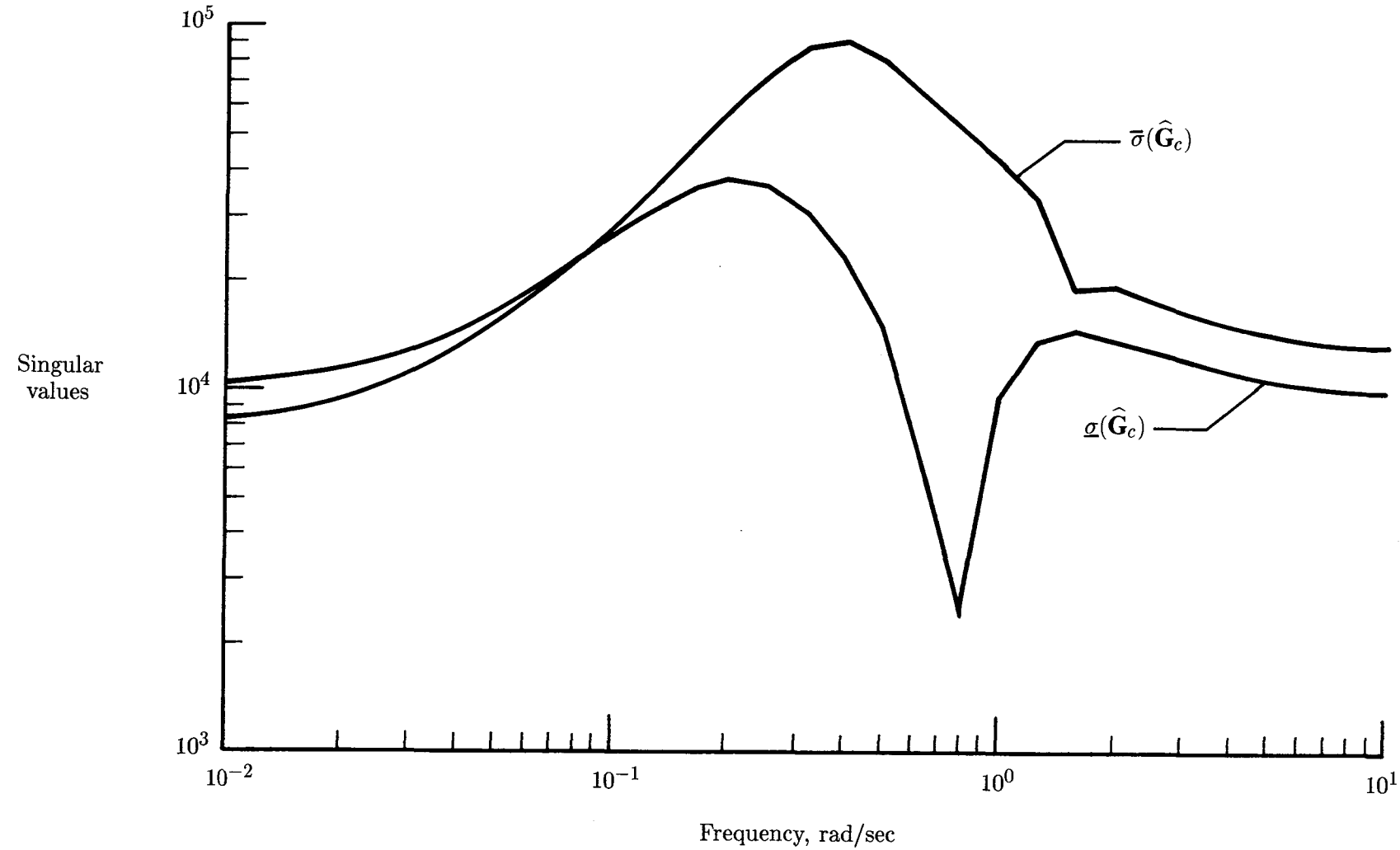

Figure 42. Singular values of compensator $\widehat{\mathbf{G}}_c$ for three-mode design model (attitude and rate feedback).

Standard Bibliographic Page

1. Report No.	2. Government Accession No.	3. Recipient's Catalog No.
NASA TP-2560		

4. Title and Subtitle	5. Report Date
Application of the LQG/LTR Technique to Robust Controller Synthesis for a Large Flexible Space Antenna	September 1986
	6. Performing Organization Code: 506-46-11-01
7. Author(s): Suresh M. Joshi, Ernest S. Armstrong, and N. Sundararajan	8. Performing Organization Report No.: L-16076
9. Performing Organization Name and Address: NASA Langley Research Center, Hampton, VA 23665-5225	10. Work Unit No.
	11. Contract or Grant No.
12. Sponsoring Agency Name and Address: National Aeronautics and Space Administration, Washington, DC 20546-0001	13. Type of Report and Period Covered: Technical Paper
	14. Sponsoring Agency Code

15. Supplementary Notes

Suresh M. Joshi and Ernest S. Armstrong: Langley Research Center, Hampton, Virginia.
N. Sundararajan: Old Dominion University Research Foundation, Norfolk, Virginia; now with Indian Space Research Organization, Bangalore, India.

16. Abstract

The problem of synthesizing a robust controller is considered for a large, flexible space-based antenna by using the linear-quadratic-Gaussian (LQG)/loop transfer recovery (LTR) method. The study is based on a finite-element model of the 122-m hoop/column antenna, which consists of three rigid-body rotational modes and the first 10 elastic modes. A robust compensator design for achieving the required performance bandwidth in the presence of modeling uncertainties is obtained using the LQG/LTR method for loop-shaping in the frequency domain. Different sensor actuator locations are analyzed in terms of the pole/zero locations of the multivariable systems and possible best locations are indicated. The computations are performed by using the LQG design package ORACLS augmented with frequency domain singular value analysis software.

17. Key Words (Suggested by Authors(s))	18. Distribution Statement
Robust controller design Flexible spacecraft control Large space antenna	Unclassified—Unlimited Subject Category 18

19. Security Classif.(of this report)	20. Security Classif.(of this page)	21. No. of Pages	22. Price
Unclassified	Unclassified	62	A04

For sale by the National Technical Information Service, Springfield, Virginia 22161

NASA-Langley, 1986

National Aeronautics and
Space Administration
Code NIT-4

Washington, D.C.
20546-0001